Journal of
Biomedical Optics

BiomedicalOptics.SPIEDigitalLibrary.org

Polarized light interaction with tissues

Valery V. Tuchin

Valery V. Tuchin, “Polarized light interaction with tissues,” *J. Biomed. Opt.* **21**(7), 071114 (2016), doi: 10.1117/1.JBO.21.7.071114.

Journal of Biomedical Optics 21(7), 071114 (July 2016)

TUTORIAL

Polarized light interaction with tissues

Valery V. Tuchin[a,b,c,*]
[a]Saratov National Research State University, Research-Educational Institute of Optics and Biophotonics, 83 Astrakhanskaya street, Saratov 410012, Russia
[b]Institute of Precision Mechanics and Control of Russian Academy of Sciences, 24 Rabochaya street, Saratov 410028, Russia
[c]National Research Tomsk State, Interdisciplinary Laboratory of Biophotonics, 36 Prospect Lenina, Tomsk 634050, Russia

Abstract. This tutorial-review introduces the fundamentals of polarized light interaction with biological tissues and presents some of the recent key polarization optical methods that have made possible the quantitative studies essential for biomedical diagnostics. Tissue structures and the corresponding models showing linear and circular birefringence, dichroism, and chirality are analyzed. As the basis for a quantitative description of the interaction of polarized light with tissues, the theory of polarization transfer in a random medium is used. This theory employs the modified transfer equation for Stokes parameters to predict the polarization properties of single- and multiple-scattered optical fields. The near-order of scatterers in tissues is accounted for to provide an adequate description of tissue polarization properties. Biomedical diagnostic techniques based on polarized light detection, including polarization imaging and spectroscopy, amplitude and intensity light scattering matrix measurements, and polarization-sensitive optical coherence tomography are described. Examples of biomedical applications of these techniques for early diagnostics of cataracts, detection of precancer, and prediction of skin disease are presented. The substantial reduction of light scattering multiplicity at tissue optical clearing that leads to a lesser influence of scattering on the measured intrinsic polarization properties of the tissue and allows for more precise quantification of these properties is demonstrated. [DOI: 10.1117/1.JBO.21.7.071114]

Keywords: biomedical optics; birefringence; medical imaging; optical properties; polarization; tissues.

Paper 160010SSTR received Jan. 4, 2016; accepted for publication Mar. 22, 2016; published online Apr. 28, 2016.

1 Introduction

The randomness of tissue structures results in fast depolarization of polarized light propagating in tissues; thus, for many optical imaging methods, such as diffusion optical tomography, polarization effects are usually ignored.[1–6] However, in certain tissues and cell structures (transparent tissues, such as eye tissues, cellular monolayers, mucous membrane, and superficial skin layers), the degree of polarization of transmitted or reflected light remains measurable even when the tissue has a considerable thickness.[2–29] Information about tissue structure can be extracted from the registered depolarization degree of initially polarized light, the transformation of the polarization state, or the appearance of a polarized component in the scattered light.

In regard to the practical implication of the polarization method, its gating ability to select ballistic photons from diffuse ones gives rise to simplified schemes of optical medical tomography compared with time-resolved methods and provides enhanced image contrast and resolution, as well as additional information about the structure, absorption inclusions, and blood supply in tissues.[8–10,15,23–29]

In addition to the long and successful history of polarimetry as a comprehensive tool for the study of different materials,[30–36], its earlier achievements included characterization of transparent bacterial[37–41] and red blood cell (RBC)[42] suspensions and examination of clear tissues, such as the eye cornea,[43–46] lens,[47] and retinal nerve fibers;[48,49] recently, this old research field was significantly driven by innovations in polarization measuring technologies, computing, and perspectives of widespread biomedical applications.[5–29,50–95] Among the driving forces for improvement of measurement accuracy on the background of multiple scattering and simultaneous existence of different polarization effects are polarization gating in CW and pulsed modes, utilizing the full description of polarized light by amplitude (2×2, Jones) or intensity (4×4 or 3×3 Mueller matrices) and the Mueller matrix decomposition technique, application of the concept of Poincaré sphere, and exploiting the polarization-sensitive optical coherence tomography (PS-OCT).

In this review-tutorial paper, we present the fundamentals of polarized light interaction with biological tissues and some of the recent key polarization optical methods that made possible the quantitative studies essential for biomedical diagnostics, as well as examples and a brief review of the cutting-edge PS measuring techniques for early pathology diagnostics. We also demonstrate the substantial improvement of tissue intrinsic polarization properties by elimination of multiple scattering effects at optical clearing.

2 Fundamentals of Polarized Light Scattering

A polarized light at incidence on an object can be presented as two orthogonal linear polarization components of the incident light field parallel ($\vec{E}_{||i}$) and perpendicular ($\vec{E}_{\perp i}$) to the scattering plane as is shown in Fig. 1. This figure illustrates the geometry of the scattering of light by an object (a particle representing the elementary component of a tissue or a cell). Here, the incident light beam, $\vec{S}_0$, is parallel to the z-axis, and θ and φ are the scattering angles in the scattering plane and in the plane perpendicular to the scattering plane, respectively.[96] Within the detector plane located at a distance r from the origin along the vector $\vec{S}_1$, two orthogonal polarization components, $\vec{E}_{||s}$ and $\vec{E}_{\perp s}$, of the scattered

---

*Address all correspondence to: Valery V. Tuchin, E-mail: tuchinvv@mail.ru

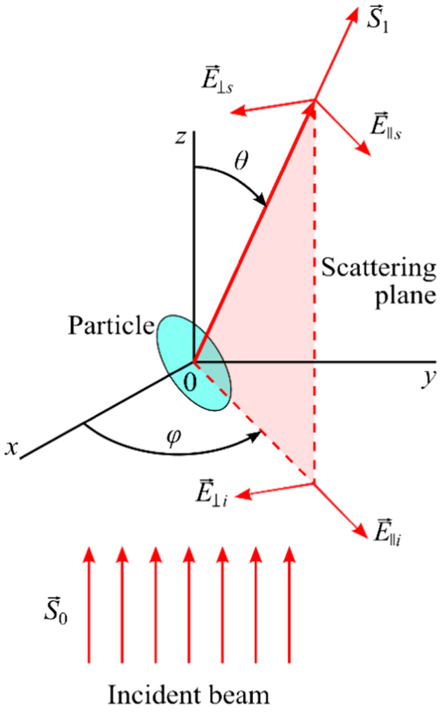

Fig. 1 Geometry of the scattering of light by a particle located at the origin.[96] The polarized incident light beam ($\vec{S}_0$) is parallel to the z-axis. Two orthogonal linear polarization components of the incident light field are presented as vectors $\vec{E}_{||i}$ and $\vec{E}_{\perp i}$ in parallel and perpendicular to the scattering plane, respectively. θ and φ are the scattering angles in the scattering plane and in the plane perpendicular to the scattering plane, respectively. A detector is located at distance r from the origin along the vector $\vec{S}_1$, where two orthogonal polarization components $\vec{E}_{||s}$ and $\vec{E}_{\perp s}$ of scattered light are coming.

light create a specific polarization state depending on amplitudes and phase shifts between components.

The transformation of an arbitrary polarized light (linear, circular, or elliptical) by a scattering particle can be described using a linear relationship between the incident and the scattered field components,[5,15,22,30–38,96–101]

$$\begin{bmatrix} \vec{E}_{||s} \\ \vec{E}_{\perp s} \end{bmatrix} = \frac{e^{ik(r-z)}}{-ikr} \begin{bmatrix} S_2 & S_3 \\ S_4 & S_1 \end{bmatrix} \begin{bmatrix} \vec{E}_{||i} \\ \vec{E}_{\perp i} \end{bmatrix}, \tag{1}$$

where $k = 2\pi/\lambda$ is the wave number, $i = \sqrt{-1}$, r is the distance from the scatterer to the detector, and z is the position coordinate of the scatterer (see Fig. 1).

The complex numbers S_1 through S_4 are the elements of the amplitude scattering matrix (S-matrix) or Jones matrix. They each depend on the scattering and azimuthal angles θ and φ, and contain information about the scatterer. Both amplitude and phase must be measured to quantify the amplitude scattering matrix. Polarimetric experimental methods are available to determine the Jones matrix elements of transparent optical materials without sign ambiguity.[102] For scattering tissues, the direct measurements of Jones matrix elements can be done using a two-frequency Zeeman laser, which produces two laser lines with a small frequency separation (~250 kHz) and orthogonal linear polarizations,[38] or by the OCT technique.[15,103]

However, more often, Stokes or Mueller polarimeters based on intensity measurements of polarized light are used.[5,15,21,22,30–38,87,91,92,96–101,104–108] In that case, light of an arbitrary polarization can be represented by four numbers known as the Stokes parameters, I, Q, U, and V ($I^2 = Q^2 + U^2 + V^2$), where I refers to the intensity of the light, and the parameters Q, U, and V represent the extent of the horizontal linear, 45 deg linear, and circular polarization, respectively.[22,30,96,107] In polarimetry, the Stokes vector $\mathbf{S}$ of a light beam is constructed based on six flux measurements obtained with different polarization analyzers in front of the detector,

$$\mathbf{S} = \begin{bmatrix} I \\ Q \\ U \\ V \end{bmatrix} = \begin{bmatrix} I_H + I_V \\ I_H - I_V \\ I_{+45\ \mathrm{deg}} - I_{-45\ \mathrm{deg}} \\ I_R - I_L \end{bmatrix} = \begin{bmatrix} I_H + I_V \\ I_H - I_V \\ 2I_{+45\ \mathrm{deg}} - (I_H + I_V) \\ 2I_R - (I_H + I_V) \end{bmatrix}, \tag{2}$$

where $I_H, I_V, I_{+45\ \mathrm{deg}}, I_{-45\ \mathrm{deg}}, I_R$, and I_L are the light intensities measured with a horizontal linear analyzer, a vertical linear analyzer, a +45 deg oriented linear analyzer, a −45 deg oriented linear analyzer, a right circular analyzer, and a left circular analyzer in front of the detector, respectively. Because of the relationship $I_H + I_V = I_{+45\ \mathrm{deg}} + I_{-45\ \mathrm{deg}} = I_R + I_L = I$, where I is the intensity of the light beam measured without any analyzer in front of the detector; a Stokes vector can be determined by four independent measurements, for example, $I_H, I_V, I_{+45\ \mathrm{deg}}$, and I_R as is shown in Eq. (2).

From the Stokes vector, the degree of polarization (P), degree of linear polarization (P_L), and the degree of circular polarization (P_C) are derived as[5,15,22,34]

$$P = \frac{\sqrt{Q^2 + U^2 + V^2}}{I}, \tag{3}$$

$$P_L = \frac{I_{||} - I_{\perp}}{I_{||} + I_{\perp}} = \frac{\sqrt{Q^2 + U^2}}{I}, \tag{4}$$

and

$$P_C = \frac{\sqrt{V^2}}{I}. \tag{5}$$

The Stokes vector for a partially polarized beam ($P < 1$) can be considered as a superposition of a completely polarized Stokes vector $\mathbf{S}_P$ and an unpolarized Stokes vector $\mathbf{S}_U$, which are uniquely related to $\mathbf{S}$ as follows:[33,109]

$$\mathbf{S} = \mathbf{S}_P + \mathbf{S}_U = \begin{bmatrix} I \\ Q \\ U \\ V \end{bmatrix} = I \times P \begin{bmatrix} 1 \\ Q/(I \times P) \\ U/(I \times P) \\ V/(I \times P) \end{bmatrix} + I \times (1 - P) \begin{bmatrix} 1 \\ 0 \\ 0 \\ 0 \end{bmatrix}. \tag{6}$$

The polarized portion of the beam represents a net polarization ellipse traced by the electric field vector as a function of time. The ellipse has a magnitude of the semimajor axis a, semiminor axis b, orientation of the major axis ϕ_o (azimuth of the ellipse) measured counterclockwise from the x axis,

$$\phi_o = \frac{1}{2}\tan^{-1}\left(\frac{U}{Q}\right), \tag{7}$$

and ellipticity

$$e = \frac{b}{a} = \frac{V}{I + \sqrt{Q^2 + U^2}}. \tag{8}$$

The ellipticity is the ratio of the minor to the major axes of the corresponding electric field polarization ellipse and varies from 0 for linearly polarized light to 1 for circularly polarized light.

In the far field, the polarization of the scattered light from an object (Fig. 1) is described by the Stokes vector $\mathbf{S}_s$ connected with the Stokes vector of the incident light $\mathbf{S}_i$ by the matrix equation $\mathbf{S}_s = M \cdot \mathbf{S}_i$, where M is the normalized 4×4 scattering matrix (intensity or Mueller matrix),[96]

$$\begin{bmatrix} I_s \\ Q_s \\ U_s \\ V_s \end{bmatrix} = \begin{bmatrix} M_{11} & M_{12} & M_{13} & M_{14} \\ M_{21} & M_{22} & M_{23} & M_{24} \\ M_{31} & M_{32} & M_{33} & M_{34} \\ M_{41} & M_{42} & M_{43} & M_{44} \end{bmatrix} \begin{bmatrix} I_i \\ Q_i \\ U_i \\ V_i \end{bmatrix}. \tag{9}$$

Elements of the light-scattering matrix (LSM) depend on the scattering angle θ, the wavelength, and the geometrical and optical parameters of the object. Element $M_{11}(\theta)$ is what is measured when the incident light is unpolarized; its angular dependence is the phase function of the scattered light; it is much less sensitive to chirality and long-range structure than some of the other matrix elements.[38,96] Element M_{12} is obtained by measuring the total scattered intensity for a horizontally linearly polarized incoming beam and subtracting the total scattered intensity for a vertically linearly polarized incoming beam from this; M_{22} displays the ratio of depolarized light to the total scattered light (a good measure of the scatterers' nonsphericity); M_{34} displays the transformation of the 45 deg obliquely polarized incident light to circularly polarized scattered light (which is a unique characteristic for various tissues and cells); the difference between elements M_{33} and M_{44} is a good measure of the scatterers' nonsphericity as well.

The polarization elements used in polarimeters, such as polarizers, retarders, and depolarizers, as well as the objects under study, such as tissues and cell layers or suspensions, have three general polarization properties: depolarization, retardance, and diattenuation.[18–22,30–37,109] A typical object displays some amount of all three properties. Depolarization describes the coupling by an object of incident polarized light into depolarized light in the exiting beam. Depolarization typically occurs when light transmits through or scatters from tissue. Depolarization is intrinsically associated with scattering and a loss of coherence in the polarization state.[109] A depolarization coefficient Δ can be defined as the fraction of unpolarized power in the exiting (scattering) beam when the polarized light is incident; Δ is generally a function of the incident polarization state.

Retardance is the phase change an object introduces between its two orthogonal polarization eigenstates. For materials with a linear birefringence, which is defined as the refractive index difference between wave components propagating along the slow (n_1) and fast (n_2) axes, $\Delta n = n_1 - n_2$, light propagation over a distance d introduces a linear retardation δ expressed in radians as[22,109]

$$\delta = \frac{2\pi(n_1 - n_2)d}{\lambda_0}. \tag{10}$$

A circular retardance appears when two orthogonal polarization eigenstates are counter-rotating circular ones. The origin of the eigenstates is a circular birefringence, which is observed in media lacking any mirror symmetry, like solutions of chiral molecules where only one enantiomer is present.[22] When a linearly polarized wave propagates in such a medium along a distance d, its polarization remains linear, but it is rotated by an angle ψ called optical rotation or optical activity,

$$\psi = \chi d, \tag{11}$$

where

$$\chi = \frac{2\pi \Delta n_c}{\lambda_0}, \tag{12}$$

and Δn_c is the circular birefringence.

Diattenuation (dichroism) arises when the intensity transmittance of an object is a function of the incident polarization state.[109] The diattenuation D_A of an object is defined in terms of the maximum, $T_{\max}$, and minimum, $T_{\min}$, intensity transmittances,

$$D_A = \frac{T_{\max} - T_{\min}}{T_{\max} + T_{\min}} = \frac{P_1^2 - P_2^2}{P_1^2 + P_2^2}, \tag{13}$$

where P_1 and P_2 are the principal coefficients of the amplitude transmission for the two orthogonal polarization eigenstates.

In terms of the Stokes vector and Mueller matrix (LSM) elements, these basic parameters can be expressed as follows. If the degree of polarization P of a light field remains at unity after transformation by an optical system, this system is nondepolarizing; otherwise, the system is depolarizing, with the depolarization being a function of input polarization,[105,106]

$$\Delta = (1 - P)(\phi_o, \sin\delta) = 1 - \frac{\sqrt{Q_s^2 + U_s^2 + V_s^2}}{I_s}, \tag{14}$$

where I_s, Q_s, U_s, and V_s are the output Stokes vector elements corresponding to a given input polarization of light (Fig. 1); ϕ_o is the orientation of the ellipse [Eq. (7)] corresponding to the input polarization state,

$$\phi_o = \frac{1}{2}\tan^{-1}\left(\frac{U_i}{Q_i}\right), \tag{15}$$

and δ is the phase retardance, given by

$$\delta = \tan^{-1}\left(\frac{V_i}{\sqrt{Q_i^2 + U_i^2}}\right). \tag{16}$$

The diattenuation (dichroism) can be presented as

$$D_A = \frac{\sqrt{M_{12}^2 + M_{13}^2 + M_{14}^2}}{M_{11}}. \tag{17}$$

In the scattering media with a low absorption, as many tissues are, the origin for dichroism could be anisotropy in the scattering abilities. In that case, the imaginary part n'' of the complex refractive index of material n will also be determined by light losses associated with scattering,

$$n = n' + in''. \tag{18}$$

In nonscattering materials, the imaginary part n'' is defined only by light losses due to absorption.

In general, all 16 elements of the LSM are nonzero; thus, a minimum of 16 measurements involving both linear and circularly polarized light are required to completely characterize the polarization properties of the sample. For nondepolarizing systems, the number of independent LSM elements cannot be more than seven since both the Mueller matrix and the Jones matrix can represent the system; therefore, in that case, 16 LSM elements are related via nine equations.[98,99,110] Linear and circular diattenuation (dichroism), D_L and D_C, can be presented, respectively, as[109,110]

$$D_L = \frac{\sqrt{M_{12}^2 + M_{13}^2}}{M_{11}}, D_C = \frac{M_{14}}{M_{11}}. \tag{19}$$

3 Tissue Structure and Anisotropy

Healthy cornea and lens of a human eye are highly transparent for visible light because of their ordered structure and the absence of strongly absorbing bands of endogenous chromophores.[5,6,43–47] The human cornea has a thickness of ∼0.5 mm with ∼90% of the thickness being a stroma. Stroma is composed of several hundred successively stacked layers of lamellae, varying in thickness (0.2 to 0.5 μm depending on the tissue region)[43,44,111] [see Figs. 2(a)–2(c)]. These lamellae, consisting of collagenous fibrils, are immersed into an amorphous ground (interstitial) substance containing water, glycosaminoglycans, proteins, proteoglycans, and salts. Fibrils in the human cornea have a uniform diameter of ∼30.8 ± 0.8 nm with a periodicity close to two diameters, i.e., 55.3 ± 4.0 nm, and a high degree of short-range spatial order—a hexagonal quasi-crystal [see Figs. 2(a) and 2(b)]. Within each lamella, all fibrils are nearly parallel with each other and with the lamella plane. The intermolecular spacing within fibrils is of 1.63 ± 0.10 nm.[112] Therefore, the corneal stroma has at least three levels of structural organization.

The sclera is a dense, white, fibrous membrane containing three layers: the episclera, the stroma, and the lamina fusca. The stroma is the thickest layer of the sclera. In the scleral stroma, the collagen fibrils exhibit a wide range of diameters, from 25 to 230 nm.[111,116] The average diameter of the collagen fibrils increases gradually from ∼65 nm in the innermost part to ∼125 nm in the outermost part of the sclera. The mean diameter is ∼100 nm and the mean distance between fibril centers is equal to ∼285 nm.[5] Collagen intermolecular spacing is similar to that in the cornea, in particular for bovine sclera, 1.61 ± 0.02 nm.[112] The fibrils are arranged in individual bundles parallel to the scleral surface, but more randomly than in the cornea. Within each bundle, the groups of fibrils are separated from each other by large empty lacunae randomly distributed in space [see Fig. 2(d)].[111] In spite of the scleral collagen fibrils displaying various diameters, locally they could be quasi-ordered with a short-range spatial ordering in the form of a hexagonal quasi-crystal.

The eye lens is also a tissue for which the short-range spatial ordering is of crucial importance.[5,47] A healthy human lens contains ∼60% water and 38% proteins and consists of many fiber cells.[117] However, the tissue's predominant dry components are $\alpha-$, $\beta-$, and $\gamma-$crystallines—structural proteins, which provide ∼33% of the total weight of the lens.[118] The water-soluble $\alpha-$crystalline is a major component that has a spherical shape with a diameter of ∼17 nm. Age-related biochemical endogenous processes in the organism and exogenous environmental-related stresses induce lens opacity caused by an increase of light scattering and/or pigmentation due to oxidizing and cross-linking of lens proteins. Formed spherical aggregates are variable in size (100 to 250 nm) and occur in clusters that create potential scattering centers.[117]

One more example of complex anisotropic tissue structure is the retinal nerve fiber layer (RNFL),[46,48,49,119] which is formed by the expansion of the fibers of the optic nerve and comprises bundles of unmyelinated axons that run across the surface of the retina. The two prominent cytoskeletal elements of axons are microtubules and neurofilaments.[120] Axonal microtubules are long tubular polymers of the protein tubulin with an outer diameter of ∼25 nm, an inner diameter of ∼15 nm, and

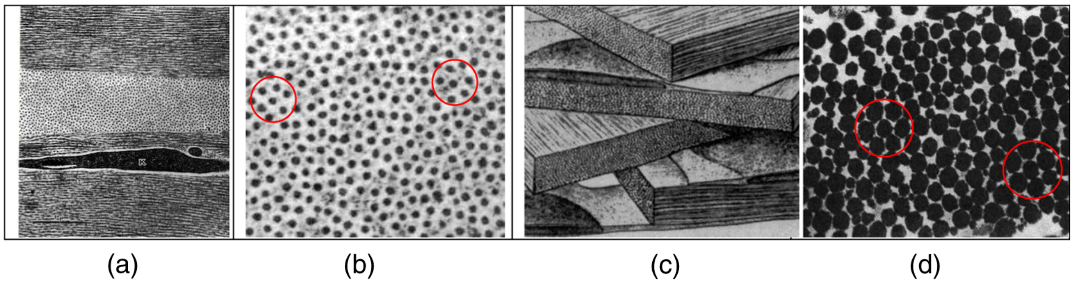

Fig. 2 The electron images of [(a) and (b)] the human cornea (×32,000) and (d) sclera (×18,000): (a) **K** is the keratocyte, (b) magnified image of middle lamella of (a); two circles show a short-range spatial ordering in the form of a hexagonal quasi-crystal; (c) the model of lamellar-fibrillar structure of the corneal stroma; (d) scleral collagen fibrils, which display various diameters; however, locally, they could be quasi-ordered (two circles show a short-range spatial ordering in the form of a hexagonal quasi-crystal).[43,44,111,113–115]

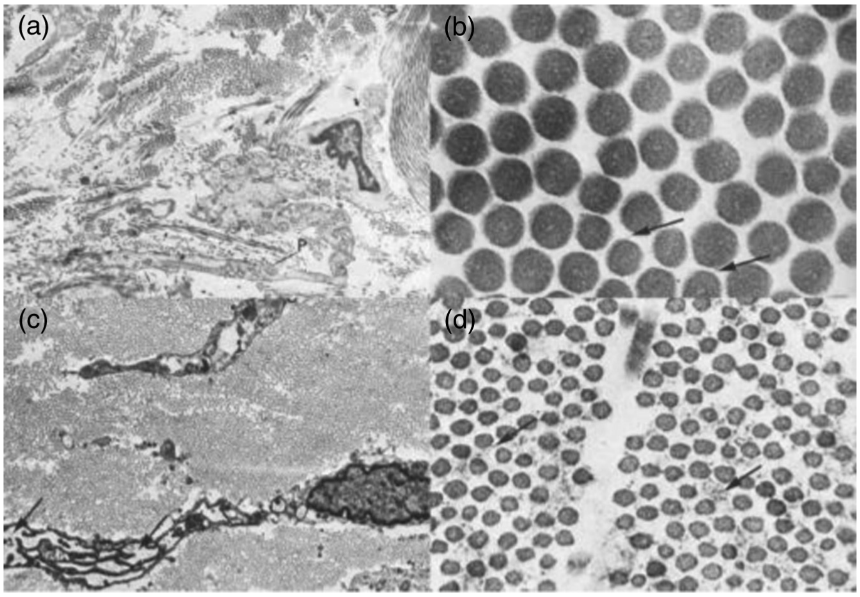

Fig. 3 Area of reticular dermis showing (a) the collagen fibrils in the normal skin and (c) nodule of a hypertrophic scar (electron image, ×10,000); (b) and (d) the close-up view of a region in (a) and (c) at higher magnification power (×105,000), respectively. Arrows in (b) and (d) show interstitial interfibrillar material; in (b) and (d), the circles show a short-range spatial ordering in the form of a hexagonal quasi-crystal.[121]

a length of 10 to 25 μm; neurofilaments are stable protein polymers with a diameter of ~10 nm.

As it follows from electron images of human reticular dermis, presented in Fig. 3, this tissue can also be locally considered as a short-range spatially ordered fibrillar system.[121] Anisotropy of light propagation in human skin was proven experimentally.[122] Skin aging and pathology may dramatically change its structure, i.e., anisotropy. For example, scar tissue typically occupies areas of fibrous tissue that replace normal tissue after injury [Figs. 3(c) and 3(d)]. Another example is benign or malignant tumor, which is abnormally growing tissue sometimes strongly vascularized and having the tendency to spread to other tissue layers, making them more random.

The bone, tooth enamel, dentin, and cementum, as well as tendon and cartilage belong to hard tissues.[119] Most of them are connective tissues, which typically consist of cells rarely distributed in an amorphous mucopolysaccharide matrix in which there are also varying amounts of tissue fibers, mainly collagenous fibers. The apatite or hydroxyapatite (HAP) natural crystals, $\mathrm{Ca_5OH(PO_4)_3}$, are the major components of some hard tissues. The dental enamel consists of 87 to 95% and bone of 50 to 60% of HAP crystals; the rest is water and proteins. Tooth is a hard body composed of dentin surrounding a sensitive pulp and covered on the crown with enamel [see Fig. 4(a)]. The enamel is the hardest tissue in a body, which is an elastic, white material containing no cells. In particular, it is an ordered array of HAP crystals surrounded by a protein/lipid/water matrix. Fairly well-oriented hexagonal HAP crystals of ~30- to 40-nm diameter and up to 10-μm length are packed into an organic matrix to form keyhole-shaped interlocking enamel prisms (or rods) with an overall cross-section of 4 to 6 μm. Enamel prisms are roughly perpendicular to the tooth surface. Because of their size, number, and high refractive index, the prisms are the main light scatterers in enamel. The enamel is translucent and grayish white in color, and it has a yellow hue due to the underlying dentin.

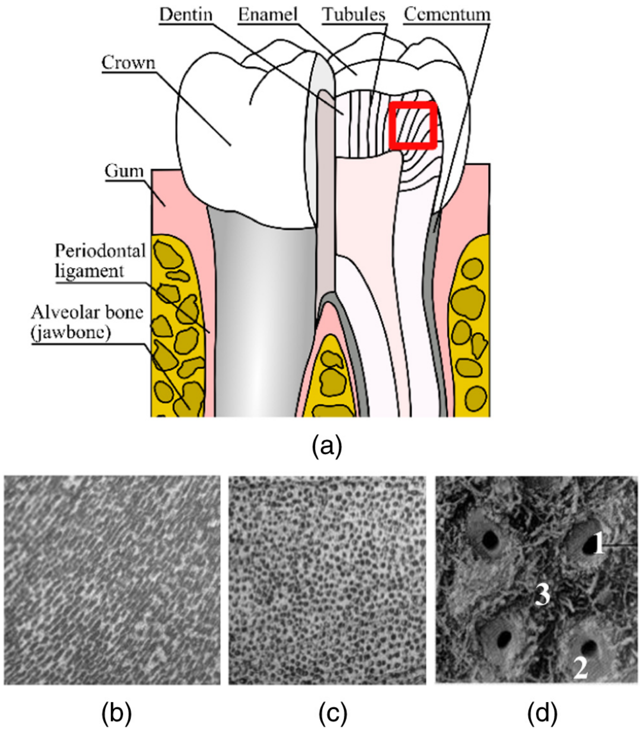

Fig. 4 Schematic representation of tooth structure, including dentinal channels: (a) tubules (rectangle), and optical images of human dentinal slab surface showing tubules for two different sections—(b) under some angle and (c) perpendicular to the slab surface (Axio Imager, Carl Zeiss, magnification 20×), done by I. V. Fedosov and N. A. Trunina; (d) the close-up view of tubules using electron scanning microscopy of human dentin (presented by R. Vilar): dentinal tubules (1), dense and homogeneous pertubular dentin (2), and less dense and less homogeneous intertubular dentin (3).

Tooth dentin is a complex structure, honeycombed with dentinal tubules, which are shelled organic cylinders with a highly mineralized shell. The tooth dentin is a hard, middle calcified, elastic, yellowish material of the same substance as bone.[119] It is the main structural part of a tooth extending from crown to root. The dentin is composed of base material that is pierced by mineralized dentinal tubules 1 to 5 μm in diameter, which makes it porous [see Fig. 4(c)]. The tubules' density is in the range of (3.0 to 7.5) $\times 10^6 \cdot \mathrm{cm}^{-2}$. They contain organic components and natural HAP crystals of 2.0 to 3.5 nm diameter and up to 100 nm length, which intensively scatter light. Average dentin contains 70% HAP crystals, 20% proteins (e.g., collagen), and 10% water. It is softer than enamel but slightly harder than bone. The tubular microstructure of dentin makes it strongly anisotropic for propagating light.[123–125]

The osteon, the basic bone unit with a typical length scale of $\sim$100 μm, is formed by concentric $\sim$10-μm-thick lamellae, composed of collagen fibrils that are $\sim$1 μm wide.[126] Fibrils in their turn consist of an inhomogeneous matrix of cross-linked type I collagen molecules, $\sim$300 nm in length and $\sim$1.5 nm in diameter, mineralized with carbonated HAP nanocrystals. Type I collagen and HAP nanocrystals are, therefore, the basic building blocks of bone at the nanoscale (1 to 300 nm).[126–128]

In bone and tooth, anisotropy is due to mineralized structures originating from HAP nanocrystals, which play an important role in hard tissue depolarization and birefringence. The demineralization process is the loss of mineral from mineralized tissues, such as bone or tooth.[125–129] In tooth tissue, demineralization may lead to caries, and in bone, to osteoporosis. Evidently, measured depolarization and birefringence could be good markers of these and other pathologies.

The cartilage is a strong, resilient, skeletal tissue. There are a few types of cartilage:[119] the hyaline cartilage is the simplest and most common form that consists of a matrix of a polysaccharide-containing protein (trachea, bronchi); the yellow fibrocartilage (elastic cartilage) contains yellow fibers in the matrix (external ear, epiglottis); and the white fibrocartilage contains white fibers in the matrix and occurs in the disks between the vertebrae. Articular cartilage is mainly composed of water, collagen fibrils, proteoglycans, and the chondrocytes with 60 to 85% of water, whereas 50 to 80% and 20 to 35% of the tissue dry weight are collagen and proteoglycans, respectively.[130–133] Chondrocytes contribute <5% of cartilage volume. Most of the collagen is of type II. The collagen fibril diameter varies from 20 to 200 nm. Articular cartilage consists mostly of three layers.[131–133] In the superficial layer (see Fig. 5), collagen fibrils are mostly oriented parallel to the cartilage surface; high collagen and lower proteoglycan content is characteristic.[130,132,133] In the transitional layer, collagen fibril orientation is more random and has a larger diameter. In the thicker deep layer (radial), collagen fibrils are oriented perpendicular to the cartilage surface and have still a larger diameter than in other layers; chondrocytes tend to align in columns (see Fig. 5, right), and the proteoglycan content is higher than that in the superficial and middle layers.[130] A thin layer of calcified cartilage separates cartilage and subchondral bone. Between the noncalcified and calcified layers lies a tidemark, which is a line seen in microscopic images at histological staining. Collagen fibers from the deep layer run through the calcified zone and are attached to the subchondral bone.

The tendon is a cord of white fibrous tissue. It usually attaches muscle to bones and consists mostly of parallel, densely packed collagen fibers arranged in parallel bundles interspersed with long, elliptical fibroblasts. In general, tendon fibers are cylindrical in shape with diameters ranging from 20 to 400 nm. The ordered structure of collagen fibers running parallel to a single axis makes tendon a highly optically birefringent tissue. Collagen fibrils are collagen molecules packed into an organized overlapping bundle. In their turn, collagen fibrils associated in a bigger bundle form a collagen or white fiber—the main component of white fibrous tissue. For example, diameters are in the range from $\sim$25 to 600 nm for tendon collagen fibrils, with bigger sizes for mature tendons, $\sim$25 nm for subfibrils, and in the range from 10 to 15 nm for protofibrils (Fig. 6).[134]

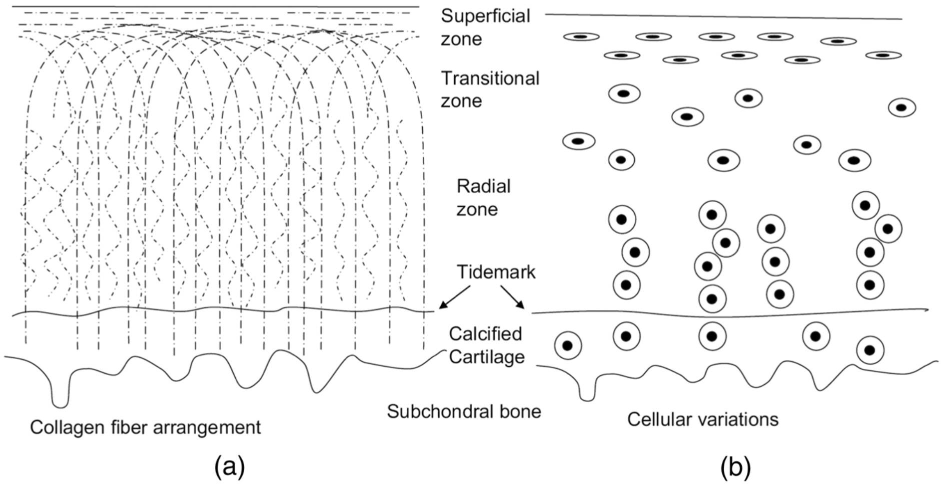

Fig. 5 The orientation of collagen fibrils in normal articular cartilage, as expounded in the classic arcade model of (a) Benninghoff and (b) cellular variations.[133] Collagen fibers arise from the subchondral bone where they are radially oriented, curve over to lie parallel to the cartilage surface in the superficial tangential layer, and then descend back to the underlying bone. The tangential layer is generally less than 100 μm thick, while the majority of the full thickness of the cartilage (1 mm or so) is occupied by the transitional and radial zones. In the superficial zone, the chondrocytes are ellipsoidal in shape, in transitional zone, they are spheroidal, and in radial, they tend to align in columns.

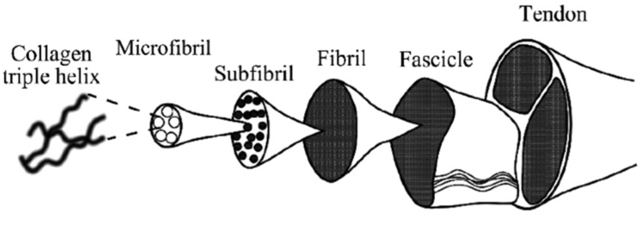

Fig. 6 Collagenous fibrillar structure of tendons: collagen triple helices are combined into microfibrils (or protofibrils), then into subfibrils, fibrils, fascicles, and into tendons.[134]

Collagen is a tough, inelastic, fibrous protein.[135] Collagen in its turn forms white fibers in connective tissue. The tropocollagen or collagen molecule subunit is a rod ∼300 nm long and 1.5 nm in diameter, made up of three polypeptide strands. There is some covalent cross-linking within the triple helices and a variable amount of covalent cross-linking between tropocollagen helices to form the different types of collagen found in different mature tissues. A distinctive feature of collagen is the regular arrangement of amino acids in each of the three chains of these collagen subunits.

There are a number of collagen types which differ in their composition and structure; type I to type V are the most abundant; types I, II, III, V, VII, and XI are capable of fibril formation; their distribution in tissues is as follows: type I—dermis, bone, cornea, tendon, cartilage, vessel wall, intestine, dentin, uterine wall, fat mashwork; type II—cartilage, notochord, vitreous humor, nucleus pulposus; type III—dermis, intestine, gingiva, heart valve, uterine wall, vessel wall; types IV and VII—basement membranes; type V—cornea, placental membranes, bone, vessel wall, cartilage, gingiva; and type XI—cartilage, intervertebral disc, vitreous humor.[119] In optical measurements, the collagen index of refraction is of importance; for example, for type I, it is at the wavelength 850 nm, $n = 1.43$ (fully hydrated) and 1.53 (dry).[135]

As follows from the analysis of tissue properties, many biological tissues are structurally anisotropic. Tissue birefringence results primarily from the linear anisotropy of fibrous structures, which forms the extracellular media. The refractive index of a medium is higher (the speed of light is lower here) along the length of fibers than along their cross-section. A specific tissue structure is a system composed of parallel cylinders that create a uniaxial birefringent medium with the optic axis parallel to the cylinder axes. This type of birefringence is called birefringence of form (Fig. 7). A large variety of tissues such as eye cornea, tendon, cartilage, eye sclera, dura mater, muscle, myocardium, artery wall, nerve, retina, bone, teeth, myelin, and so on exhibit birefringence. All these tissues contain uniaxial and/or biaxial birefringent structures. For example, myocardium contains fibers oriented along two different axes. It consists mostly of cardiac muscle fibers arranged in sheets that wind around the ventricles and atria. Since the refractive index along the axis of the cardiac muscle fibers is different from that in the transverse direction, tissue is birefringent.

Besides anisotropy of form, collagen fibrils as complex molecular structures have intrinsic linear birefringence arising due to anisotropy at the molecular scale and are fundamentally determined by the anisotropic distribution of electrical charge.[132] The spatial length scale of the structure producing intrinsic birefringence is much smaller than the fibrillary scale at which form birefringence is produced, but both scales are smaller than the wavelength of light. Studies on type I collagen in tendon have led to the consensus that this collagen type displays intense intrinsic positive birefringence due to the quasi-crystalline arrangement of the amino-acid residues that comprise the polypeptide chains of the collagen molecule alpha chains.[132] A crucial distinguishing feature between form and intrinsic birefringence is that the value of birefringence of form can be reduced by refractive index matching between the background material and the inclusions as intrinsic birefringence is an intrinsic property of the fibril material and cannot be altered unless gross changes in the molecular structure are induced.

Form birefringence arises when the relative optical phase between the orthogonal polarization components is nonzero for forward-scattered light. For linear structures, an increase in optical field phase delay (δ_{oe}) is characterized by a difference in the effective refractive index for light polarized along, and perpendicular to, the long axis of the linear structures (Δn_{oe}). Phase retardation δ_{oe} between orthogonal polarization components is proportional to the distance d for light with a wavelength λ_0 traveling through the birefringent medium [see Eq. (10)],[15,132]

$$\delta_{\mathrm{oe}} = \frac{2\pi \Delta n_{\mathrm{oe}} d}{\lambda_0}. \tag{20}$$

A structure of parallel dielectric cylinders immersed in isotropic homogeneous ground substance behaves as a positive uniaxial birefringent medium [$\Delta n_{\mathrm{oe}} = (n_e - n_o) > 0$] with its optic axis parallel to the cylinder axes [Fig. 7(a)]. Therefore, an incident electrical field directed parallel to the cylinder axes will be called an extraordinary ray (e), and the incident electrical field perpendicular to the cylinder axes will be called an ordinary ray (o). The difference $(n_e - n_o)$ between the indices of refraction of the extraordinary and ordinary rays is a measure of

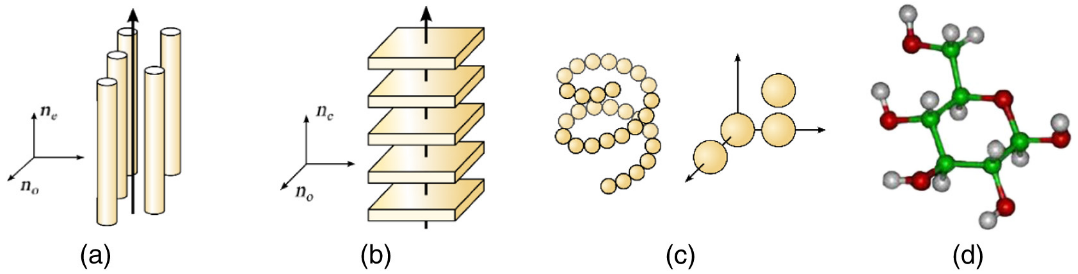

Fig. 7 Examples of structurally anisotropic models of tissues and tissue components: (a) system of long dielectric cylinders; (b) system of dielectric plates; (c) chiral aggregates of particles; and (d) glucose (chiral molecule) as a tissue component.

the birefringence of a medium. For the Rayleigh limit (diameter of cylinders ≪ wavelength λ), the form birefringence is described as[136]

$$\Delta n_{\mathrm{oe}} = (n_e - n_o) = \frac{f_1 f_2 (n_1 - n_2)^2}{f_1 n_1 + f_2 n_2}, \tag{21}$$

where f_1 is the volume fraction of the cylinders; f_2 is the volume fraction of the ground material; and n_1, n_2 are the corresponding refraction indices. For a given difference of refraction index $(n_1 - n_2)$, maximal birefringence is expected for approximately equal volume fractions of thin cylinders and ground material. For systems with a high volume fraction of cylinders or, on the contrary, ground material (rare fibers), the birefringence goes down.

The experimental birefringence values for muscle, coronary artery, myocardium, sclera, skin, cartilage, and tendon are in the range from 1.4×10^{-3} to 4.2×10^{-3}.[5,15,119] For these tissues, it is lowest for the muscle and highest for the tendon. For thermally treated tendon, it is twice as low as for intact tissue.

The diattenuation (linear dichroism) is the difference of attenuation of two waves with orthogonal polarizations traveling in an anisotropic medium, which is described by the difference between the imaginary (losses) parts of the effective indices of refraction for two orthogonal directions. Depending on the relationship between the sizes and the optical properties of the cylinders or plates [see Figs. 7(a) and 7(b)], this difference can take positive or negative values.[15]

The magnitude of birefringence and diattenuation is related to the density and other properties of the collagen fibers, whereas the orientation of the fast axis indicates the orientation of the collagen fibers. The densities of collagen fibers in skin and cartilage are not as uniform as in tendon, and the orientation of the collagen fibers is not distributed as orderly as in tendon. Correspondingly, the amplitude and orientation of birefringence of the skin and cartilage are not as uniformly distributed as in tendon.

In addition to linear birefringence and diattenuation, many tissue components show optical activity (circular birefringence) and circular diattenuation.[9,14,15] In complex tissue structures, chiral aggregates of particles may be responsible for tissue optical activity [see Fig. 7(c)]. The molecule's chirality, which stems from its asymmetric molecular structure [see Fig. 7(d)], also results in a number of effects generically called optical activity. A well-known manifestation of optical activity is the ability to rotate the plane of linearly polarized light about the axis of propagation [see Eqs. (11) and (12)]. The amount of rotation depends on the chiral molecular concentration, the path length through the medium, and the light wavelength. Interest in tissue chirality studies is driven by the attractive possibility of noninvasive *in situ* optical monitoring of glucose in diabetic patients.[9,14,15,17,83]

More sophisticated anisotropic tissue models can also be found. For example, the eye cornea can be represented as a system of plane anisotropic layers (plates, i.e., lamellas), each of which is composed of densely packed long cylinders (fibrils) [see Fig. 2(c)] with their optical axes oriented along a spiral.[137] This fibrillar-lamellar structure of the cornea is responsible for the linear and circular diattenuation and its dependence on the angle between the lamellas.

4 Tissue Models

4.1 *Single Scattering*

4.1.1 *Discrete particle model*

Biological tissue is an inhomogeneous medium with different levels of organization that include cells, cell organelles, and inclusions, different fiber and tubular/lamellar structures (see Figs. 2–6). In view of the great diversity and structural complexity of tissues, the development of an adequate optical model accounting for the scattering and absorption of light is often the most complex step of a study.[1–5] Many tissues are composed of structures with a wide range of sizes and can be represented as a system of discrete scattering particles. Such models have been used to describe the angular dependence of the intensity and polarization properties of scattered radiation.[1–22,138]

Biological media are often modeled as ensembles of homogeneous spherical particles with a refractive index higher than surroundings, since many cells, cell organelles, and biological macromolecules are close in shape to spheres or ellipsoids.[2,5,96,138,139] A system of noninteracting spherical particles is the simplest tissue model. The Rayleigh and Mie theories or their combinations are basic to calculate tissue scattering properties. In particular, Mie theory rigorously describes the diffraction (elastic scattering) of light by a spherical particle. The advances of this theory account for the structures of the spherical particles, namely, the multilayered spheres and the spheres with radial nonhomogeneity, anisotropy, and optical activity.[96–101]

For connective tissue composed from fiber structures, a system of long cylinders is the most appropriate model to describe light scattering. Tendon, cartilage, skin dermis, dura mater, muscular tissue, eye cornea, and sclera belong to this type of tissue formed essentially by collagen fibrils. The solution of the problem of light scattering by a single homogeneous or multilayered cylinder is also well understood.[96–101]

At transport in the inhomogeneous (turbid) medium with absorption, a photon (light wave) changes its direction (wave vector) due to reflection, refraction, and diffraction on microscopic internal structures, and can be absorbed by an appropriate molecule on its way. Light scattering means a change in direction of light propagation so that its trajectory is deflected by an angle θ in the scattering plane and by an azimuthal angle φ (0 to 2π) in the perpendicular plane (Fig. 1).[96]

To characterize scattering and absorption efficiency of a medium, scattering (μ_s) and absorption (μ_a) coefficients are introduced, which follow from the exponential Bouguer–Beer–Lambert law for light propagation in a tissue layer of thickness d.[2,5]

$$I(d) = I_0 \exp(-\mu_t d), \tag{22}$$

where $I(d)$ is the intensity of transmitted light measured using a distant photodetector with a small aperture (on-line or collimated transmittance), and I_0 is the incident light intensity.

$$\mu_t = \mu_a + \mu_s \tag{23}$$

is the interaction or total attenuation coefficient. Equation (22) is valid if scattering is not strong and only the unscattered portion of transmitted light beam (so-called ballistic photons) is detected. Such a regime could be more or less realized for thin tissue layers when absorption is high enough to eliminate multiple scattering events.

In addition to the scattering coefficient, the scattering process is also characterized by a scattering phase function—the function that describes the scattering properties of the medium and is in fact the probability density function for a photon traveling in some direction to be scattered in some new direction $p(\theta, \varphi)$. Figure 1 illustrates the geometry of scattering of light by a particle, where the incident light beam, $\vec{S}_0$, is parallel to the z-axis, and θ and φ are the scattering angles in the scattering plane and in the plane perpendicular to the scattering plane, respectively.[37] The scattering phase function characterizes an elementary scattering act. If scattering is symmetric relative to the direction of the incident wave, then the phase function depends only on the scattering angle θ [angle between two directions, new ($\vec{S}_1$) and former one ($\vec{S}_0$)], $p(\theta)$.

4.1.2 *Rayleigh scattering*

If a particle is small with respect to the wavelength of the incident light, its scattering can be described as if it is a single dipole.[140] This Rayleigh theory is applicable under the condition that $m(2\pi a/\lambda) \ll 1$, where m is the relative refractive index of the scatterers, $(2\pi a/\lambda)$ is the size parameter, a is the radius of the particle, and λ is the wavelength of the incident light in a medium. For this theory, the scattered irradiance strongly increases as a^6 and decreases as λ^{-4} (Fig. 8); the angular distribution of the scattered light is polarization sensitive and isotropic (Fig. 9).

The angular dependence of the scattered intensity by an ensemble of N randomly distributed particles with a mean distance between particles bigger than the wavelength λ, unpolarized incident light of intensity I_0, and distant detector position r is described by the Rayleigh equation,[140]

$$I(r,\theta) = (2\pi)^4 \frac{a^6}{\lambda^4 r^2} \left(\frac{m^2 - 1}{m^2 + 2} \right)^2 N \frac{1 + \cos^2\theta}{2} I_0, \tag{24}$$

where $m = n_s/n_0$ is the relative index of refraction of the scatterers and ground material, and N is the number of particles in the scattering volume V, i.e., $N = \rho_p V$, where ρ_p is the scattering particle density.

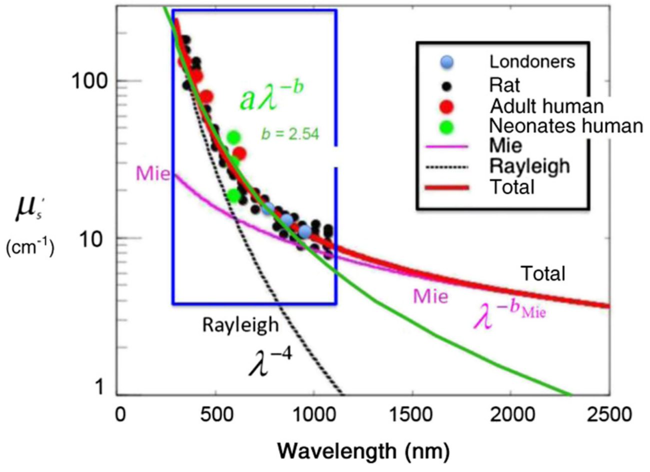

Fig. 8 The wavelength dependence of reduced scattering coefficient, $\mu_s' = \mu_s\ (1 - g)$, for human and rat skin; dots present experimental data, and solid and dotted lines represent theoretical dependences from Mie and Rayleigh theories; total means wavelength dependence calculated based on both theories, where coefficients of each theory provide fitting to experimental data (Steven L. Jacques, Ulm, LALS-2014).[139]

Figure 9 illustrates the isotropy of Rayleigh scattering for unpolarized incident light and the polarization-insensitive detection (curve 3) and polarization ability of the scattering particles for the particular direction of detection (90 and 270 deg), where only light polarized perpendicular to the scattering plane is scattered (compare curves 1 and 2). An ideal isotropy (circle-shaped phase function) of the scattering is achieved if incident light is linearly polarized perpendicular to the scattering plane (curve 1). For any scattering angle, except $\theta = 0$ and 180 deg, interaction of unpolarized light with Rayleigh scatterers provides linear polarization of the scattered light with preferable intensity of the electrical vector oscillating in the plane perpendicular to the scattering plane with polarization degree

$$P_L = \frac{I_\perp(\theta) - I_\parallel(\theta)}{I_\perp(\theta) + I_\parallel(\theta)} = \frac{\sin^2\theta}{1 + \cos^2\theta}. \tag{25}$$

For the near-infrared (NIR) light and typical biological scatterers with $m = 1.05$ to 1.10, the maximum particle radius is ~12 to 14 nm for the Rayleigh theory to remain valid. The Rayleigh–Gans or Rayleigh–Debye theory addresses the problem of calculating the scattering by a special class of arbitrarily shaped particles; it requires $|m - 1| \ll 1$ and $\frac{2\pi a'}{\lambda}|m - 1| \ll 1$, where a' is the largest dimension of the particle. These conditions mean that the electric field inside the particle must be close to that of the incident field and the particle can be viewed as a collection of independent dipoles that are all exposed to the same incident field. A biological cell might be modelled as a sphere of cytoplasm with a higher refractive index ($n_c = 1.370$) relative to that of the surrounding interstitial medium ($n_i = 1.350$); then $m = 1.015$, and for the NIR light, this theory will be valid for the particle dimension up to $a' =$ 850 to 950 nm. This approximation has been applied extensively to calculate light scattering from suspensions of bacteria[37–41] and can be applicable to describe light scattering from cell organelles (mitochondria, lysosomes, peroxisomes, and so on) in tissues due to their small dimensions and refraction.

4.1.3 *Mie scattering*

Mie or Lorenz-Mie scattering theory relates to scattering by comparatively large spherical particles, which are of the order of the wavelength, and is based on an exact solution of Maxwell's electromagnetic field equations for a homogeneous sphere.[2,5,96,140] Typically, tissues contain both types of scatterers, small and large (for instance, cell components and collagen

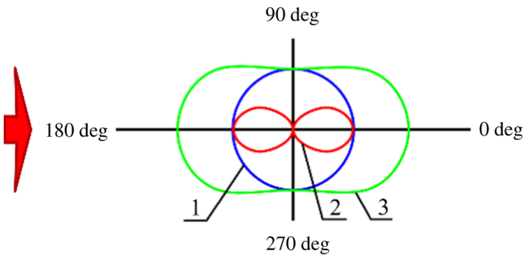

Fig. 9 Rayleigh scattering: light distribution in the scattering plane for two orthogonal linear polarization states and unpolarized incident light;[140] 1, electric vector perpendicular to the scattering plane; 2, electric vector parallel to the scattering plane; and 3, unpolarized light.

fibers of connective tissues, see Fig. 8). Mie theory operates with the following relevant particle parameters: radius a and complex refractive indices of its material $n_s(\lambda_0)$ and dielectric host (ground material) $n_0(\lambda_0)$,

$$n_{s,0}(\lambda_0) = n'_{s,0}(\lambda_0) + in''_{s,0}(\lambda_0), \tag{26}$$

where λ_0 is the wavelength in vacuum. The imaginary part of the complex refractive index of the material is responsible for light losses due to absorption. Mie theory yields the scattering ($Q_{\text{sca}} = \sigma_{\text{sca}}/\pi a^2$) and absorption ($Q_{\text{abs}} = \sigma_{\text{abs}}/\pi a^2$) efficiencies and the phase function from which the absorption and scattering cross-sections (σ_{sca} and σ_{abs}) and the scattering anisotropy factor $g \equiv <\cos\theta>$ are calculated,

$$\sigma_{\text{sca}}^{\text{Mie}} = \frac{\lambda_0^2}{2\pi n_0^2}\sum_{n=1}^{\infty}(2n+1)(|a_n|^2 + |b_n|^2), \tag{27}$$

$$\sigma_{\text{abs}}^{\text{Mie}} = \frac{\lambda_0^2}{2\pi n_0^2}\sum_{n=1}^{\infty}(2n+1)[\text{Re}(a_n + b_n) - (|a_n|^2 + |b_n|^2)], \tag{28}$$

$$p^{\text{Mie}}(\theta) = \frac{\lambda_0^2}{2\pi n_0^2 \sigma_{\text{sca}}^{\text{Mie}}}(|S_1|^2 + |S_2|^2), \tag{29}$$

$$g^{\text{Mie}} = \frac{\lambda_0^2}{\pi n_0^2 \sigma_{\text{sca}}^{\text{Mie}}}\left[\sum_{n=1}^{\infty}\frac{2n+1}{n(n+1)}\text{Re}(a_n b_n^*) + \sum_{n=1}^{\infty}\frac{n(n+2)}{n+1}\text{Re}(a_n a_{n+1}^* + b_n b_{n+1}^*)\right], \tag{30}$$

where a_n and b_n are Mie coefficients, which are functions of the relative complex refractive index of particles (m) and parameter $\alpha = 2\pi n_0 a/\lambda_0$; an asterisk indicates that the complex conjugate is to be taken.

$$a_n = \frac{\psi_n(\alpha)\psi'_n(m\alpha) - m\psi_n(m\alpha)\psi'_n(\alpha)}{\zeta(\alpha)\psi'_n(m\alpha) - m\psi_n(m\alpha)\zeta'_n(\alpha)}, \tag{31}$$

$$b_n = \frac{m\psi'(m\alpha)\psi_n(\alpha) - \psi_n(m\alpha)\psi'_n(\alpha)}{m\psi'_n(m\alpha)\zeta_n(\alpha) - \psi_n(m\alpha)\zeta'_n(\alpha)}. \tag{32}$$

ψ_n and ζ_n are the Riccati–Bessel functions; S_1 and S_2 are functions of the polar scattering angle and can be obtained from the Mie theory as

$$S_1(\theta) = \sum_{n=1}^{\infty}\frac{2n+1}{n(n+1)}[a_n\pi_n(\cos\theta) + b_n\tau_n(\cos\theta)], \tag{33}$$

$$S_2(\theta) = \sum_{n=1}^{\infty}\frac{2n+1}{n(n+1)}[b_n\pi_n(\cos\theta) + a_n\tau_n(\cos\theta)]. \tag{34}$$

The parameters π_n and τ_n can be given as

$$\pi_n(\cos\theta) = \frac{1}{\sin\theta}P_n^1(\cos\theta), \tag{35}$$

$$\tau_n(\cos\theta) = \frac{d}{d\theta}P_n^1(\cos\theta), \tag{36}$$

where $P_n^1(\cos\theta)$ is the associated Legendre polynomial; the following recursive relationships are used to calculate π_n and τ_n,

$$\pi_n = \frac{2n-1}{n-1}\pi_{n-1}\cos\theta - \frac{n}{n-1}\pi_{n-2},$$
$$\tau_n = n\pi_n\cos\theta - (n+1)\pi_{n-1}, \tag{37}$$

and the initial values are

$$\begin{cases}\pi_1 = 1, & \pi_2 = \cos\theta,\\ \tau_1 = \cos\theta, & \tau_2 = 3\cos 2\theta.\end{cases} \tag{38}$$

From the expressions for σ_{sca} (cm^2) and σ_{abs} (cm^2), scattering and absorption coefficients can be calculated as $\mu_s = \rho_p\sigma_{\text{sca}}$ and $\mu_a = \rho_M\sigma_{\text{abs}}$, where ρ_p is the scattering particle density and ρ_M is the number of absorbing molecules per unit volume (cm^{-3}).

Mie theory predicts that scattering introduced by spherical micrometer-sized particles is strongest and highly anisotropic if the particle radius and wavelength are of the same order of magnitude (Figs. 9 and 10). The scattering coefficient decays with the wavelength much more slowly than for Rayleigh scattering, i.e., λ^{-b}, with b in the range of 1 to 3. The scattering coefficient increases strongly with the elevation of the relative index of refraction m. In contrast, for the matched refractive indices of scatterers and background material, the scattering coefficient goes to zero as scattering anisotropy factor approaches 1 (extremely high scattering directness).

Similar to the Rayleigh equation [Eq. (24)] for unpolarized incident light of intensity I_0 and distant detector position r, the angular dependence of intensity of the light scattered by an ensemble of N randomly distributed Mie particles with a mean distance between particles bigger than the wavelength λ is described by

$$I(\theta) = p^{\text{Mie}}(\theta)\cdot N\cdot I_0. \tag{39}$$

Mie theory is strictly applicable only to particles of particular regular shapes, but the results are still useful if the shape is irregular.

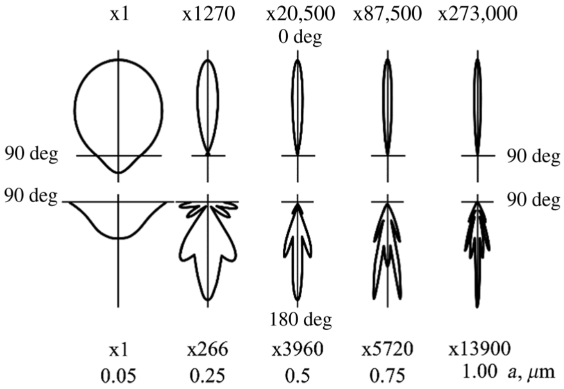

Fig. 10 The polar diagrams of the calculated angular-dependent intensity distributions (Mie phase functions) for five single isotropic spheres with the diameter in the range of those that are typical for cell organelles, from $2a = 0.1$ to 2.00 μm, $\lambda_0 = 500$ nm, and $m = 1.5$.[140]

Actual biological tissue models are more complex than a monodispersive system of distant spherical particles or even randomly shaped ones. Sometimes, a mixture of large particles contributing high scattering anisotropy and small particles with increased scattering toward shorter wavelengths may be a good approximation to describe tissue scattering properties (see Fig. 8).[139]

The scattering anisotropy factor (mean cosine of the scattering angle θ, see Fig. 1) is expressed as that corresponding to scattering symmetry and assumption of random distribution of particles in a medium,[96,98]

$$g \equiv \langle \cos\,\theta \rangle = 2\pi \int_0^\pi M_{11}(\theta) \cos\,\theta\, \sin\,\theta d\theta,$$

$$2\pi \int_0^\pi M_{11}(\theta) \sin\,\theta d\theta = 1, \tag{40}$$

where $M_{11}(\theta)$ is the first element of LSM [see Eq. (9)].

In addition to theoretical Mie phase function [see Eq. (30)], several semi-empirical approximations for the scattering phase function have been used. One of the most often exploited is the Henyey-Greenstein (HG) phase function,

$$p^{\mathrm{HG}}(\theta) = \frac{1}{4\pi} \cdot \frac{1 - g^2}{(1 + g^2 - 2\,g\,\cos\,\theta)^{3/2}}. \tag{41}$$

The transport mean free path (TMFP), l_{tr}, of a photon traveling in a scattering medium characterizes the distance within which the direction of light propagation becomes totally random after many sequential scattering events,[2,5,8,11,15,52,54]

$$l_{\mathrm{tr}} = \frac{1}{\mu_a + \mu_s'} \cong \frac{1}{\mu_s'}, \tag{42}$$

where $\mu_s' = (1 - g)\mu_s$ is the reduced scattering coefficient, and g is the scattering anisotropy factor defined by Eqs. (37) and (40).

4.2 *Quasi-Ordered Tissue Model*

Many tissues composed from optically soft particles (refractive index mismatch of scatterers and surrounding medium is small) and thin enough, such as cornea, eye lens, mucosa, epithelia, can be approximated as single-scattering systems. For example, healthy tissues of eye cornea and lens are highly transparent for visible light because of their ordered structure and the absence of strongly absorbing chromophores.[5] However, scattering is an important feature of light propagation in eye tissues. Typical eye tissue models are long, round dielectric cylinders (corneal and scleral collagen fibers) [Fig. 7(a)] or spherical particles (lens protein structures) having a refractive index n_s; they are randomly (sclera, opaque lens) or regularly (transparent cornea and lens) distributed in the isotropic base matter with a refractive index $n_0 < n_s$.

All these tissues can be considered as densely packed disperse systems in which light propagation can be analyzed using the radial distribution function $g(r)$. This function statistically describes the spatial arrangement of particles in the system (Fig. 11). The $g(r)$-function is the ratio of the local number density of the particles at a distance r from a reference particle placed at $r = 0$ to the bulk number density of particles.[43] For a corneal model as a system of interacting fibrils, it expresses the relative probability of finding two fibril centers separated by a distance r; thus, $g(r)$ must vanish for values of $r \leq 2a$ (a is the radius of a fibril; fibrils cannot approach each other closer than touching).

The $g(r)$-function of scattering centers for a certain tissue is calculated from tissue electron micrographs (see Fig. 2). The $g(r)$-function was first found for the rabbit cornea by McCally and Farrell[43] In Fig. 12(a), a typical experimental $g(r)$-function for one of the cornea regions is shown, $g(r) = 0$ for $r \leq 25$ nm, which is consistent with a fibril radius of 14 ± 2 nm. The first peak in the distribution gives the most probable separation distance between fibrils, which is ~50 nm. $g(r)$ is essentially unity for $r \geq 170$ nm, indicating that the fibril positions are correlated over no more than a few of their nearest neighbors. Therefore, a short-range spatial order exists in the system and should be accounted for the optical model.

Similar calculations for several regions of the human eye sclera are illustrated in Fig. 12(b). Electron micrographs from Ref. 111 [see Fig. 2(d)], averaged for 100 fibril centers, were processed.[5] The obtained results present evidence of the

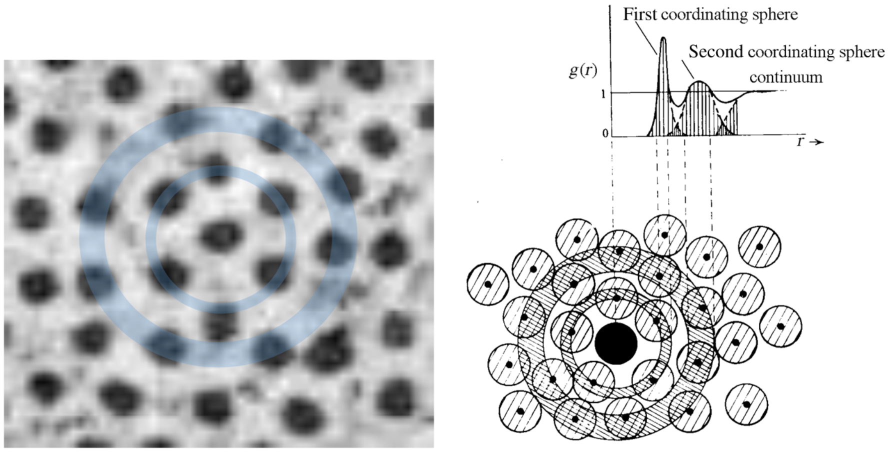

(a) (b)

Fig. 11 (a) A short-range spatially ordered fibrillar system around fixed fibril is shown schematically by two successive rings, characterizing the probability of spatial distribution of neighbor fibrils. (b) The close-up view of collagen fibrils from electron microscopy image of human cornea presented in Fig. 2; diagram of radial distribution function $g(r)$ that is proportional to the probability of particle displacement r at a certain distance from an arbitrarily fixed fibril.[143]

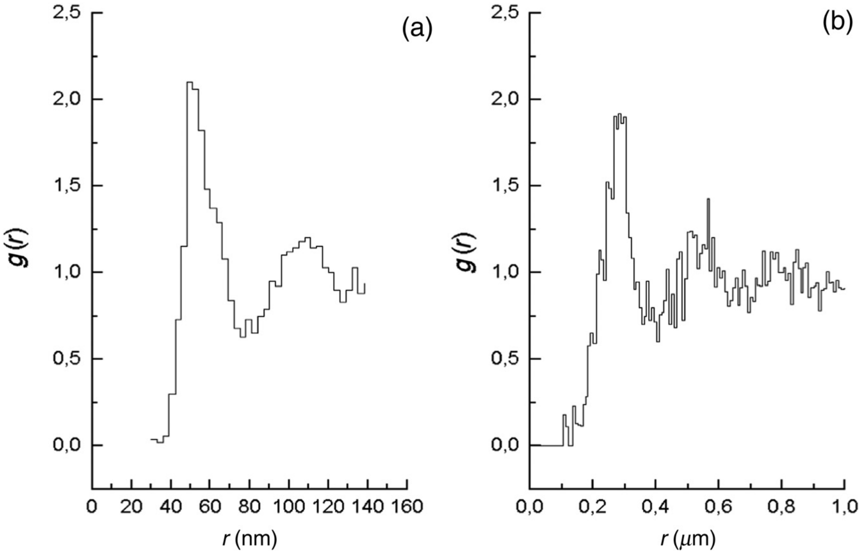

Fig. 12 Experimental histograms of radial distribution function $g(r)$ obtained from electron micrographs of (a) rabbit cornea (700 particles)[43] and (b) human sclera (100 particles)[5,111] [see Figs. 2(b) and 2(d)]. For rabbit cornea, fibril mean diameter is ~28 nm, and it is ~100 nm for human sclera; for a fibril placed at $r = 0$, the nearest most probable particle position is at $r \approx 50$ nm for rabbit cornea and at $r \approx 285$ nm for human sclera.

presence of a short-range spatial order in the sclera, although the degree of order is less pronounced than in the cornea, because of polydispersity of fibrillary structure. $g(r) = 0$ for $r \leq 100$ nm, which is consistent with the mean fibril diameter of ~100 nm derived from the electron micrograph. The first peak in the distribution gives the most probable separation distance, which is ~285 nm. The value of $g(r)$ is essentially unity for $r \geq 750$ nm, indicating a short-range spatial order in the system.

For an isotropic system of N identical interacting long cylinders, the scattered intensity is defined as[5,43]

$$\langle I \rangle = |E_0|^2 N S_2(\theta), \tag{43}$$

where E_0 is the scattering amplitude of an isolated particle.

$$S_2(\theta) = \left\{1 + 8\pi a^2 \rho_c \int_0^R [g(r) - 1] J_0\left(\frac{2\pi a}{\lambda} r \sin\frac{\theta}{2}\right) \mathrm{d}r\right\} \tag{44}$$

is the structure factor; a is the radius of the cylinder face; ρ is the mean density of the cylinder faces; $\rho_c = f_c/\pi a^2$, where f_c is the surface fraction of the cylinders' faces; J_0 is the zero-order Bessel function; R is the distance for which $g(r) \to 1$; θ is the scattering angle.

The structure factor $S_2(\theta)$ describes complex interference of the scattered fields from individual fibrils distributed in two-dimensional space. With no spatial correlation of fibrils, when $g(r) \to 1$, $S_2(\theta) \to 1$; thus, no interference of individual scattered fields exists, and in Eq. (43), intensities of light scattered by individual fibrils rather than fields are summarized. For an isotropic system of identical spherical particles in a single-scattering approximation,[5,104,143]

$$\langle I \rangle = |E_0|^2 N S_3(\theta), \tag{45}$$

$$S_3(\theta) = \left\{1 + 4\pi \rho_p \int_0^R r^2 [g(r) - 1] \frac{\sin qr}{qr} \mathrm{d}r\right\}, \tag{46}$$

where $q = \frac{4\pi}{\lambda} \sin\frac{\theta}{2}$, ρ_p is the mean density of particles, and R is the distance for which $g(r) \to 1$. Quantity $S_3(\theta)$ is the three-dimensional (3-D) structure factor. This factor describes the alteration of the angular dependence of the scattered intensity that appears with a higher particle concentration due to complex interference of the scattered fields from individual spheres distributed in 3-D space. Similar to the fibril system, at no spatial correlation of spherical particles, $g(r) \to 1$, $S_3(\theta) \to 1$; no interference of scattered fields and intensities of light scattered by individual spheres are summarized.

The presented models can be used to describe unpolarized and polarized light interactions with particle media showing a single scattering. Figure 13 illustrates the angular dependences of the scattered intensity for systems of small spherical particles ($a = 20$ nm) with volume fraction $f = 0.1$ and large spherical particles ($a = 500$ nm) with volume fraction $f = 0.4$. The incident wave is linearly polarized parallel with or perpendicular to the scattering plane (see Fig. 1). The dotted lines show angular light distributions for the independent (randomly distributed) particles and the solid lines are that for the ordered particles, for which the interference of the scattered fields plays a significant role. The overall scattering is suppressed due to interference between the out-of-phase scattered fields from individual particles. For the small particle system, such suppression is quite isotropic for both polarization states, and for the large particle system, is mostly suppressed in the forward directed scattering. As a result, both particle systems became more transparent for the incident light (see a big portion of ballistic photons, schematically shown in Fig. 13). It is important to note that for big particle systems, the results for the scattered intensity are presented in the logarithmic scale. Data presented in Fig. 13 allow for evaluation of unpolarized light (50% mixture of two orthogonal linear polarized light beams) interaction with a closely packed particle system that leads to creation of a partly polarized light at scattering as it follows from data in Fig. 9. It is well seen that for the ordered small particles, the polarization

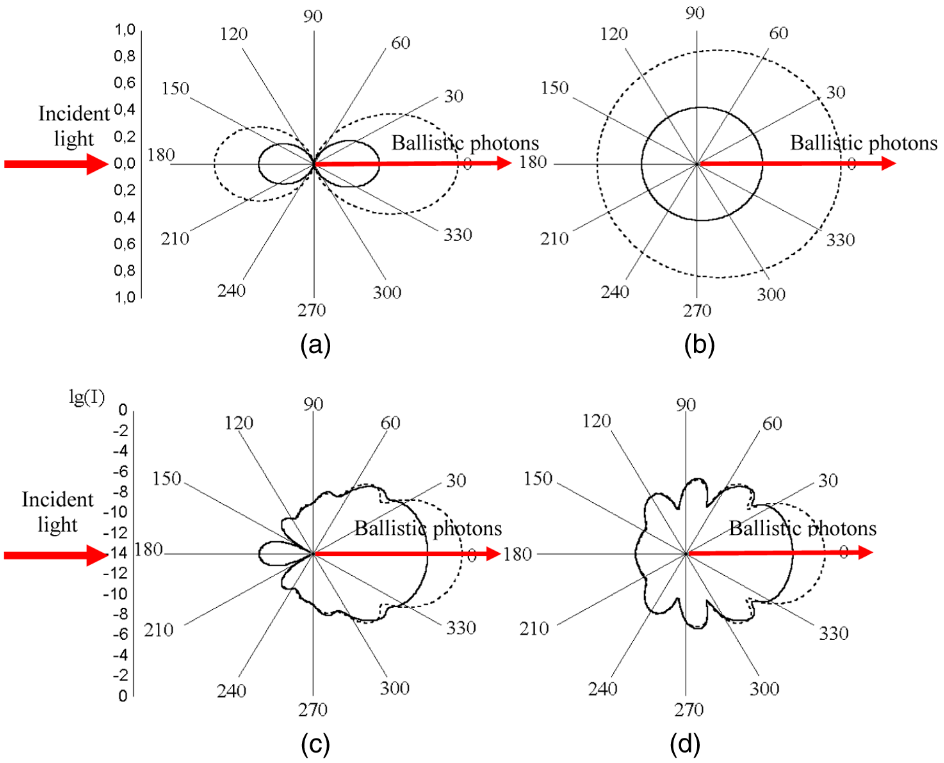

Fig. 13 The calculated angular dependences of the scattered intensity for systems of [(a) and (b)] small spherical particles ($a = 20$ nm) with volume fraction $f = 0.1$ and [(c) and (d)] large spherical particles ($a = 500$ nm) with volume fraction $f = 0.4$; the incident wave is linearly polarized [(a) and (c)] parallel with or [(b) and (d)] perpendicular to the scattering plane (see Fig. 1); dotted lines show calculations for independent particles; wavelength, 633 nm; relative refraction index, $m = 1.105$ (calculated by I. L. Maksimova).[5]

ability at the scattering angles around 90 deg is stronger than for random (independent) particles.

The interference between elementary scattered fields is able to modulate the transformation of the arbitrary polarized incident light into another state of polarization at light scattering that is described in frames of amplitude (2 × 2, Jones) or intensity (4 × 4, Mueller) matrices.[5,15]

4.3 *Light Scattering Matrix*

As is already presented in Sec. 2, the polarization of the scattered light from an object (Fig. 1) is fully described by the Stokes vectors of the incident and scattered light and 4 × 4 Mueller matrix [intensity or LSM, see Eq. (9)].[96] Elements of the LSM depend on the scattering angle θ, the wavelength, the shape, and the optical properties of the object. For scattering by a collection of randomly oriented particles, there are 10 independent LSM elements. The LSM for macroscopically isotropic and symmetric media has a well-known block-diagonal structure.[107]

$$M(\theta) = \begin{bmatrix} M_{11}(\theta) & M_{12}(\theta) & 0 & 0 \\ M_{12}(\theta) & M_{22}(\theta) & 0 & 0 \\ 0 & 0 & M_{33}(\theta) & M_{34}(\theta) \\ 0 & 0 & -M_{34}(\theta) & M_{44}(\theta) \end{bmatrix}. \tag{47}$$

It follows that only eight LSM elements are nonzero and only six of these are independent. Moreover, there are special relationships for two specific scattering angles, 0 and π,[98]

$$\begin{aligned} &M_{22}(0) = M_{33}(0), M_{22}(\pi) = -M_{33}(\pi), \\ &M_{12}(0) = M_{34}(0) = M_{12}(\pi) = M_{34}(\pi) = 0, \\ &M_{44}(\pi) = M_{11}(\pi) - 2M_{22}(\pi). \end{aligned} \tag{48}$$

Rotationally symmetric particles have an additional property,[98]

$$M_{44}(0) = 2M_{22}(0) - M_{11}(0). \tag{49}$$

The structure of the LSM further simplifies for spherically symmetric particles, which are homogeneous or radially inhomogeneous (composed of isotropic materials with a refractive index depending only on the distance from the particle center), because in this case,[98]

$$M_{11}(\theta) \equiv M_{22}(\theta), M_{33}(\theta) \equiv M_{44}(\theta). \tag{50}$$

Mie theory is an exact solution of Maxwell's electromagnetic field equations for a homogeneous sphere.[96,141] For spherically symmetric particles made from optically inactive materials, the Mueller matrix is given by Eqs. (47) and (50). Mie theory has been extended to arbitrary coated spheres and to arbitrary cylinders.[38,98,99] In this theory, the electromagnetic fields of the incident, internal, and scattered waves are each expanded in a series.[141] A linear transformation can be made between the fields in each of these regions. This approach can also be used for nonspherical particles such as spheroids.[98,99] The linear transformation is called the transition matrix (T-matrix).

For systems of spherical and cylindrical particles, when a single-scattering approximation is valid, the angular intensity characteristics are described by Eqs. (43)–(46). The structure factor modifying these characteristics depends only on the spatial particle arrangement, and it is independent of the state of light polarization. Therefore, for systems of identical particles, the angular dependences of all LSM elements are multiplied by the same quantity, accounting for interference interaction [see Eq. (46) for spherical particles].

$$M_{ij}(\theta) = M_{ij}^{0}(\theta) N S_3(\theta), \tag{51}$$

where $M_{ij}^{0}(\theta)$ are the LSM elements for an isolated particle. Consequently, the LSM for the system of monodispersive interacting particles coincides with that of the isolated particle [see Eq. (47)] if normalization to the magnitude of its first element is done.[144]

Unlike for monodispersive systems, in differently sized densely packed particle systems, the normalization to the first element does not eliminate the impact of the structure factor on the angular dependences of the matrix elements. In the simplest case of a bimodal system of particles, expressions analogous to Eqs. (44) and (46) can be found using four structural functions instead of one (see Figs. 11 and 12): $g_{11}(r), g_{22}(r), g_{12}(r)$, and $g_{21}(r)$.[104] These functions characterize the interaction between particles of similar and different sizes. In tissues, a bimodal system formed by a great number of equally sized small particles, and a minor fraction of coarse ones, provides a good model of pathological tissue, e.g., a cataract eye lens or enlargement of a cell nucleus at cancer.

Figure 14 shows results of numerical modeling for a binary mixture of spherical particles with two different diameters and volume fractions.[104] It is seen that the normalized LSM elements of a dense binary mixture are substantially altered due to the interference interaction.

So far, Stokes vectors have been defined for the case of a monochromatic plane wave, and the Mueller matrix for a single scattering. However, this approach has to be generalized to more complicated cases. For a partially polarized [see Eq. (6)] quasi-monochromatic wave, the following inequality is valid:[96,109]

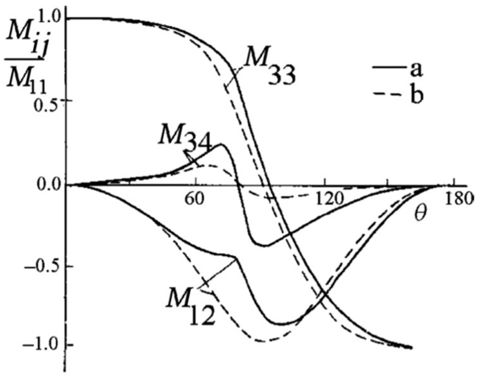

Fig. 14 Calculated angular dependences of LSM elements for a binary mixture of spherical particles:[104] particle diameters: $2a_1 = 60$ nm and $2a_2 = 500$ nm; volume fractions: $f_1 = 0.3$ and $f_2 = 0.02$; relative index of refraction, $m = 1.07$ for both types of particles; $\lambda = 633$ nm; solid lines demonstrate the impact of particle interactions, and dashed lines indicate neglecting of cooperative effects.

$$I^2 \geq Q^2 + U^2 + V^2. \tag{52}$$

When Mueller matrices from an ensemble of particles differing in size, orientation, morphology, or optical properties are added incoherently, many of the above-mentioned equalities became inequalities.[145]

4.4 *Multiple Scattering*

4.4.1 *Vector radiative transfer theory*

Polarization effects at light propagation through tissues with multiple scattering are fully described by the vector radiative transfer equation (VRTE).[5,15,99,100,146] The radiative transfer theory (RTT) originated as a phenomenological approach based on considering the transport of energy through a medium composed of a large number of discrete, sparsely, and randomly distributed particles. Such a medium is treated as continuous, locally homogeneous, and ensuring energy conservation. The scattering and absorption of the small volume element in RTT follow from the Maxwell equations and are given by the incoherent sums of the respective characteristics of the constituent particles. The result of scattering is not the transformation of a plane incident wave into a spherical scattered wave but, rather, the transformation of the intensity Stokes vector of the incident light into the Stokes vector of the scattered light. For macroscopically isotropic and symmetric plane-parallel scattering media, the VRTE can be substantially simplified as follows:[99]

$$\frac{d\mathbf{S}(\bar{\mathbf{r}},\vartheta,\phi)}{d\tau(\bar{\mathbf{r}})} = -\mathbf{S}(\bar{\mathbf{r}},\vartheta,\phi) + \frac{\Lambda(\bar{\mathbf{r}})}{4\pi}\int_{-1}^{+1} d(\cos\vartheta') \times \int_{0}^{2\pi} d\phi' \bar{Z}(\bar{\mathbf{r}},\vartheta,\vartheta',\phi-\phi')\mathbf{S}(\bar{\mathbf{r}},\vartheta',\phi'), \tag{53}$$

where $\mathbf{S}$ is the Stokes vector; $\bar{\mathbf{r}}$ is the position vector; ϑ and φ are the angles characterizing incident direction, respectively, the polar (zenith) and the azimuth angles (see Fig. 1).

$$d\tau(\bar{\mathbf{r}}) = \rho(\bar{\mathbf{r}})\langle\sigma_e(\bar{\mathbf{r}})\rangle ds \tag{54}$$

is the optical path length element, ρ is the local particle number density, $\langle\sigma_e\rangle$ is the local ensemble-averaged extinction coefficient, and ds is the path length element measured along the unit vector of the direction of light propagation; $\Lambda = \mu_s/(\mu_a + \mu_s)$ is the single-scattering albedo; φ' and φ' are the angles characterizing the scattering direction; and $\bar{Z}$ is the normalized phase matrix.

$$\bar{Z}(\bar{\mathbf{r}},\vartheta,\vartheta',\phi-\phi') = R(\Phi)M(\theta)R(\Psi), \tag{55}$$

where $M(\theta)$ is the single-scattering Mueller matrix, θ is the scattering angle, and $\mathbf{R}(\phi)$ is the Stokes rotation matrix for an angle ϕ.

$$R(\varphi) = \begin{bmatrix} 1 & 0 & 0 & 0 \\ 0 & \cos 2\varphi & -\sin 2\varphi & 0 \\ 0 & \sin 2\varphi & \cos 2\varphi & 0 \\ 0 & 0 & 0 & 1 \end{bmatrix}. \tag{56}$$

This phase matrix links the Stokes vectors of the incident and scattered beams, specified relative to their respective meridional planes. To compute the Stokes vector of the scattered beam with respect to its meridional plane, one must calculate the Stokes vector of the incident beam with respect to the scattering plane, multiply it by the scattering matrix (to obtain the Stokes vector of the scattered beam with respect to the scattering plane), and then compute the Stokes vector of the scattered beam with respect to its meridional plane. Such a procedure involves two rotations of the reference plane: $\Phi = -\phi$; $\Psi = \pi - \phi$ and $\Phi = \pi + \phi$; $\Psi = \phi$. The scattering angle θ and the angles Φ and Ψ are expressed via the polar and the azimuth incident (ϑ, φ) and scattering angles (ϑ', φ').[5,15,99]

Every Stokes vector and Mueller matrix are associated with a specific reference plane and coordinates. The first term on the right-hand side of VRTE [Eq. (53)] describes the change in the specific intensity vector over the distance ds caused by extinction and diattenuation (dichroism); the second term describes the contribution of light illuminating a small volume element centered at $\bar{\mathbf{r}}$ from all incident directions and scattered into the chosen direction.

For real systems, the form of VRTE is rather complex and often intractable. Therefore, many analytical and numerical techniques have been developed to solve VRTE. As the normalized phase matrix [Eq. (55)] depends on the difference of the azimuthal angles of the scattering and incident directions rather than on their specific values, an efficient analytical treatment of the azimuthal dependence of the multiple scattered light, using a Fourier decomposition of the VRTE, is possible.[100] The following techniques and their combinations can be used to solve VRTE: transfer matrix method, the singular eigenfunction method, the perturbation method, the small-angle approximation, the adding-doubling method, the matrix operator method, the invariant embedding method, and the Monte Carlo (MC) method.[9,13,16,18,20–22,52–54,56,59,64,65,68–70,73,93,97–101,140,144–153]

4.4.2 *Polarization-sensitive Monte Carlo modeling*

A number of powerful MC codes for the modeling of polarized light propagation through a scattering layer are available in the literature (see, for example, Refs. 2, 5, 13, 15, 59, 64, 68, 70, 73, 85, 89, 93, 94, 146, 147, 150, 151, and 153–160). The polarization-sensitive MC modeling has the following major advantages: the possibility to employ any scattering matrix; one is not able to use strongly forward directed phase functions or experimental single-scattering matrices; the calculation of polarization parameters takes only a twofold increase in computation time over that needed for the evaluation of intensity; and the possibility to model media with complex geometry. The main disadvantage of the MC technique is a trade-off between the accuracy and the computation time. To provide a twofold increase of the accuracy, one needs a fourfold increase in the computation time.

To illustrate a MC simulation technique, we will briefly discuss the algorithm described in Ref. 147 and applied to model the angular dependencies of the scattering matrix elements. Let a flux of photons within an infinitely narrow beam be incident exactly upon the center of the spherical volume with the randomly distributed scattering particles inside. When an incident photon enters a scattering volume, it is allowed to travel a mean free path (MFP) l, which depends on the particle concentration ρ and extinction cross-section $\sigma_{\text{ext}} = (\sigma_{\text{abs}} + \sigma_{\text{sca}})$ (see Sec. 4.1.3). The MFP l is a random quantity that takes any positive values with the probability density $p(l)$,

$$p(l) = \rho\sigma_{\text{ext}} e^{-\rho\sigma_{\text{ext}} l}. \tag{57}$$

The particular realization of the MFP l is dictated by the value of a random number ξ that is uniformly distributed over the interval [0, 1],

$$\int_0^l p(l)dl = \xi. \tag{58}$$

Substituting Eq. (57) into Eq. (58) yields the value l of the certain realization in the form

$$l = -\frac{1}{\rho\sigma_{\text{ext}}} \ln \xi. \tag{59}$$

If the MFP is larger than the diameter of the scattering object, then this photon is transmitted without any scattering (ballistic photons). For the smaller MFPs, when the photon remains within the scattering volume, the possible events of photon–particle interaction (scattering or absorption) are randomly selected.

For the spherical system of coordinates, the density of the probability of photon scattering along the direction specified by the scattering angle θ between the directions of the incident and scattered photons and by the angle ϕ between the previous and new scattering planes is given by[147]

$$p(\theta, \varphi) = \frac{I_s(\theta, \varphi) \sin\theta}{\int_0^{2\pi} \int_0^{\pi} I_s(\theta, \varphi) \sin\theta d\theta d\varphi}, \tag{60}$$

where $I_s(\theta, \phi)$ is the intensity of the light scattered in the direction (θ, ϕ) with respect to the previous direction of the photon, defined by angles ϑ and φ [see Eqs. (53) and (54)]. For spherical particles, this intensity is given by the Mie equations [see Eqs. (37)–(39)] with allowance for the state of polarization of each photon. An integral $I_s(\theta, \phi)$ over all scattering directions determines the scattering cross-section,

$$\sigma_{\text{sca}} = \int_0^{2\pi} \int_0^{\pi} I_s(\theta, \varphi) \sin\theta d\theta d\varphi. \tag{61}$$

The density of the probability of photon scattering along the specified direction, $p(\theta, \phi)$, is defined by the Mueller matrix of the scattering particle $\mathbf{M}(\theta, \phi)$ (a single-scattering matrix) and the Stokes vector $\mathbf{S}$ associated with the photon [Eqs. (2) and (9)]. The single-scattering Mueller matrix $M(\theta, \phi)$ links the Stokes vectors of the incident $[\mathbf{S}_i(0,0)]$ and scattered $[\mathbf{S}_s(\theta, \phi)]$ light. For the spherical particle tissue model, the elements of this matrix may be factorized,

$$M(\theta, \varphi) = M(\theta)R(\varphi). \tag{62}$$

For spherical particles, the single-scattering matrix $M(\theta)$ is described by Eqs. (47) and (50). The elements of this matrix are given by the Mie equations,[96,141] which are functions of the scattering angle θ and diffraction parameter $x = 2\pi a/\lambda$, where a is the radius of the spherical particle and λ is the wavelength in the medium. The matrix $R(\phi)$ describes the transformation of the Stokes vector under rotation of the plane of scattering through the angle ϕ, which is defined by Eq. (56). Thus, the intensity of the light scattered by spherical particles can be presented by the following algorithm:

$$I_s(\theta, \varphi) = [M_{11}(\theta)I_i + (Q_i \cos 2\varphi + U_i \sin 2\varphi)M_{12}(\theta)], \tag{63}$$

where Q_i and U_i are components of the Stokes vector of the incident light [see Eq. (2)]. As it follows from this equation, the probability $p(\theta, \phi)$ [Eq. (60)], unlike the scattering matrix [Eq. (62)], cannot be factorized; it appears to be parametrized by the Stokes vector associated with the scattered photon.

The method of generating pairs of random numbers with the probability density $p(\theta, \phi)$ can be used in that case.[147] In the 3-D space, the function $p(\theta, \phi)$ specifies some surface. The values (θ, ϕ) corresponding to the distribution $p(\theta, \phi)$ are chosen using the following steps: (1) a random direction (θ_ξ, ϕ_ξ) with a uniform spatial distribution is selected, and the values of the random quantities θ_ξ and ϕ_ξ distributed over the intervals $[0, \pi]$ and $[0, 2\pi]$, respectively, are found from the equations

$$\cos\theta_\xi = 2\xi - 1, \varphi_\xi = 2\pi\xi, \tag{64}$$

where ξ is a random number uniformly distributed over the interval [0,1]; (2) the surface specified by the function $p(\theta, \phi)$ is surrounded by a sphere of radius R, equal to the maximum of the function $p(\theta, \phi)$, and a random quantity $r_\xi = \xi R$ is generated; (3) the direction (θ_ξ, ϕ_ξ) is accepted as the random direction of the photon scattering at this stage, providing the condition $r_\xi \leq p(\theta_\xi, \phi_\xi)$ is satisfied. If not, steps 1 and 2 are repeated again.

The migration of the photon can be described by a sequence of transformations for the related coordinate system. Each scattering event provides a variation of the Stokes vector associated with the photon. The new Stokes vector $\mathbf{S}_{n+1}$ is a product of the preceding Stokes vector, transformed to the new scattering plane, and the Mueller matrix $\mathbf{M}_k(\theta)$ of the scattering particle,

$$\mathbf{S}_{n+1} = M_k(\theta) R_n(\varphi) \mathbf{S}_n, \tag{65}$$

where the matrix $R_n(\phi)$ [see Eq. (56)] describes the rotation of the Stokes vector around the axis specifying the direction of propagation of the photon before the interaction.

For the chosen scattering direction, the Stokes vector is calculated using Eqs. (9), (47), (49), (65), and expressions for elements of the single-scattering Mueller matrix for a homogeneous sphere made of an optically inactive material.[15,96,141] The value thus obtained is renormalized to get the Stokes vector associated only with the information on the state of polarization of the scattered photon. The intensity is determined from the number of detected photons within the chosen direction on the detector aperture.

The described procedure is repeated as long as the photon appears to be outside the scattering volume. The spatial distribution of the scattered radiation can be obtained with regard to the polarization state by analyzing the above data for a sufficiently great number of photons.

To illustrate the MC simulation technique, the described algorithm[147] was used to model the angular dependencies of the LSM elements for polarized light propagating in a medium with parameters close to that of a multiply scattering tissue. The results of these calculations, presented in Figs. 15 and 16, demonstrate that the polarization properties of tissues could be dramatically transformed for the multiple-scattering conditions. The simulation was performed for the ensembles of spherical particles with a relative index of refraction, $m = 1.2$, uniformly distributed within a spherical volume (spheroid) at volume fraction $f = 0.01$. A narrow illuminating beam is incident exactly upon the center of the spheroid at the zero angle direction and the scattered radiation is detected at different scattering angles in the far zone by a detector with the angular aperture of 1 deg in the scattering plane and 5 deg in the orthogonal plane (see Fig. 1).

The angular distributions of the total scattering intensity for ensembles of particles with small radius, $a = 50$ nm, and large radius, $a = 300$ nm, are presented in Figs. 15(a) and 16(a), respectively. The multiplicity of scattering increases with increasing dimensions of the tissue-mimicking spheroids filled up by the particles. As follows from modeling, for small particles distributed in the small spheroid of 1-mm diameter due to the predominant contribution of a single scattering showing angular isotropy [Fig. 15(a), spheroid 1], the Rayleigh scattering

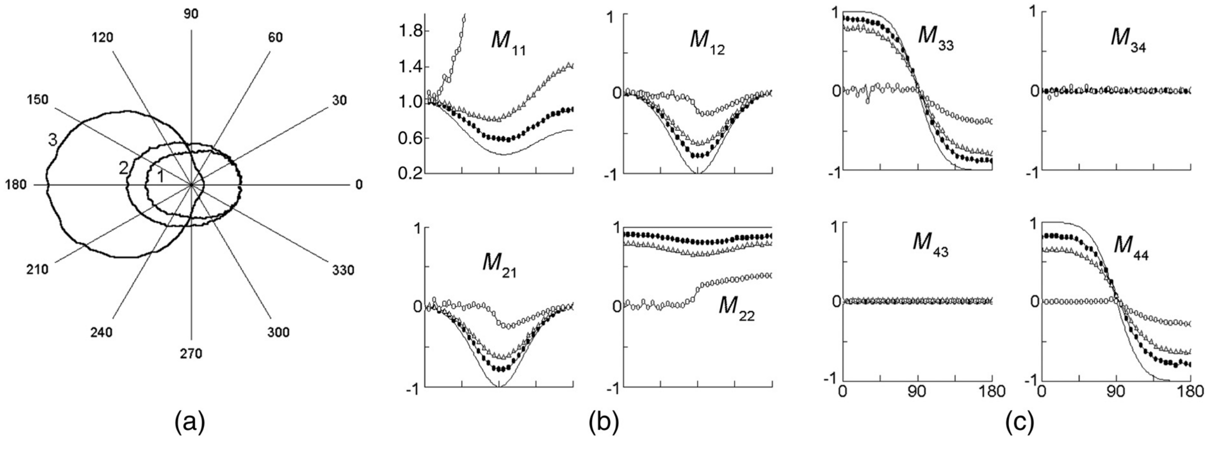

Fig. 15 (a) The MC simulation: LSM elements for ensembles of small dielectric particles filling up spheroids of different diameters:[147] particle radius $a = 50$ nm, relative index of refraction $m = 1.2$, particle volume fraction $f = 0.01$, light wavelength $\lambda = 633$ nm; the angular distributions of the scattered light intensity $[M_{11}(\theta)]$ from spheroid of diameter 1 mm (1), 2 mm (2), and 20 mm (3); (b) a group of LSM elements from the first quadrant of Mueller matrix [Eq. (33)]: $M_{11}, M_{12}, M_{21}, M_{22}$; M_{12}– refers to a degree of linear polarization of the scattered light; M_{22} displays the ratio of depolarized light to the total scattered light (marker of particle nonsphericity); (c) a group of LSM elements from the fourth quadrant of Mueller matrix [Eq. (33)]: $M_{33}, M_{34}, M_{43}, M_{44}$; difference between M_{33} and M_{44} is a good measure of particle nonsphericity; (—) presents calculations for single scattering approximation; remaining curves present calculations for multiple scattering for spheroids of diameters 1 mm (-•-), 2 mm (-Δ-), and 20 mm (-○-).

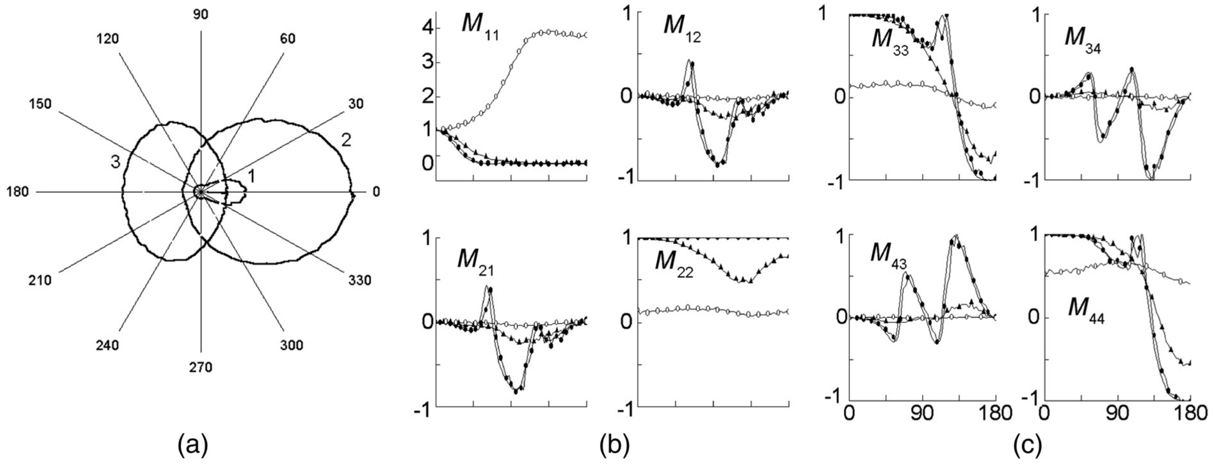

Fig. 16 (a) The MC simulation: LSM elements for ensembles of big dielectric particles filling up spheroids of different diameters:[147] particle radius $a = 300$ nm, relative index of refraction $m = 1.2$, particle volume fraction $f = 0.01$, light wavelength $\lambda = 633$ nm; the angular distributions of the scattered light intensity $[M_{11}(\theta)]$ from spheroid of diameter 0.002 mm (1), 0.2 mm (2), and 2 mm (3); (b) a group of LSM elements from the first quadrant of Mueller matrix [Eq. (33)]: $M_{11}, M_{12}, M_{21}, M_{22}$; M_{12} refers to a degree of linear polarization of the scattered light; M_{22} displays the ratio of depolarized light to the total scattered light (marker of particle nonsphericity); (c) a group of LSM elements from the fourth quadrant of Mueller matrix [Eq. (33)]: $M_{33}, M_{34}, M_{43}, M_{44}$; difference between M_{33} and M_{44} is a good measure of particle nonsphericity; M_{34} displays the transformation of 45 deg obliquely polarized incident light to circularly polarized scattered light; (—) presents calculations for single-scattering approximation; remaining curves present calculations for multiple scattering for spheroids of diameters 0.002 mm (-●-), 0.2 mm (-Δ-), and 2 mm (-○-).

approximation could be applicable for such particles. As the spheroid increases in diameter, the contribution of the multiplicity of scattering grows as well and the shape of the intensity angular distribution is transformed; beginning from a certain value of the spheroid diameter, most of the incident light is scattered in the backward direction.

Spheroids composed of particles with a size comparable with the wavelength [Fig. 16(a)] also show an increase in the contribution of multiple scattering with an increase of spheroid diameter. However, the particle system transforms from the forward to the backward directed scattering mode at a rather small thickness, 2 mm in diameter.

As can be seen for both small and large particles, the intensity of unpolarized scattered light at the high scattering multiplicity mode weakly depends on the scattering angle and carries almost no information about the size of the scattering particles.

The angular dependences of LSM elements at a multiple-scattering mode differ substantially from that for the LSM of a single-scattering system (solid lines). It is seen from Figs. 15(b), 15(c), 16(b), and 16(c) that the multiple scattering flattens the angular dependences of the LSM elements. All elements of the LSM are normalized to the M_{11} element (total scattering intensity) along the given direction, and the element M_{11} is presented in the plot as normalized to unity in the forward direction; its actual intensity distributions are presented in Figs. 15(a) and 16(a).

For small particles (Fig. 15), the contribution of multiple scattering is associated with a gradual decrease in magnitude of all the elements except M_{11}; i.e., the form of the LSM approaches that of the ideal depolarizer. In particular, the magnitudes of M_{12} and M_{21} decrease in nearly the same way; M_{33} and M_{44} also decrease in magnitude. As M_{44} decreases faster, the difference between M_{33} and M_{44} can be detected for multiple scattering media, even composed from only spherical particles. M_{11}, which refers to the total scattering intensity, shows a significant scattered light redistribution from the mode of isotropic scattering characteristic to single scattering to more intensive scattering mostly in the backward direction as the multiplicity of scattering goes up. The polarization ability of the system originated by Rayleigh (single dipole) scattering (see Fig. 15) and expressed in terms of the element M_{12}, which refers to a degree of linear polarization of the scattered light, goes down as scattering multiplicity increases. The 100%-polarization efficiency at the scattering angle $\theta = 90$ deg for the single-scattering mode is reduced significantly, to ~20%, at multiple scattering.

Thus, the manifestation of multiple scattering in a monodispersive system of small spherical particles, which leads to the nonzero difference of $|M_{33} - M_{44}|$ and $|1 - M_{22}|$, is similar to the influence of particle nonsphericity under conditions of single scattering. The effects of multiple scattering are apparent as the broken symmetry relationship between LSM elements $M_{12}(\theta) \neq M_{21}(\theta), M_{33}(\theta) \neq M_{44}(\theta)$, and a significant reduction of linear polarization of the light scattered at angles close to $\pi/2$.[161]

For the large particle systems, transfer from the single- to multiple-scattering mode changes angular dependences of the elements M_{11} and M_{12} more dramatically than for small particles (see Fig. 16). As the multiplicity of scattering increases, a strong forward scattering transfers to a strong backward scattering with the shape more or less similar to the scattering by small particles; however, the polarization ability at $\theta = 90$ deg decreased from ~80% to a few percentages only. The multiple scattering also decreases the magnitudes and smooths out the angular dependences of LSM elements, showing the following specific features: M_{22} reaches its minimum not at 90 deg, but rather at larger angles; the fine structures of the angular dependences for all elements are smeared, and M_{44}

tends to 0.5 rather than to zero. Therefore, the scattered radiation holds the preferential circular polarization at higher scattering multiplicities. This result is consistent with theoretical and experimental data on the survival of different types of polarization under conditions of multiple scattering for particles or tissue structures of different sizes.[11,15,52,54]

The depolarization will increase with the growth of scattering multiplicity. For moderate optical thickness (spheroid of 0.2 mm, $f = 0.01$), the depolarizing ability is strongly different for different directions. The scattered light may be almost completely polarized in the region of small scattering angles and completely depolarized at large angles ($\theta = 120$ deg) and be partly polarized in the backward direction. The angular range of the strongest depolarization corresponds to the angle at which the element M_{22} acquires minimum values [see Fig. 16(b)].

These MC simulations allow one to estimate the limits of applicability of the single-scattering approximation when interpreting the results of experimental studies on tissues and cell structure, such as cancer cell spheroids.[162–164] These simulations also allow one to analyze limitations on the application of the measured LSM for reconstruction of scatterer nonsphericity at multiple scattering. The appropriate criteria to distinguish the effects of multiple scattering and particle nonsphericity have to be developed.

The Mueller matrix for the backscattering geometry was obtained by solving a radiative transfer equation with appropriate boundary conditions.[15] Analysis of this matrix structure showed that its form coincides with the single-scattering matrix for optically active spherical particles. Thus, different healthy or diseased tissues should display different responses to the probing with linearly and circularly polarized light. This phenomenon can be employed for optical medical tomography and tissue optical properties quantification.

The comparison of MC simulation accounting for multiple scattering with the analytical double-scattering model had indicated no essential alterations in the backscattering polarization patterns.[148] This indicates that the main contribution comes from near-double-scattering trajectories in which light undertakes two wide-angle scattering events and many near-forward scatterings among multiple-scattering trajectories.

To account for particle spatial correlation, one can include the interference of scattered fields into calculations of the single-scattering Mueller matrix and integral cross-sections for a particle.[5,15] If the size of a region of the local particle correlation is substantially smaller than the mean free photon path length,[165,166] it is possible at the first step of MC simulation to consider interference effects in the framework of the single-scattering properties and then to use modified properties in the multiple-scattering simulations.

As the TMFP, l_{tr} [see Eq. (42)], of a photon traveling in tissues characterizes the distance within which the direction of light propagation and, consequently, the polarization plane of linearly polarized light become totally random after many sequential scattering events, thus, the depolarization length should be close to the TMFP.[2,5,8,11,15,52,54]

From the MC modeling presented in Fig. 17, it follows that at backscattering starting from the multiplicity of scattering more than 10 times, circularly polarized photons keep their polarization state considerably better than the linearly polarized photons at light propagation in tissue-like media.[13] For linear polarization, the degree of polarization (DOP) on the level of $P_{\mathrm{L}} \leq 0.3$ comes mainly from photons that have been scattered less than 10 times as for circular polarization, the DOP with $P_{\mathrm{C}} \leq 0.3$ comes mainly from photons that have been scattered 10 to 60 times with a maximum of $P_{\mathrm{C}} \cong 0.55$ at 18 to 20 collisions. This result supports data presented in Fig. 16[147] and Ref. 54, because calculations were done for size factor $ka = 6.5$, which corresponds to the Mie scattering mode ($ka \gg 1.3$). The phenomenon is also known as the circular polarization memory of light,[74,75] which is of fundamental importance for polarized light–tissue interaction, allowing one to provide unique tissue diagnostics.

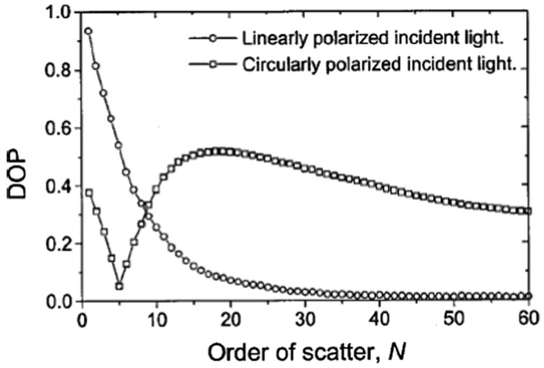

Fig. 17 MC simulation for DOP of backscattered photons as a function of the number of scatters *N* for linearly and circularly polarized incident light;[13] the wavelength in the free space, $\lambda_0 = 450$ nm; a photodetector has a narrow receiving angle; the refractive indices of the scattering spheres and surrounding medium are 1.57 and 1.33, respectively; the radius of spheres is $a = 350$ nm, and size factor $ka = 6.5$; $\mu_{\mathrm{s}} = 90\ \mathrm{cm}^{-1}$, $\mu_{\mathrm{a}} = 1\ \mathrm{cm}^{-1}$, and $g = 0.9$.

For soft tissues and blood, the experimental data of Ref. 50 demonstrate that the depolarization length l_p of linearly polarized light (defined as the length for which $I_{||}/I_{\perp}$ decreases down to 2 from the initial magnitude of $I_{||}/I_{\perp} = 300$) displays its dependence on l_{tr} (i.e., g). l_{p} differs considerably for the brain white matter and cerebral cortex: 0.23 and 1.3 mm for $\lambda = 633$ nm, respectively. Human skin bloodless dermis has $l_{\mathrm{p}} \cong 0.46$ mm ($\lambda = 633$ nm). l_{p} is $\cong 0.54$ mm for a normal aorta, $\cong 0.39$ mm for calcified tissue, and $\cong 0.33$ mm for necrotic ulcer ($\lambda = 476$ to 514 nm). Whole blood with a low hematocrit is characterized by a considerable depolarization length, $l_p \cong 4$ mm at $\lambda = 633$ nm. This is indicative of the dependence on the scattering anisotropy factor g, whose value for blood is of 0.982 to 0.999.[5,167]

Figure 18 presents the experimental data for decay of the degree of linear polarization $P_L = I_{||} - I_{\perp}/I_{||} + I_{\perp}$ for various tissues and blood with an increase of tissue layer thickness, expressed in terms of light transmittance $I_{\mathrm{out}}/I_{\mathrm{in}} \equiv T$ through the layer.[11]

For many tissues, due to multiple scattering, it is impossible to detect pure ballistic photons (photons that do not experience scattering), but forward scattered photons retain their initial polarization and can be used for imaging purposes.[2,5,6,9,10,15,18,94] It was experimentally demonstrated by Steve Jacques that laser radiation retains linear polarization on the level of $P_{\mathrm{L}} \leq 0.1$ within $2.5 l_{\mathrm{tr}}$. Specifically, for skin irradiated in the NIR, $\mu_a \cong 0.4\ \mathrm{cm}^{-1}$, $\mu_s' \cong 20\ \mathrm{cm}^{-1}$, and $l_{\mathrm{tr}} \cong 0.48$ mm [Eq. (42)]. Consequently, light propagating in skin can retain linear polarization within the length of ∼1.2 mm. Such an optical path corresponds to a delay time of 5.3 ps for light propagating in a tissue and allows for polarization imaging of macro-inhomogeneities with a spatial resolution equivalent to that of much more sophisticated time-resolved techniques. In addition, polarization-contrast imaging

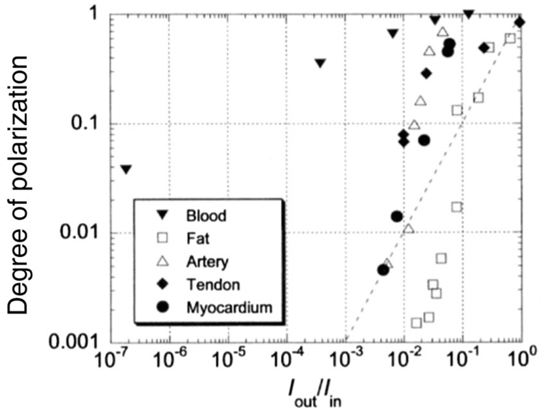

Fig. 18 Degree of linear polarization P_L for tissues and blood as a function of the sample optical transmittance, $I_{out}/I_{in} \equiv T$, at the wavelength of 633 nm. For a particular tissue type, transmittance is less as thickness of the sample is bigger. Each point is an average of three measurements.[11]

makes it possible to eliminate tissue specular reflection and bulk absorption, thus allowing for imaging of superficial microvessels and subsurface textural changes and erasing absorbers (melanin) from an image.[8,10,19,51,60]

5 Polarization Measurements

5.1 *Polarized Reflectance Spectroscopy*

The morphological and functional state of tissue may be effectively monitored by the spectral analysis of the polarization properties of the scattered light.[7,15,24,64,77,168–174] The probing of a tissue by a linearly polarized white light beam and measuring the spectral response of co- and cross-polarized components of the backscattered light allow one not only to quantify chromophore content, but also to estimate its in-depth distribution. It is important to note that tissue absorbers such as melanin in skin epidermis and hemoglobin in dermis increase the degree of the residual polarization of the backscattered light in the spectral ranges corresponding to absorbing bands of the dominate chromophores. This happens due to shortening of photon migration trajectories at absorption, because the length of trajectories is proportional to the multiplicity of scattering, i.e., determines depolarization ability. Since tissue chromophores are placed at different depths, their localization may be estimated owing to characteristic absorbing bands on the differential polarization spectra.[15,168]

The wavelength dependence of the intensity of the light elastically scattered by the tissue structure appears sensitive to changes in tissue morphology that are typical of precancerous lesions.[7,24,169,171] It was found that specific features of malignant cells, such as increased nuclear size and nuclear/cytoplasmic ratio, are markedly manifested in the elastic light scattering spectra of the probed tissue. The oscillatory component of the spectra is due to a single scattering from surface epithelial cell nuclei and is described by Mie theory [see Eqs. (27)–(39), Figs. 10 and 13]. The density and size distributions of these nuclei could be reconstructed from the spectra. However, this superficial epithelial tissue probing method suffers from a diffuse background and hemoglobin absorption. By using a polarization discrimination technique for detection of linear co- and cross-polarized components of the backreflecting intensity, these drawbacks could be overcome.[7,172] Polarized reflectance spectroscopy (PRS) will potentially provide a quantitative estimate not only of the size distributions of cell nuclei, but also of the relative refractive index of the nucleus. The potentialities of PRS have been demonstrated in a series of experimental works with tissue phantoms and *in vivo* epithelial tissues.[7,15,24,71,169–174] A fiber optic probe[175] with a high spatial resolution is prospective for clinical applications of PRS for early skin cancer diagnostics.

5.2 *Fluorescence Polarization Spectroscopy*

Fluorescence polarization spectroscopy is used to estimate parameters of the fluorophore environment.[176] Thus, it has a potential for biomedical diagnostics, in particular, in discriminating between normal and malignant tissues.[177–183] At polarized light excitation, the emission from a fluorophore in a nonscattering medium becomes depolarized because of the random orientation of the fluorophore molecules and the angular displacement between the absorption and emission dipoles of the molecules.[176] These intrinsic molecular processes are sensitive to the local environment of the fluorophore.

In tissues, multiple scattering also leads to depolarization of the propagating polarized light, both of excitation and emission.[177–183] Fluorescence polarization measurements should be sensitive to tissue structural or functional changes, which are caused by tissue malignancy at the molecular level (the sensitivity to the environmental molecules) or at the macrostructural level (the sensitivity to tissue scattering properties). In addition to polarized fluorescence spectra, fluorescence polarization anisotropy (r), which is a dimensionless quantity independent of the total fluorescence intensity, is measured,[176]

$$r = \frac{I_{\parallel} - I_{\perp}}{I_{\parallel} + 2I_{\perp}}. \tag{66}$$

Collagen, elastin, coenzymes (NADH/NADPH), and flavins contribute to polarized fluorescence spectra with orthogonal linear polarizations with excitation at 340 and 460 nm of human breast tissue samples.[177,178] The contribution of NADH dominates with excitation at 340 nm as different forms of flavins dominate with excitation at 460 nm. A blueshift in the polarized fluorescence spectra maximum was found in the malignant, as compared to the normal tissue. A similar shift of 5 to 10 nm was also observed for 460-nm excited fluorescence. This shift is associated with the accumulation of positively charged ions in the intracellular environment of the malignant cells. A spectral shift of the maximum between the parallel and cross-polarized fluorescence spectra observed for rather thick tissue samples (≈2 mm) was associated with the elastic scattering and the absorption properties of the tissue.

The fluorescence anisotropy factor measured for normal and malignant human breast samples at 440 nm emission and 340 nm excitation was higher for malignant tissues as compared to normal for very thin tissue sections, $d \leq 30$ μm.[178] By contrast, in thicker sections, the malignant tissue shows smaller fluorescence anisotropy than the normal tissues. The dependence on tissue thickness is associated with the manifestation of various mechanisms of fluorescence depolarization. Energy transfer and/or rotational diffusion of the fluorophores dominate in thin tissue sections, and these processes are faster in normal tissues than in malignant ones. In thicker sections, elastic light scattering dominates with more contribution to depolarization during light transport within the malignant tissues.

This suggests fluorescence anisotropy measurement to be a useful parameter for discriminating malignant sites from normal ones. It could be used especially for epithelial cancer diagnostics where thin superficial tissue layers are typically examined.[178] Fluorescence-polarization measurements with exogenous fluorophores used for the demarcation of melanoma and other types of skin cancer are presented in Refs. 179–183.

5.3 *Mueller Matrix Meter*

In general, four independent polarization state measurements are necessary to obtain one element of Mueller matrix or LSM.[15,144] A significant drawback of the technique at a CW mode use is the possible relative errors associated with small LSM elements obtained as differences of big intensity signals. These errors can be effectively reduced by modulating the polarization state in the incident and/or the scattered fields. A laser Mueller matrix meter based on polarization modulation of the incident and scattered light by mechanically rotating phase plates has been described.[5,6,15,184–186] The principle of operation is described by the following matrix equation:

$$\mathbf{S} = AF'MFP\mathbf{S_0}, \tag{67}$$

where $\mathbf{S}$ and $\mathbf{S_0}$ are the Stokes vectors of recorded and source radiations, respectively; A, P and F', F are the Mueller matrices for the linear analyzer and polarizer and the phase plates [typically quarter-wave plates (QWPs)] in front of the detector and object, respectively, as shown in Fig. 19.

As the phase plates (QWPs) are rotated, the intensity recorded by a photodetector would depend on time. By multiplying the matrices in Eq. (67) and performing the appropriate trigonometric transformations, one can find that the output intensity would be represented as a Fourier series, namely[5,15,184–186]

$$I = a_0 + \sum_{k=1}^{K} (a_{2\,k} \cos 2\,k\phi + b_{2\,k} \sin 2\,k\phi), \tag{68}$$

where φ is the angle of orientation of the fast axis of the first phase plate.

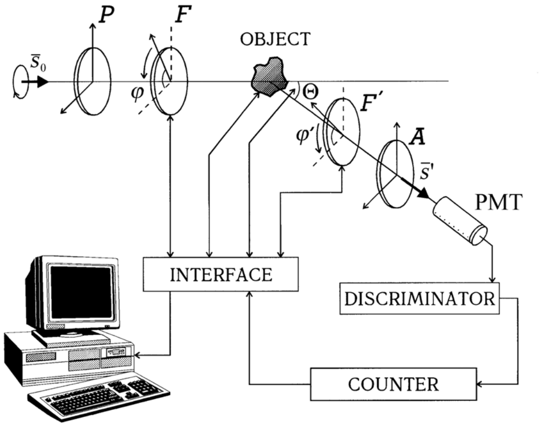

Fig. 19 Schematics of a Mueller matrix meter with the rotating phase plates (QWPs): $\bar{S}_0$ is the laser light source with a high quality of circular polarization; P is the linear polarizer; the next are the first rotating phase plate F, object under study, and the second rotating phase plate F'; A is the linear analyzer; and PMT is the photomultiplier.[5,144]

The coefficients of this series are defined by the values of the matrix M elements of the sample under study and their measurement ensures a system of linear equations to determine the matrix M. The number of equations are dependent on the ratio between rotation rates of the phase plates. The rotation rate ratio is 1:5, i.e., $\varphi' = 5\varphi$ allows one to get an optimally stipulated system of linear equations ($K = 12$) to find the full matrix M.[5,15,184–186] More sophisticated and fast electro-optic modulation of the polarization state is also used.[187–190]

Experimental studies of polarization properties of scattering tissues and cells are presented in multiple original and review literature (see, for example, Refs. 2, 5–11, 14–22, 24, 28, 29, 37–42, 46, 48–51, 60, 65, 86, 87, 90–92, 94, 97, 105, 191–195). To classify tissue or cell abnormalities or functioning by analyzing their LSM angular dependences, one is able to account for the distinctions between elements $M_{22}(\theta)$ and $M_{11}(\theta)$ that would serve as a measure for scattering particles to be nonspherical. Studies of different types of pollen and marine organisms in diluted suspensions showed a high sensitivity to modification of their form. However, for dense cell suspensions or tissues, a similar distinction between $M_{22}(\theta)$ and $M_{11}(\theta)$ may be caused by multiple scattering.

The angular behavior of $M_{34}(\theta)$ is most specific for various biostructures because of its sensitivity to small morphological alterations, such as surface roughness of spherical particles. It was used for determining the diameter of rod-shaped bacteria (*Escherichia coli*), which is difficult to measure using other techniques.[40]

The LSM angular measurements were used to examine RBC and white blood cells, in particular to quantify the index of refraction[191] and to distinguish between disc-like and spherical-shaped RBC,[192] as well as between two types of granulocytes.[193]

The measurements of angular dependences of the informative LSM elements for the human eye lenses carried out using the laser Mueller matrix meter (Fig. 19) demonstrate substantial modification of these dependencies for normal and turbid (cataractous) lenses[6] (Fig. 20). If for the aged but clear lens a set of LSM elements $M_{12}(\theta)$, $M_{34}(\theta)$, $M_{33}(\theta)$, and $M_{44}(\theta)$ differs only slightly from that of a system of monodisperse spherical particles, then for lens with cataract, the discrepancy is huge. Such studies are important for understanding in what way the alteration of spatial protein organization would lead to turbidity.

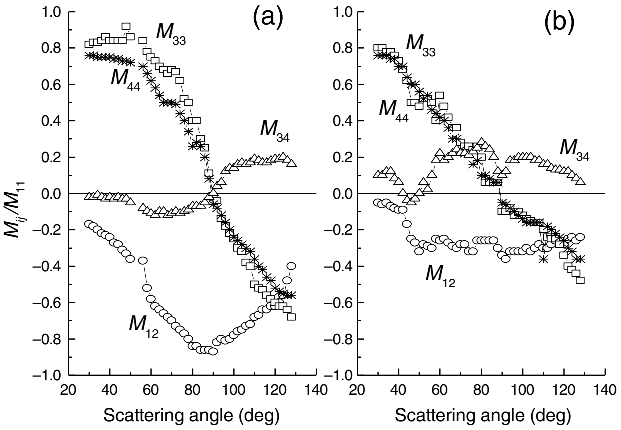

Fig. 20 Experimental angular dependencies for the LSM elements of normal human lens (a) (age 56 years, 5 h after death) and (b) lens with cataract (age 88 years, 5 h after death). Measurements were performed at a wavelength of 633 nm.[6]

As follows from experimental data, a transparent lens is featured by a system of small-diameter particles close to a monodisperse one, and a turbid lens contains a considerable fraction of bigger particles appearing due to the formation of high-molecular proteins. The high sensitivity of the LSM to variations in tissue structure makes it possible to use its measurement for early cataract diagnostics.

5.4 *Polar Decomposition of Mueller Matrix*

As we see, the interpretation of the measured polarization properties for clear tissues, thin tissue sections, and dilute cell suspensions is more or less straightforward and can be done in terms of characteristic LSM elements. However, for thick turbid tissues where polarization alteration can be due to multiple scattering effects, Mueller matrix measurements should be processed by its polar decomposition to quantify diattenuation, retardance, and depolarization separately.[18–22,105,194–196] Following a paper by Gupta et al.,[105] it is possible to underline some typical overlapping polarization effects that can be detected in multiple scattering tissues. A rotation of the plane of polarization of incident linearly polarized light (retardance) can be caused both by the presence of chiral molecules such as glucose or due to the diattenuation and retardance caused by single backscattering. In their turn, diattenuation and retardance associated with the presence of oriented collagen or myosin structures in tissues can also contribute to the depolarization as multiple scattering does.

To extract tissue structural information in the presence of all these factors affecting the depolarization, retardance, and diattenuation is a difficult problem. In addition to the above-discussed scattering angular-resolved Mueller matrix measurements, its spatially and spectrally resolved studies can provide valuable information for successful deconvolution of some of the different contributions.[105,145]

Polar decomposition of the Mueller matrix[18–22,105,194–196] is an efficient way to quantify tissue polarization properties from the measured Mueller matrix, which is presented as a combination of a diattenuator M_{D}, a retarder M_{R}, and a depolarizer M_{Δ} matrices. The steps involved in the polar decomposition of the Mueller matrix are shown as a flowchart in Fig. 21.[105,196]

Using the polar decomposition of the experimentally measured Mueller matrix, the depolarization index Δ at each wavelength can be computed [see Eq. (14)].

5.5 *Linear Polarization Measurements: 3 × 3 Partial Mueller Matrix*

As we see, the polarization properties of any tissue sample can be fully presented by a (4×4) Mueller matrix. This requires both linearly and circularly polarized light independent measurements (no less than 16) to be provided. For many medical diagnostic applications, more robust techniques are preferable; thus, the approach introduced by Gupta et al.,[110,197,198] which is based exclusively on linear polarization measurements, has a good perspective. These authors suggest the use of a (3×3) partial Mueller matrix, containing only the first three rows and columns of the conventional (4×4) matrix. In that case, nine independent linear polarization measurements are enough to get all elements of the (3×3) matrix. Using the various symmetry constraints on Mueller matrix elements, the authors proved that for nondepolarizing media, the 4×4 Mueller matrix can be fully reconstructed from the measured (3×3) matrix.

The decomposition procedure of the experimentally obtained (3×3) Mueller matrix M as the product of diattenuation (M_{D}), retardation (M_{R}), and depolarization (M_{Δ}) matrices is described in detail.[110,197,198] The measured Mueller matrix can be expressed as[198]

$$M = M_{\Delta} M_{\mathrm{R}} M_{\mathrm{D}}, \tag{69}$$

where the first row is used to construct the 3×3 diattenuation matrix (M_{D}). Then by multiplying the inverse of the diattenuation matrix M_{D}^{-1} and M, MM_{D}^{-1}, diattenuation is eliminated from M. The remaining matrix (M') consists of only retardance and depolarization,

$$M' = MM_D^{-1} = M_{\Delta} M_{\mathrm{R}}. \tag{70}$$

For a nondepolarizing sample, the depolarization matrix is the identity matrix, and M' can be used to calculate the linear retardance δ and circular retardance ψ (optical rotation).

However, for a depolarizing sample, decoupling of the depolarization matrix is needed.[197] In tissues, due to the randomization of the orientation of the polarization vector at multiple scattering, the depolarization of linearly polarized light is independent of the orientation angle of the incident linear polarization vector. Thus, polar decomposition of a (3×3) Mueller matrix can be provided and the linear retardance (δ), the circular retardance (ψ), the linear depolarization coefficient (Δ), and the linear diattenuation (D_{L}) can be quantified.[197]

The advantages of the linear polarization measurement technique follow from the simplicity of the measurement procedure and the possibility to provide measurements in a wider spectral range due to the absence of the QWPs required for circular polarization measurements. The measurement of polarization parameters (linear retardance, diattenuation, and depolarization) of normal and malignant tissue from human oral cavity and breast over the spectral range from 390 to 550 nm was reported.[198] Also, multispectral (3×3) Mueller matrix imaging was performed over a spectral range from 470 to 632 nm for 4-μm unstained gastric tissue sections.[199] In this study, the combination of linear depolarization and linear retardance yields the highest accuracy in sample classification.

This (3×3) Mueller matrix technology shows the feasibility of implementing polarimetric imaging in an endoscopic investigation in order to reveal valuable diagnostic information.[200]

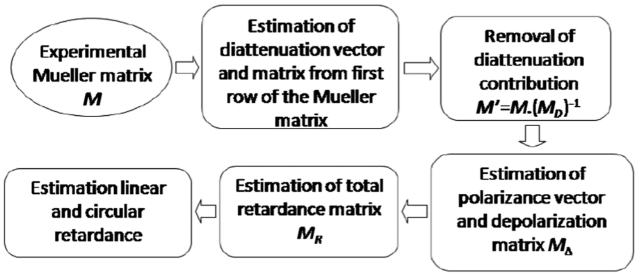

Fig. 21 Flowchart for polar decomposition of an experimentally obtained Mueller matrix.[105]

5.6 *Circular Light Probing and Optical Activity*

Many tissues and cell suspensions demonstrate the effects of optical activity that are manifested in circular dichroism (diattenuation) and circular birefringence (retardance). The optical activity may be conditioned by the intrinsic optical activity of tissue containing molecules [see Fig. 7(d)] and by the form of the structural elements of tissue [see Fig. 7(c)]. Circular intensity differential scattering (CIDS) is a technique based on measurements of a difference between scattered intensities for left and right circularly polarized incident light. CIDS is related to the measurement of the M_{14} LSM element.[96] The form-CIDS can be associated with anisotropy caused by the helical structure of the particles.[193] The measurements of CIDS are used to study secondary and ternary structures of macromolecules and the polymerization of hemoglobin in sickling RBCs.[144] The experimental studies of polarization properties of laser radiation scattered by thin sections of optically active tissues show that laser polarization scattering can be employed for effective diagnostics of tissue structure.[86]

In a tissue containing chiral molecules exhibiting optical activity, such as glucose [see Fig. 7(d)], the polarization measurements can provide a noninvasive estimation of their concentration by using an optical rotatory dispersion method.[5,15,17,83,84,88] The angle of rotation of the plane of linearly polarized light passing through the media depends linearly on the concentration of the chiral species, the path length through the sample, and the specific rotation, which is a constant for a particular chiral molecule. The net rotation is expressed as $\phi_M = \alpha_\lambda LC$, where α_λ is the specific rotation for the species in $\mathrm{dm}^{-1}(\mathrm{g/L})^{-1}$ at the wavelength λ, L is the path length in dm, and C is the concentration in $\mathrm{g/L}$. Glucose in the body is dextrorotatory (rotates light in the right-handed direction) and has a specific rotation of $+52.6\ \mathrm{dm}^{-1}(\mathrm{g/L})^{-1}$ at the wavelength of 589 nm. At physiological concentrations and path lengths of $\sim$1 cm, optical rotation due to glucose is only 0.005 deg. However, a number of techniques providing the needed accuracy exist.[5,15,17,83,84,88] Most of them use crossed polarizers to measure rotation via alteration of amplitude or measure the relative phase shift of modulated polarized light passing through the sample.

It is difficult to measure sugar concentration in blood *in vivo* because of strong light depolarization due to light multiple scattering in superficial tissue layers of skin or mucosa. For this reason, the anterior chamber of the eye (aqueous humor) was suggested as a site for polarimetric measurement since scatter in the eye cornea is generally very small compared to other tissues.[88] The use of optical polarimetry for the noninvasive measurement of physiological glucose concentration in the anterior chamber of the eye of New Zealand white rabbits was reported.

To quantify changes in light polarization associated with alterations in tissue structure, the use of a Poincaré sphere has been suggested.[67,94,201,202] The coordinates on the Poincaré sphere are defined by the Stokes parameters [see Eq. (2)]. The Poincaré sphere makes it easier to identify at once different polarization states and, thus, is very practical in use (Fig. 22).

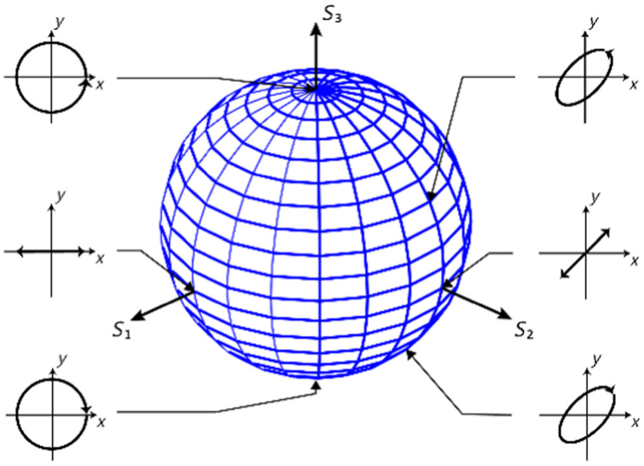

Fig. 22 The Poincaré sphere is the representation of three Stokes parameters $S_1 \equiv Q$, $S_2 \equiv U$, and $S_3 \equiv V$ that are plotted in 3-D space.[67,93,94,202] The distance from the center of the sphere indicates the degree of polarization; fully polarized states occupy a point on the surface of the sphere, whereas partially polarized states reside inside. For zero radius of the sphere, light is unpolarized. Each point on the sphere represents one state of polarization, so, for instance, a point at the northern pole $+S_3 \equiv +V$ signifies right-handed circular polarization, and the south pole $-S_3 \equiv -V$, left circular. States of linear polarization lie on the equator, and elliptical polarizations fill the remaining surface.

As we already discussed, when incident circular polarized light is multiply scattered, it is depolarized with the depolarization rate depending on the size and shape of scattering particles,[54,58,147] and on the number of scattering events (see Fig. 17).[13,147,203] Because of the intrinsic phase difference between two orthogonal linear components of the circularly polarized light, an incident state of polarization undergoes a flip in its helicity at backscattering.[75] For a tissue, represented as a system of large particles, due to strong forward scattering, the initial helicity of light is preserved.[54,58,147] Thus, the measured helicity of the scattered light with respect to the incident one will give information on whether it has been forward or backward scattered.

The experimental setup utilizing tissue probing by the circularly polarized light is presented in Fig. 23.[89,93] The backscattered light is collected at a distance d from the point of light incidence under the angle θ and then passed through a conventional polarimeter to measure its state of polarization. The MC simulation[93] indicated that when the source–detector separation is small ($d \cong 0$), the detected signal is likely to be overwhelmed

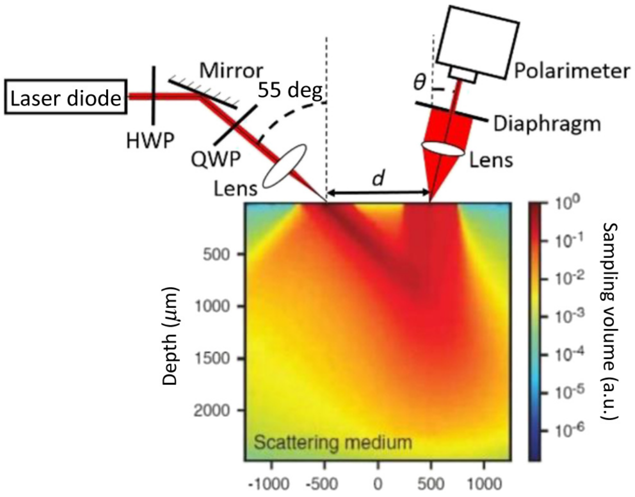

Fig. 23 Schematics of the experimental setup:[89,93] vertical polarized light from a laser diode (639 nm, 30 mW) is directed toward the sample at an angle 55 deg from the normal through a half wave plate (HWP) via mirror; the light is then altered by a QWP into a state of right circular polarized and/or right elliptically polarized, and focused onto the surface of the tissue by a lens; the source–detector separation d, as well as the angle of detection θ can be varied to change the sampling volume.

by the cross-polarized component due to single-backscattering events at or near the tissue surface. At bigger source–detection separations, the path lengths of the detected photons increase, thus, the contribution of the copolarized component to the detected signal dominates. Such behavior is also supported by data presented in Fig. 17, where the total circular light depolarization, $P_C \cong 0$, is happening at approximately five scattering events when intensities of cross- and copolarized components are equal to each other. With an increase of d, the multiplicity of scattering for detected photons increases; thus, the copolarized component prevails on the cross-polarized. The distance d causing complete depolarization is related to the optical properties of the medium, specifically the TMFP l_{tr} [see Eq. (44)]. For the size parameter of a tissue $ka \cong 5.9$, $d \cong 6l_{\mathrm{tr}}$ if detectable DOP $P_C \cong 10^{-1}$ and $d \cong 12l_{\mathrm{tr}}$ if it is $\cong 10^{-2}$.[54]

To observe cancer development, the measurement of the polarization properties of light backscattered from tissue samples at probing by a circularly or elliptically polarized laser beam was shown to be effective.[93,94,201] It was found that by tracking the Stokes vector of the scattered light on the Poincaré sphere, the difference between normal and cancerous tissue can be detected (Fig. 24).

Polar decomposition of the Mueller matrix measured in the forward detection geometry was used to extract the optical rotation of a chiral molecule (glucose) in turbid media and blood.[204] It was found that the optical rotation linearly increases with the concentration of glucose and the scattering multiplicity makes the rotation angle larger. The optical rotation in these media follows the Drude's dispersion relation. The blood measurements of diabetic patients show that the extracted rotation angle induced by glucose is in accordance with the clinical diagnosis. For interpretation of experimental data obtained for the Mueller matrix measurements done at transillumination of strongly scattering media, the results of Refs. 205 and 206 could be useful.

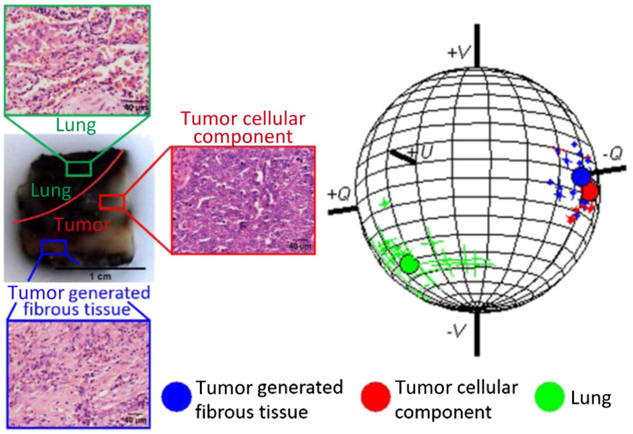

Fig. 24 Lung tissue embedded in paraffin wax (left) shows the boundary between healthy lung and tumor tissue (red line) marked based on histological examination.[93,94,201] Microscopy images of haematoxylin and eosin stained 5 μm tissue sections are shown in the colored squares and their position on the block is marked by the corresponding squares. The Poincaré sphere (right) shows the mean Stokes vector of the right elliptically polarized light backscattered from the region of healthy lung tissue (green), tumor generated fibrous tissue (blue), and the tumour cellular component (red); dots with error bars represent a single measurement and the larger circles represent the mean state of polarization; $d = 1.5$ mm and $\theta = 30$ deg (see Fig. 23).

6 Polarization Imaging

6.1 *Introduction*

Polarization imaging is an innovative and prospective technology for medical diagnostics.[2–6,9,15,16,18–22,29,86,132,144,166,170,171,179–183,202–273] The techniques are from the simplest and robust to unique and comprehensive, such as polarized light microscopy (PLM) and ellipsometry,[48,49,76,86,209–213,217] linear polarization degree mapping and gating,[8,10,19,25,27–29,51,57,60,71,95,152,162,169–171,174,207,218] polarized fluorescence imaging,[179–183] full-field polarization-speckle technique,[15,29] polarized light spatial frequency domain imaging,[214] two-dimensional backscattering Mueller matrix measurements,[18,20–22,79–82,91,92,105,145,154,194] circularly polarized laser beam probing and Poincaré sphere tracking,[67,94,201,202] Mueller matrix polarimetric endoscopy,[215,216,261] spectral light scattering polarimetry,[7,23,24,162,217,219] Mueller matrix fluorescence spectroscopy,[220–222] polarized Raman spectroscopy,[223,224] PS-OCT,[2,5,9,15,21,22,61,62,66,67,103,129,132,163,202,225–250,256–260,268] and polarization-resolved nonlinear microscopy[132,133,189,190,251–253,262] based on vector Bessel beams[254] or polarization modulation for light focusing through turbid tissue.[255] Single cell polarization studies[263,264] and nanoparticle enhanced cell and tissue polarization imaging,[163,265–270] as well as clinical applications of different polarization imaging technologies[198,199,257–260,271–273] are also of great interest.

6.2 *Degree of Polarization Imaging*

The simplicity of the technical arrangement is one of the advantages of the linear polarization degree mapping and gating method. Only two polarization filters are needed. One linear polarizer is mounted on the light source and another is placed in front of the camera and is free to be rotated with respect to the first polarizer to provide either parallel or perpendicular orientation to the direction of polarization of the illuminating light.

For instance, by using polarized light photography at parallel polarizers, one selectively probes superficial features of the skin.[51,59,170,207,273] Surface features can be viewed without image distortion by underlying pigmented lesions or erythema, and by light coming from the skin depth and underlying tissues. Instead, with the crossed polarizers, the surface irregularities, such as scales, wrinkles, and pore openings, are eliminated from the image. Therefore, the evaluation of melanin content, erythema, and inflammatory lesions is possible.[207,273] Human skin UV reaction, photodamage, response of psoriatic and acne lesions to treatment, and irritancy were evaluated using polarization photography.[207]

A calculation of degree of polarization for each pixel of the polarization image gives new important features of the technique—degree of polarization imaging (DPI).[10,170] Two images received for the copolarized, $I_{||}$, and cross-polarized, $I_{\perp}$, components are algebraically combined to yield a residual DPI described by Eq. (4). The numerator in this equation is sensitive only to polarized light and rejects randomly polarized diffuse light. On the other hand, the attenuation factor due to absorption (melanin, hemoglobin) is common to all terms (in numerator and denominator) of Eq. (4) and thus cancels out. As skin freckle is a superficial melanin pigmentation, it acts like an absorptive filter that attenuates light passing in/out of the skin, which affects both $I_{||}$ and $I_{\perp}$ images approximately to the same degree. Therefore, freckle melanosomes do not influence the DPI image [Figs. 25(a) and 25(b)]. For pigmented nevi, melanin are usually imbedded deeper in the skin; thus due to

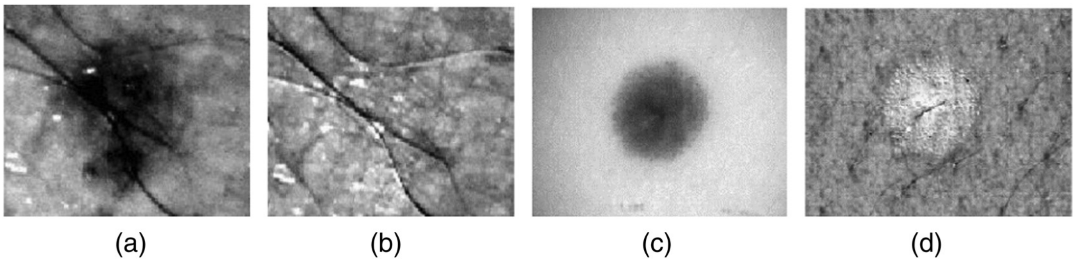

Fig. 25 DPI:[10] a polarization image removes the melanin from a freckle, compare (a) bright-light image and (b) DPI; freckle melanosomes do not appear to influence the image; a polarization image removes the melanin and shows apparent scatter from benign pigmented nevus structure, compare (c) bright-light image and (d) DPI.[10]

influence of scattering of surrounding tissues, the statement of equality of melanin absorption affecting on $I_{||}$ and $I_{\perp}$ images is not yet completely valid. Thus, the calculated DPI may not perfectly eliminate melanin inclusion; however, it is sufficient to see apparent scattering from nevus structures [Figs. 25(c) and 25(d)].

Figure 26 presents monochromatic images of burn-injured skin surface obtained for co- and cross-polarized light detection in the spectral band of hemoglobin absorption. The DPI image contrast (~0.5) considerably exceeds the contrast of co- and cross-polarized images (0.08 to 0.13). The depth of DPI is of 100 to 150 μm.

The quantitative estimation of epithelial cellular structures *in situ* done by polarized light scattering spectroscopy is described elsewhere.[7,15,24,71,169–174] A cross-polarized multispectral technique allows for real-time imaging of skin structures with the resolution down to 12 μm over a wide-field of ~4 cm^2 (Fig. 27).[95,218] The images acquired at 440 nm reject light remitted from the epidermis, thus enabling a high-resolution visualization of collagen in the papillary dermis.

This section presents a few examples of polarization imaging and evaluation of structural properties of tissues that normally show multiple scattering. For some tissues, like tendon, tissue sectioning is enough to see and evaluate collagen birefringence on the background of relatively small scattering (Fig. 28).[114]

6.3 *Polarized Light Microscopy*

For other tissues, such as eye sclera or skin, either optical clearing that reduces light scattering is needed to estimate birefringence for thick tissue sections,[15] or one is able to use very thin sections of around 30 μm.[213] PLM of thin tissue sections demonstrates accurate, repeatable, and robust data on fiber orientation with μm-scale resolution over a broad field of view (Fig. 29).[213] Similar to the optical scheme presented in Fig. 28, a white light source and two polarizing filters were used in PLM. Multiple images were acquired with various filter orientations relative to the sample separated by 45 deg. The signal intensities from the set of images were used to compute the local orientation at each CCD pixel with weighting by a parameter denoted as Energy,

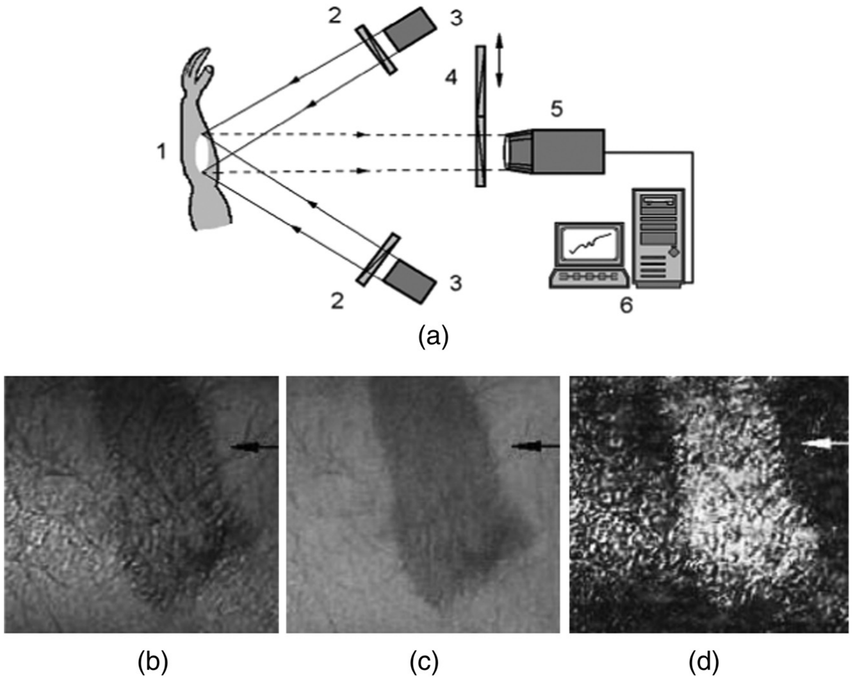

Fig. 26 (a) Polarization spectral imaging: 1, skin site; 2, polarization filters; 3, light source; 4, polarization and interferential filters; 5, monochrom CCD camera; 6, PC; polarization-spectral ($\lambda = 550$ nm) images of skin burn lesion of the volunteer: (b) a copolarized image; (c) a crossed-polarized image; (d) DPI.[170]

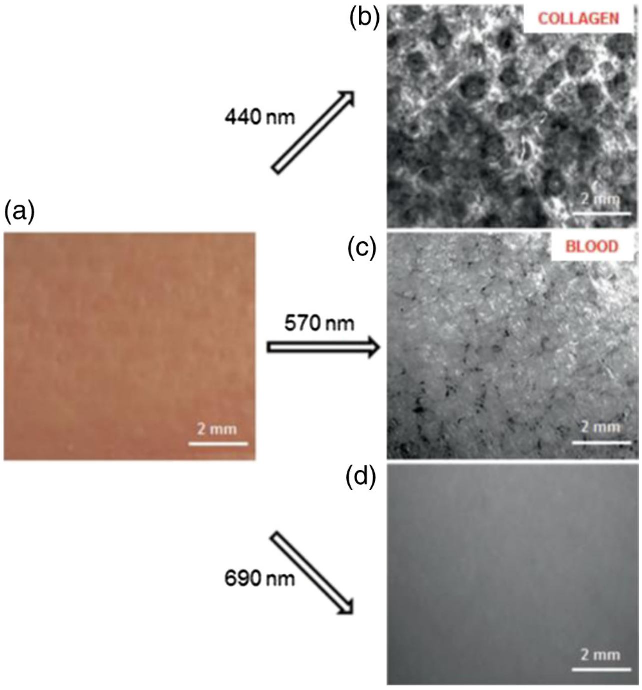

Fig. 27 Cross-polarized imaging at different wavelengths emphasizes different features of human skin *in vivo*: (a) skin photograph; cross-polarized image at (b) 440 nm, (c) 570 nm, and (d) 690 nm.[95]

$$\text{Energy}^2 = (I_{90} - I_0)^2 - (I_{135} - I_{45})^2, \tag{71}$$

where I_α is the pixel intensity at an angle α to the analyzer direction.

PLM may have a broad range of applications where collagen fiber orientation and organization of a tissue are of interest, in particular, to understand tissue biomechanics.[244,245] Additional coherence gating in PS-OCT also allows one to measure linear birefringence on the background of strong scattering as in intact human eye sclera.[240]

6.4 *Two-Dimensional Reflection and Transmission Light-Scattering Matrix*

The registration of two-dimensional polarization patterns for the reflection and transmission of a polarized incident narrow laser beam is the basis for the polarization imaging technique. The most informative images can be received by using the Mueller matrix approach. To determine each of the 16 experimental LSM, a total of 16 images should be taken at various combinations of input and output polarization states. Figure 30 demonstrates corresponding LSMs calculated for a turbid medium with parameters characteristic to tissues.[15] The patterns of the reflection Mueller matrix XE “Mueller matrix” are identical to those reported elsewhere.[108,149,150] The symmetries in the patterns can be explained by the symmetries in the single-scattering Mueller matrix and the medium.[149] The transmission and reflection matrices have quite different patterns. One of the differences appears in M_{31} and M_{13} elements. Due to the mirror effect in the reflection process of the scattered light, they are antisymmetric in the reflection mode but symmetric in the transmission one.

The comparison of the Mueller matrix elements calculated for the microsphere-silk tissue model and polarized reflectance images of fresh skeletal muscle is shown in Fig. 31.[85] For polarized reflectance, a total of nine equi-intensity profile (EIP) images are displayed corresponding to different combinations of incidence and reflectance polarization states, i.e., horizontal linear (H), vertical linear (V), and 45 deg linear (P). The first set of QWP and linear polarizer controlled polarization of the incident laser beam and the second set, placed in front of the CCD, controlled the polarization of the backscattered light.

The EIP images for skeletal muscle and a microsphere-silk sample do not match quantitatively to each other. However, they are quite similar in form, which proves the skeletal muscle model as a combination of both spherical and cylindrical scatterers. In particular, the VV image, which corresponds to vertical incident polarization and vertical reflectance polarization states, has the highest intensity and is elongated along the x-axis (the perpendicular direction to cylindrical scatterers). The HH image shows a distinct rhombic shape with more balanced intensities along the x- and y-axes. The EIPs of the other images have patterns that are between HH and VV. Images have a diagonal symmetric relationship, see HV-VH, HP-PH, and VP-PV. The differences in VV and HH images can be explained using Mie scattering theory for spheres and infinitely long dielectric cylinders.[85,96] Polarization maintaining photons tend to be scattered to the perpendicular direction of cylindrical scatterers (x), which gives the specificity of EIP patterns in comparison with the pure spherical particle tissue model.

The degree of polarization (DoP) maps or depolarization maps for imaging of polarization dependent alterations in the depolarization is also used for optical imaging.[105,106] The depolarization as a function of input polarization is described by Eq. (14), which can be expressed via the angle, characterizing the orientation of the ellipse of the input polarization state, φ_o and phase retardance δ [see Eqs. (15) and (16)].[105]

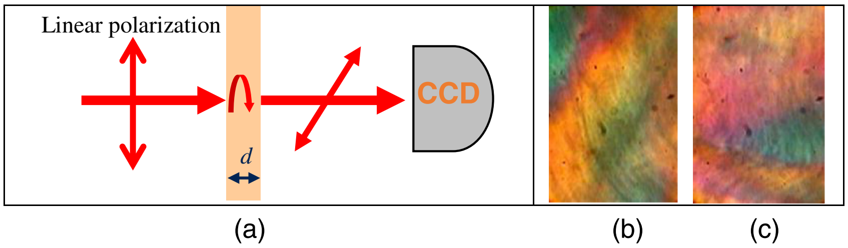

Fig. 28 Linear birefringent tissue polarization imaging: (a) tissue layer working as a phase plate (linear birefringent retarder); (b) and (c) images for two different rotation angles of the human tendon sample ($d \cong 0.5$ mm cut along fibril) in crossed polarizers (polarization filters) at a white light illumination (measured by G. V. Simonenko).[114]

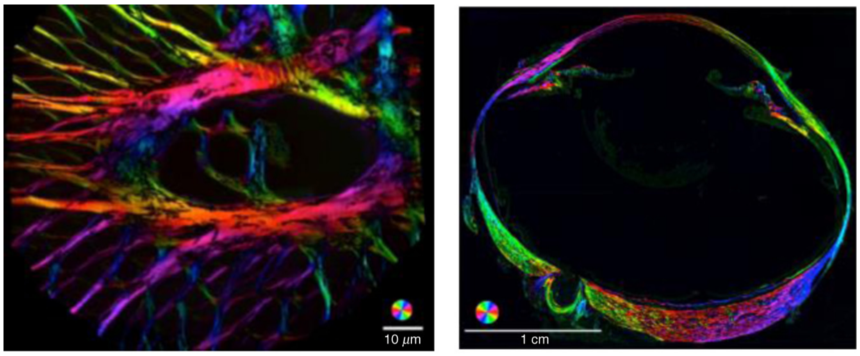

(a) (b)

Fig. 29 PLM images of sheep eye tissue sections: (a) lamina cribrosa of optic nerve head and (b) whole-globe axial eye section. Image sets of a tissue section were taken, and for each set, the fiber orientation was calculated (color coded).[213]

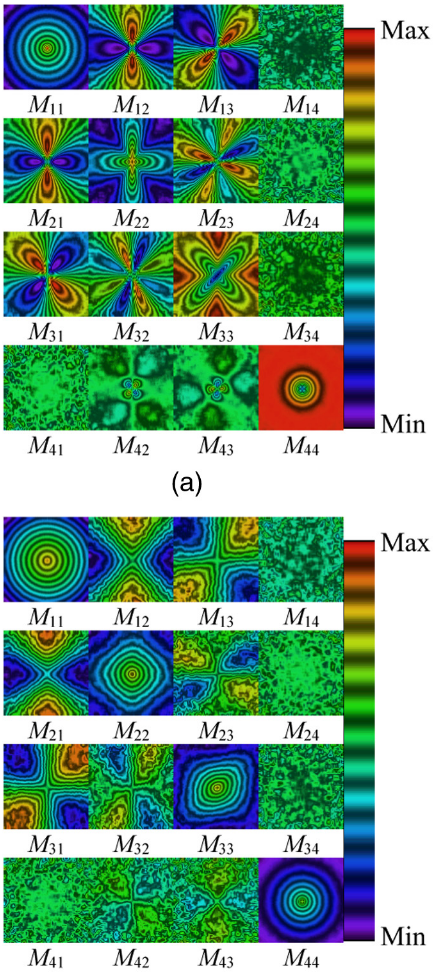

(a)

(b)

Fig. 30 (a) Reflection and (b) transmission Mueller matrices of a slab of turbid medium with a scattering coefficient of 4 cm^{-1} and a scatterer radius of 0.102 μm.[15] The calculated Mueller matrix elements are normalized to the M_{11} element to compensate for the radial decay of intensity. Each of the image is displayed with its own color map to enhance the image contrast. The size of each image is 4×4 cm^2.

Measurement of Mueller matrix requires at least 16 intensity measurements at different input polarization states, for each of which the scattered light is analyzed with four different analyzer configurations (Fig. 19). The incident polarization states are created by taking four different orientations of the fast axis of the QWP with respect to the pass axis of the polarizer. The DoP maps are constructed from depolarization measurements for light emerging from different spatially separated points in the tissue sample at its illumination with a narrow laser beam (Fig. 32). These maps can be used to extract the scattering coefficient, the anisotropy factor, and the mean particle size.[150]

6.5 *Polarization-Sensitive Optical Coherence Tomography*

OCT is an interferometric technique providing high-resolution cross-sectional tissue images by detection of the intensity of a low-coherence light reflected from tissue layers or other inhomogeneities.[2,5,274] To study complex anisotropic tissues possessing microscopic fibrous structures, including collagen fibers and nerve fibers, a conventional OCT was improved by enabling measurements of signal polarization characteristics, which is the PS-OCT.[2,5,9,15,21,22,61,62,66,67,103,129,132,163,202,225–250,256–260,268] In-depth measurements of Stokes parameters allow for determination of tissue birefringence (phase retardation), dichroism (diattenuation), and optic-axis orientation. Advanced PS-OCT systems give the possibility for tissue imaging by measurements of a full Jones matrix[103,202,239,241,242] or Mueller matrix[61,62,67,202,239] for each pixel, as well as representing results of imaging in the form of the Poincaré sphere.[67,202,239]

In the majority of studies by PS-OCT, the criterion of pathology in tissue is a measured decrease in tissue macroscopic birefringence. However, it is difficult to make correct measurements of birefringence for depths of more than 300 to 500 μm. For deeper layers (up to 1.5 mm), a much simpler version of PS-OCT—the cross-polarization OCT (CP-OCT)—can be employed.[225–228,246–248,250,260] Light depolarization caused by light scattering and tissue birefringence both lead to the appearance of a cross-polarized component in the backscattered light. It is important to note that both types of images—conventional and cross-polarized—are obtained from the same tissue site. Neoplastic pathology development is characterized by the changes in the amount of collagen fibers and their spatial organization to which CP-OCT is very sensitive. The facilities of the

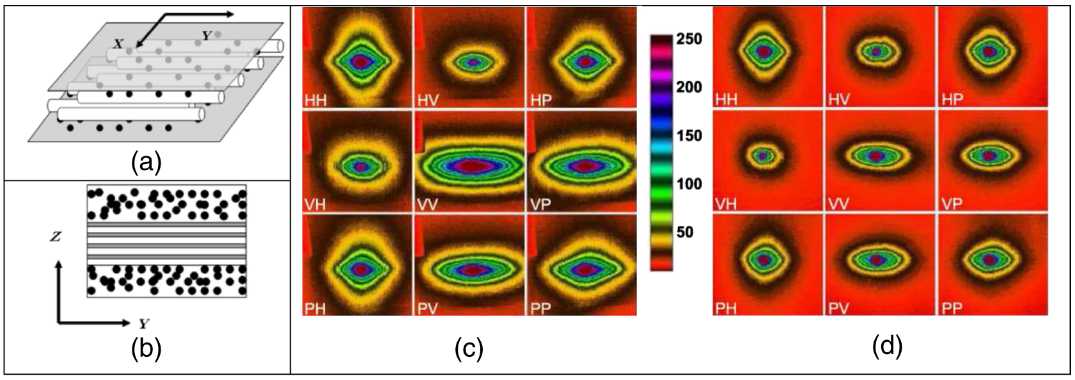

Fig. 31 Polarized reflectance images from microsphere-silk sample model (MC simulation) and fresh bovine skeletal muscle:[85] schematics of the three-layer microsphere-silk sample (the first and third layers are 200-nm-diameter polystyrene microsphere in water ($n_{\mathrm{pm}}/n_{\mathrm{w}} = 1.59/1.33$); the second layer is 1.5-μm-diameter well-aligned silk fibers in water $n_{\mathrm{sf}}/n_{\mathrm{w}} = 1.56/1.33$; total thickness of the sample is 2 cm; (a) and (b) thickness of the first and third layers is adjustable, and that of the second layer is 3 mm; polarized reflectance images ($\lambda = 633$ nm) of (c) microsphere-silk sample and (d) fresh skeletal muscle. The image size is 1.4 cm × 1.27 cm. The muscle fibers and silk fibers are along the vertical direction.

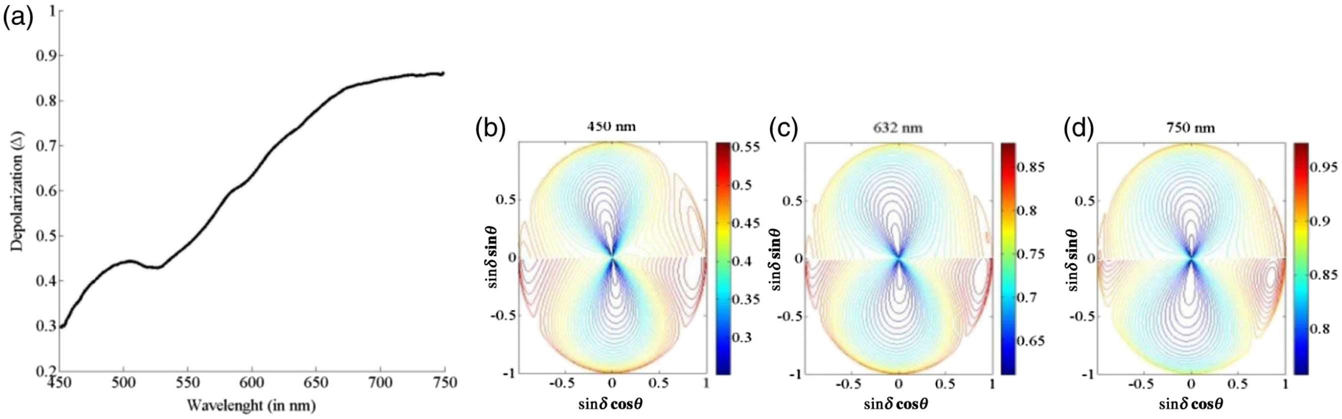

Fig. 32 (a) Wavelength dependence of depolarization and [(b), (c), and (d)] depolarization maps for mouse heart tissue at 450, 632, and 750 nm.[105]

CP-OCT to give additional structural information were demonstrated by *ex vivo* human esophagus scar tissue imaging,[228] by study of evaluation of oral mucosa collagen[246] and human bladder mucosa pathologies *in vivo*,[247] and by multimodal optical imaging for characterization of atherosclerotic plaques.[248]

A method of mapping cardiac muscle structure using the local optical axis obtained from PS-OCT measurements was described.[234,235] The true local depth-resolved tissue anisotropic parameters, such as optical axis, retardation, and diattenuation, were obtained using a Jones matrix based PS-OCT system and designed algorithm for extraction of parameters. The cross-helical laminar structure of myocardial fibers was clearly visualized using the developed optical tractography technology.[235]

The polarization-sensitive light–tissue interactions in human retina studied by PS-OCT were recently discussed and their use for retinal diagnostics was demonstrated.[238] These are birefringence of the RNFL, which can be used as a marker for glaucoma diagnostics, and depolarization observed in the retinal pigment epithelium, which can be used to detect lesions like drusen or atrophies in age-related macular degeneration.

A novel PS-OCT system combined with retinal tracking functionality was designed.[236,237] It consists of integrating a PS-OCT and a line-scanning laser ophthalmoscope (LSLO). Based on the images acquired by the LSLO, the system compensated for motion artifacts by adjusting the OCT scanner position in real time. The PS-OCT system was tested in healthy eyes demonstrating the usefulness and the superior image quality achieved in a real clinical situation.

PS-OCT has been used in a wide variety of applications, including correlating burn depth with a decrease in birefringence, *in vivo* imaging of human burn injuries, measuring the birefringence of RNFL,[67,202,238,239,257] monitoring the onset and progression of caries lesions, demineralization and remineralization processes,[249,250] clinical monitoring of enamel lesions,[260] as well as collagen restoration in bacteria-infected wounds at antimicrobial photodynamic treatment.[258,259]

7 Optical Clearing

The refractive index (RI) mismatch exists between cellular tissue components, such as cell membrane, cytoplasm, cell nucleus and other organelles, melanin granules, and the extracellular fluid. For fibrous connective tissue, there is an index mismatch of interstitial fluid (ISF) and long strands of scleroprotein (collagen-, elastin-, or reticulin-forming fibers). The scattering particles (organelles, protein fibrils, membranes, and protein globules) exhibit a higher density of proteins and lipids in comparison with the ground substance and, thus, a greater RI ($n_s = 1.39$ to 1.47). The RI of the ISF, cytoplasm, and blood plasma, where fibers, cell organelles, or blood cells are distributed, is ~1.33 to 1.35. The scattering efficiency of a tissue depends on the (RI) mismatch between the RIs of ISF n_{is} and scatterers n_s. For the tissue model that can be presented as a monodisperse system of thin dielectric cylinders ($n_s \equiv n_{\mathrm{cyl}}$) with a number of fibrils per unit area ρ_s, the scattering coefficient μ_s has the form[5]

$$\mu_s \cong \rho_s \left(\frac{\pi^5 a^4 n_0^3}{\lambda_0^3} \right) (m^2 - 1)^2 \left[1 + \frac{2}{(m^2 + 1)^2} \right], \tag{72}$$

where $\rho_s = f_{\mathrm{cyl}}/\pi a^2$, f_{cyl} is the surface fraction of the cylinders' faces, a is the cylinder radius, n_0 is the mean RI of the tissue, λ_0 is the light wavelength in free space, and $m = n_{\mathrm{cyl}}/n_{\mathrm{is}}$ is the relative RI of cylinders (scatterers) to the background (medium of the interfibrillar space, ISF).

The described tissue model is applicable to any fibrous soft tissue, including sclera, skin dermis, and muscle. A bit more sophisticated model is presented in Fig. 31, which combined cylindrical and spherical particles. To provide optical clearing, the RI of the optical clearing agent (OCA) should be higher than the RI of the ISF and cytoplasm. Therefore, diffusion of foreign molecules of an OCA inside tissue will reduce the RI mismatch ($m \to 1$) and correspondingly will lead to a drop of the scattering coefficient ($\mu_s \to 0$). The single-scattering directness, described by a scattering anisotropy factor g, is also sensitive to RI matching [see Eq. (11)]; it increases with the better matching conditions.[5] As a result of these two processes, reduced scattering coefficient $\mu_s' = \mu_s(1-g)$ becomes a very sensitive function of RI matching. Therefore, TMFP of a photon, which is defined by Eq. (42), is a key parameter for image contrast and probing depth, including polarization-sensitive measurements (see Fig. 18), and could be increased significantly at RI matching. It follows from Eq. (72) that a relatively small increase in the RI of the background matter n_{is} will cause a few-fold decrease of the scattering coefficient μ_s.

There are several main mechanisms of light scattering reduction in living tissues induced by an OCA:[5,201,275–297] (1) partial replacement of the ISF by an OCA,[5,144,275–282,289–295] (2) dehydration,[5,144,277–282,284,289–295] (3) structural modification (better ordering),[5,144,283,284,289–295] and (4) reversible dissociation or solubility of collagen.[285–288]

For fibrous connective tissue similar to sclera, dura mater, dermis, the first mechanism could be prevalent for many of the tested chemical agents for which the molecule size is much less than the mean cross-section of interfibrillar space. Both the first and the second processes mostly cause matching of the RIs of the tissue scatterers (cell constituents, collagen, and elastin fibers) and the cytoplasm and/or ISF. The RI matching is manifested in the reduction of the scattering coefficient ($\mu_s \to 0$) [Eq. (50)] and increase of single-scattering directness ($g \to 1$). The second and the third mechanisms are characteristic for application of hyperosmotic agents.

Structural modification is manifested as tissue shrinkage; it causes the near-order spatial correlation of scatterers (see Fig. 11)[5,144,283] and, as a result, the increased constructive interference of the elementary scattered fields in the forward direction and destructive interference in the perpendicular direction of the incident light, which may significantly increase tissue transmittance even at residual RI mismatch.

If an OCA, like sugars, sugar alcohols, and other organic solvents, is applied to living tissue for a limited time (from minutes to a few hours), it could reversibly destabilize the collagen structure by interactions of hydrogen bonds between collagen and OCA molecules, i.e., lead to reversible collagen solubility that correlates with tissue optical clearing potential.[286–288] A lesser hydrodynamic radius of tissue scatterers (collagen fibers) in that case could be the main reason for reduction of tissue light scattering.

All these mechanisms, which usually coexist, can lead to a significant decrease of the reduced scattering coefficient μ_s' of fibrous connective tissues, such as skin dermis, eye sclera, dura mater, tendon, skeletal muscle, and myocardium.

Dynamics of tissue polarization structure at OCA immersion can be easily observed using an optical scheme with a white light source and a tissue sample placed between two in parallel or crossed polarizers (Fig. 28). The evolution of polarization images (crossed polarizers) during human sclera optical clearing is shown in Fig. 33. A tissue layer works as a phase plate (or number of phase plates),[296–298] whose linear birefringence is spatially and temporally dependent. As scattering goes down with time due to RI matching, the birefringence of fibrillar structure of the sclera affects the transmittance of the optical system in crossed polarizers (see also Fig. 28). The spatial inhomogeneities of images are due to spatial variations of the sample thickness and structure, which both may influence the efficiency of OCA impregnation and corresponding phase shift between the orthogonal optical field components.

By comparison of kinetics of optical clearing curves for the linearly polarized component of transmitted intensity $I_{||}$, which is in parallel to the polarization of the incident beam, and the total transmitted intensity I_T of scleral tissue layer, presented in Fig. 34, we can conclude that OCA-induced optical clearing leads to an increase in the length of tissue depolarization ability.[279] The intensity of transmitted linearly polarized light is significantly improved. As far as the tissue sample is immersed, the number of scattering events decreases and the residual polarization degree of transmitted linearly polarized light increases. As a result, the kinetics of the average transmittance (I_T) and degree of polarization ($I_{||}$) are correlated. It is important to note that there is also some correlation between the total transmitted intensity (I_T) and the intensity of the

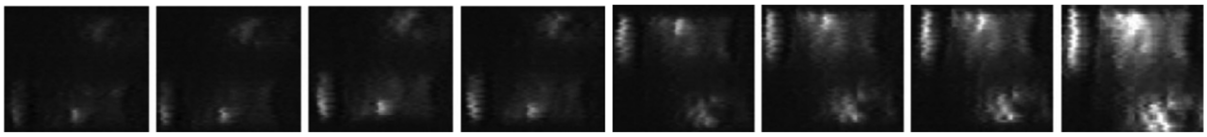

Fig. 33 Polarization images of a sclera sample (white light source, crossed polarizers). Images from left to right correspond to 4, 5, 6, 7, 8, 9, 9.5, and 10 min of tissue impregnation by Trazograf-60™ (x-ray contrast agent). Supporting wires of the sample are seen for the translucent tissue (see Refs. 5 and 144).

orthogonal polarization component ($I_\perp$), which can be explained as an inclusion of tissue birefringence that is revealed at low scattering conditions (see Fig. 33). Data presented in Fig. 34 demonstrate the reversibility of tissue optical clearing by a successive OCA and physiological solution application.

As a spatially coherent laser beam was used in this experiment, the speckle pattern transformation accompanied optical clearing effects (see inserted far-field speckle patterns in Fig. 34). Transmitted intensities $I_T, I_{||}$, and $I_\perp$ were measured as mean speckle intensities averaged over the scanning trace (1.5 mm) in the paraxial region. It is well seen that the speckle patterns are transferred from small-size and more or less homogeneously distributed speckles, characteristic for multiple scattering, to big-size inhomogeneously distributed speckles with a large portion of ballistic photons in the central part of the pattern.

Reduction of the scattering at optical immersion makes it possible to detect the polarization anisotropy of tissues more precisely and to separate the effects of light scattering and intrinsic birefringence of the tissue polarization properties. It is also possible to study the features of birefringence of form at optical immersion. When immersion is strong, the RI of the tissue anisotropy structure will be close to the RI of the ground media, and the birefringence of form should be eliminated. Because both phenomena—light scattering and birefringence of form— are based on the RI mismatching—scattering due to irregular refractive index variations and birefringence due to regular ones [see Eqs. (21) and (72)], strong immersion condition is a way to evaluate a molecular intrinsic birefringence of collagen fibrils.

Figure 35 shows the reversible loss of turbidity and birefringence in rodent tail tendon observed at glycerol (13 M) application.[285] The dark background in each of the images demonstrates the extinction of illuminating light at crossed polarizers. Characteristic banding patterns observed in the tendon sample indicate ordered fibril organization. The distribution of pattern brightness corresponds to the distribution of a phase shift between orthogonal optical field components [see Eq. (21)], and the background smooth brightness corresponds to light scattering. Loss of transmittance at the sample edges and appearance of bright spots in the middle of the sample in the course of glycerol action indicate RI matching of collagen fibers. The complete RI matching at the edge region happens earlier than in the middle of the sample, and turns tissue to lose scattering and birefringence completely in this region. In the middle region of the sample, refractive index matching is not completed and most scattering is reduced (loss of turbidity); thus, bright and dark areas corresponding to a certain phase shift are well seen. Tissue shrinkage at glycerol action, due to tissue dehydration, as well as hypothesized by authors of Ref. 286 the reversible dissociation of collagen, may have influence on the pattern formation. The rehydration of the tissue sample in saline makes the banding structure fully visible in the crossed polarizers due to resumption of the tissue birefringence and turbidity approximately to the initial states.

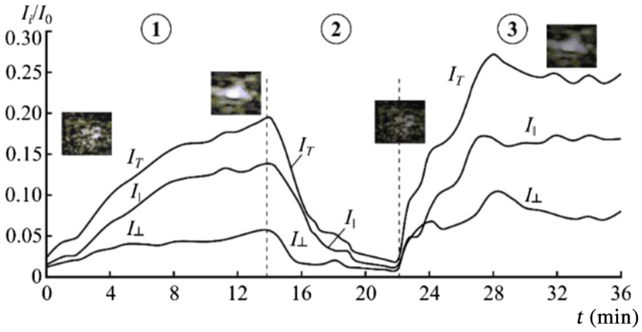

Fig. 34 The time-dependent transmittance (I_i/I_0) of the human sclera specimen ($d = 0.4$ mm) measured with a small diaphragm for linear polarization of the incident laser beam I_0 with $\lambda = 633$ nm;[279] $I_i = I_{||}$, $I_\perp$ are two orthogonal polarization components of the transmitted light; $I_{||}$ is parallel to the polarization of the incident beam and $I_\perp$—perpendicular; $I_T = I_{||} + I_\perp$; the subsequent measurements for the specimen kept at first in Trazograpf-60$^{\text{TM}}$ (x-ray contrast agent), zone (1); in saline, zone (2), and again in the OCA solution, zone (3); insets show far-field speckle patterns in the transmitted light before and after optical clearing without polarization filtration.

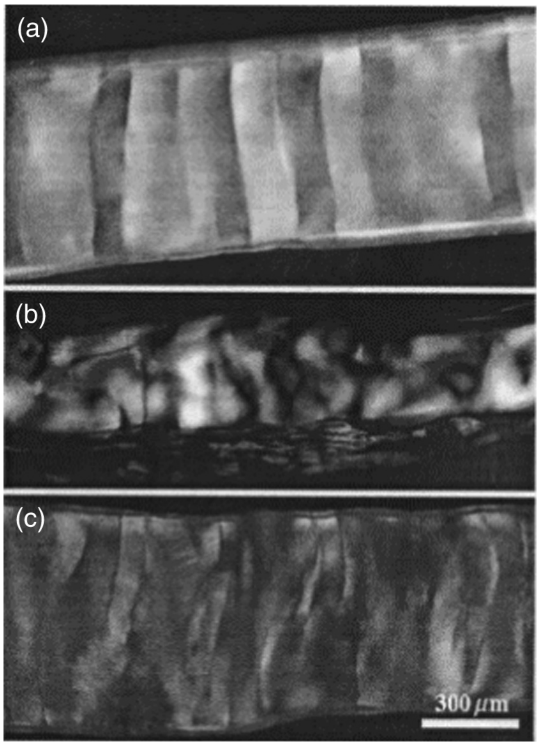

Fig. 35 Reversible loss of turbidity and birefringence in rodent tail tendon following glycerol (13 M) application observed by PLM at crossed polarizers:[285] (a) before glycerol application, banding patterns observed in tendon indicate ordered fibril organization; (b) at glycerol application, loss of transmittance at the sample edges and bright spots in the middle indicate RI matching of collagen fibers; (c) the tissue sample after rehydration in saline (figure was kindly presented by Alvin T. Yeh and Bernard Choi).

The backreflected circularly polarized light from a scattering medium at its immersion optical clearing was investigated for tissue phantom using the experimental setup shown in Fig. 23.[201] The high sensitivity of the parameters of the reflected circularly polarized light to changes of phantom scattering properties was demonstrated (Fig. 36). The improvement of the polarization ability of the backreflected circular polarized light at optical clearing with an increase of OCA concentration (glycerol) is well seen.

8 Nanoparticle Enhancement of Contrast of Polarized Light Microscopy

Another possibility to enhance polarization contrast at cell and tissue imaging is to use nanoparticles.[163,265,–270] Recent advances

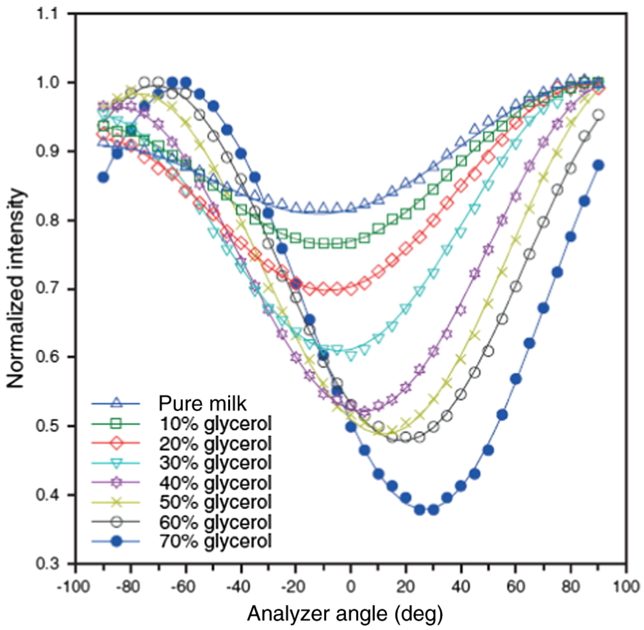

Fig. 36 Polarization-sensitive measurements at optical clearing:[201] normalized intensity of light backscattered from milk and detected using a quarter wavelength plate and rotating analyzer in front of detector (see Fig. 23); each curve shows results for samples diluted by given amounts of water solution of glycerol: 10, 20, 30, 40, 50, 60, and 70%.

in plasmonic nanoparticle synthesis with different shapes and composition give new opportunities for PLM. For instance, a combination of stellated gold nanoparticles (GNPs) with polarization-sensitive dark-field microscopy was successfully used for detecting molecular assemblies and tracking of individual epidermal growth factor receptors within single live cells with a high signal-to-background ratio.[265] Depolarization of linearly polarized light by stellated nanoparticles was over 15-fold more efficient than similar-sized spheroidal nanoparticles. This allowed one to provide a robust detection of nanoparticle labeled molecules in cross-polarized imaging where the intrinsic light scattering from cells is significantly reduced. A single molecule sensitive imaging with no signal degradation was demonstrated.

Polarization properties of differently shaped GNPs, such as rods, tetra-pods, flowers, and stars, were studied by using Mueller matrix measurements.[266] It was shown that for all the particle shapes investigated, the depolarization for circularly polarized light is larger than that for linearly polarized light by about a factor of 2, and depolarization is largest for the rod-shaped particles. The wavelength dependences of the retardance and diattenuation properties of the GNP suspensions were also investigated experimentally and theoretically using discrete dipole approximation.

For Intralipid tissue phantoms, it was demonstrated that at a given extinction coefficient, the absorption of the GNPs contributes more to the depolarization of the turbid medium.[267] The GNP scattering is significant only for the larger-sized particles. The depolarization of GNPs dominates in the low-scattering phantoms. For highly scattering samples, GNP absorption significantly modulates the depolarization spectra of the turbid medium.

Standard PS-OCT hardware was used to discriminate cells and gold nanorods within 3-D tissue cultures based on motility-, autocorrelation-, and polarization-sensitive algorithm.[163] The amplitude (motility) and time scale (autocorrelation decay time) of the speckle fluctuations were combined with the cross-polarization pixel-wise OCT imaging. This combination of metrics provided high specificity for discriminating diffusive gold nanorods and mammary epithelial cell spheroids within 3-D tissue culture.

A novel approach toward significant enhancement of image contrast of OCT microscopy was recently demonstrated.[268] It is based on the combination of a circular-polarization OCT system with 3-D chiral nanostructures as contrast agents. By detecting the circular intensity differential depolarization, high-quality images of single chiral nanoparticles underneath a 1-mm-thick tissue-mimicking phantom were successfully acquired.

Ultrahigh polarimetric image contrast enhancement for skin cancer diagnosis using InN plasmonic nanoparticles in the terahertz range was demonstrated using Mueller matrix imaging.[269] Detection of water content in the tissue with high sensitivity was made possible yielding a limit of detection down to 0.0018% for relative alterations in the water content.

A single-cell optical clearing methodology is also prospective for improvement of polarization-sensitive cell imaging in combination with plasmonic nanoprobes, hyperspectral dark-field microscopy, angular elastic light scattering, and optical tweezers.[264,270]

9 Conclusion

The author hopes that the summarized intrinsic origins of tissue polarization anisotropy, presented discussion of fundamentals, basic theories, and experimental techniques for the study of polarized light interaction with biological tissues and cells will enable readers to be acquainted with and to understand the main specific features of polarized light propagation and interaction in random and quasi-ordered tissues with basic single and multiple scattering. *In vitro* and *in vivo* studies demonstrate the abilities of polarization-sensitive techniques to provide diagnostics and monitoring of tissue lesions and other abnormalities. We emphasize that immersion optical clearing and nanoparticle labeling are useful technologies for tissue polarization properties differentiation and quantification, and for further improvement of polarization imaging facilities and polarization properties control.

In spite of the presented discussion of the recent key polarization-sensitive optical methods that make possible the quantitative early pathology diagnostics, polarization optical imaging is a rapidly developing, innovative, and prospective technology that could not be overviewed in one paper. Thus, many novel polarization techniques, such as full-field polarization-speckle technique, polarized light spatial frequency domain imaging, Mueller matrix polarimetric endoscopy, spectral light scattering polarimetry, Mueller matrix fluorescence spectroscopy, polarized Raman spectroscopy, PS-OCT, and polarization-resolved nonlinear microscopy, were only mentioned with some basic referencing. The author leaves this to the readers for self-learning.

A comparative study aimed to describe the similarities and differences between the Jones and Stokes–Mueller formalisms at modeling polarized light propagation, using MC numerical simulations done by authors of Refs. 299 and 300 also should be of interest to the readers. In these papers, the theoretical concepts of pure and partially polarized light propagation and detection, as well as fundamentals and historical aspects of matrix polarization optics, are presented.

Acknowledgments

Many results presented in this paper on modeling of tissue polarization properties were received by Irina L. Maximova, who passed away in 2013. I will remember her forever as a very talented scientist and a great person. I would like to thank Yurii P. Sinichkin, Georgy V. Simonenko, Dmitry A. Zimnyakov, Lihong V. Wang, Steven L. Jacques, and Igor Meglinski for a long-time collaboration in the field of tissue polarization optics. This study was supported in parts by grants 14.Z50.31.0004 of the Government of the Russian Federation, 14-15-00186 of the Russian Science Foundation, and the Tomsk State University Academic D. I. Mendeleev Fund Program.

References

1. G. Müller et al., Eds., *Medical Optical Tomography: Functional Imaging and Monitoring*, Vol. **IS11**, SPIE Press, Bellingham, Washington (1993).
2. L. V. Wang and H.-I. Wu, *Biomedical Optics: Principles and Imaging*, Wiley-Interscience, Hoboken, New Jersey (2007).
3. D. Boas, C. Pitris, and N. Ramanujam, Eds., *Handbook of Biomedical Optics*, CRC Press, Boca Raton, London, New York (2011).
4. T. Vo-Dinh, Ed., *Biomedical Photonics Handbook*, 2nd ed., CRC Press, Boca Raton (2014).
5. V. V. Tuchin, *Tissue Optics: Light Scattering Methods and Instruments for Medical Diagnostics*, 3rd ed., Vol. **PM 254**, SPIE Press, Bellingham, Washington (2015).
6. V. V. Tuchin, "Light scattering study of tissues," *Physics-Uspekhi* **40**(5), 495–515 (1997).
7. V. Backman et al., "Polarized light scattering spectroscopy for quantitative measurement of epithelial cellular structures in situ," *IEEE J. Sel. Top. Quantum Electron.* **5**, 1019–1026 (1999).
8. S. L. Jacques, R. J. Roman, and K. Lee, "Imaging superficial tissues with polarized light," *Lasers Surg. Med.* **26**, 119–129 (2000).
9. L. V. Wang, G. L Coté, and S. L. Jacques, "Special section guest editorial: tissue polarimetry," *J. Biomed. Opt.* **7**, 278 (2002).
10. S. L. Jacques, J. C. Ramella-Roman, and K. Lee, "Imaging skin pathology with polarized light," *J. Biomed. Opt.* **7**(3), 329–340 (2002).
11. V. Shankaran, J. T. Walsh, Jr., and D. J. Maitland, "Comparative study of polarized light propagation in biological tissues," *J. Biomed. Opt.* **7**(3), 300–306 (2002).
12. I. M. Stockford et al., "Analysis of the spatial distribution of polarized light backscattering," *J. Biomed. Opt.* **7**(3), 313–320 (2002).
13. X. Wang and L. V. Wang, "Propagation of polarized light in birefringent turbid media: a Monte Carlo study," *J. Biomed. Opt.* **7**(3), 279–290 (2002).
14. K. C. Hadley and I. A. Vitkin, "Optical rotation and linear and circular depolarization rates in diffusively scattered light from chiral, racemic, and achiral turbid media," *J. Biomed. Opt.* **7**(3), 291–299 (2002).
15. V. V. Tuchin, L. Wang, and D. A. Zimnyakov, *Optical Polarization in Biomedical Applications*, Springer, New York (2006).
16. A. De Martino, Ed., "A polarization-based optical techniques applied to biology and medicine," in *Proc. European Workshop*, Ecole Polytechnique, Massy, France (2009).
17. G. L. Coté and B. D. Cameron, "A noninvasive glucose sensor based on polarimetric measurements through the aqueous humor of the eye," in *Handbook of Optical Sensing of Glucose in Biological Fluids and Tissues*, V. V. Tuchin, Ed., pp. 183–211, CRC Press, Taylor & Francis Group, London (2009).
18. N. Ghosh and I. A. Vitkin, "Tissue polarimetry: concepts, challenges, applications and outlook," *J. Biomed. Opt.* **16**, 110801 (2011).
19. S. L. Jacques, "Polarized light imaging of biological tissues" in *Handbook of Biomedical Optics*, D. Boas, C. Pitris, and N. Ramanujam, Eds., pp. 649–669, CRC Press, Boca Raton, London, New York (2011).
20. N. Ghosh, M. F. G. Wood, and I. A. Vitkin, "Polarized light assessment of complex turbid media such as biological tissues via Mueller matrix decomposition," in *Handbook of Photonics for Biomedical Science*, V. V. Tuchin, Ed., pp. 253–282, CRC Press, Taylor & Francis Group, London (2010).
21. D. Layden, N. Ghosh, and A. Vitkin, "Quantitative polarimetry for tissue characterization and diagnosis," in *Advanced Biophotonics: Tissue Optical Sectioning*, R. K. Wang and V. V. Tuchin, Eds., pp. 73–108, CRC Press, Taylor & Francis Group, Boca Raton, London, New York (2013).
22. A. Vitkin, N. Ghosh, and A. de Martino, "Tissue polarimetry" in *Photonics: Scientific Foundations, Technology and Applications*, D. L. Andrews, Ed., Vol. **IV**, pp. 239–321, John Wiley & Sons, Inc., Hoboken, New Jersey (2015).
23. S. G. Demos, H. B. Radousky, and R. R. Alfano, "Deep subsurface imaging in tissues using spectral and polarization filtering," *Opt. Express* **7**, 23–28 (2000).
24. R. S. Gurjar et al., "Imaging human epithelial properties with polarized light scattering spectroscopy," *Nature Med.* **7**, 1245–1248 (2001).
25. S. P. Morgan and I. M. Stockford, "Surface-reflection elimination in polarization imaging of superficial tissue," *Opt. Lett.* **28**, 114–116 (2003).
26. M. Hunter et al., "Tissue self-affinity and polarized light scattering in the Born approximation: a new model for precancer detection," *Phys. Rev. Lett.* **97**(13), 138102 (2006).
27. P. Shukla et al., "Influence of size parameter and refractive index of the scatterer on polarization-gated optical imaging through turbid media," *J. Opt. Soc. Am. A* **24**, 1704–1713 (2007).
28. V.M. Turzhitsky et al., "Measuring mucosal blood supply in vivo with a polarization-gating probe," *Appl. Opt.* **47**(32), 6046–6057 (2008).
29. S. M. Daly and M. J. Leahy, "'Go with the flow:' a review of methods and advancements in blood flow imaging," *J. Biophotonics* **6**(3), 217–255 (2013).
30. W. A. Shurkliff, *Polarized Light. Production and Use*, Harvard University Press, Cambridge, Massachussets (1962).
31. W. A. Shurkliff and S. S. Ballard, *Polarized Light*, Van Nostrand, Princeton (1964).
32. D. S. Kliger, J. W. Lewis, and E. C. Randall, *Polarized Light in Optics and Spectroscopy*, Academic Press, Boston (1990).
33. E. Collet, *Polarized Light. Fundamentals and Applications*, Dekker Inc., New York (1993).
34. R. M. A. Azzam and N. M. Bashara, *Ellipsometry and Polarized Light*, Elsevier Science, Amsterdam (1994).
35. C. Brosseau, *Fundamentals of Polarized Light: A Statistical Optics Approach*, Wiley, New York (1998).
36. D. H. Goldstein, *Polarized Light*, 3rd ed., CRC Press, Boca Raton (2010).
37. R. G. Johnston, S. B. Singham, and G. C. Salzman, "Polarized light scattering," *Comments Mol. Cell. Biophys.* **5**(3), 171–192 (1988).
38. G. C. Salzman et al., "Light scattering and cytometry," in *Flow Cytometry and Sorting*, 2nd ed., M. R. Melamed, T. Lindmo, and M. L. Mendelsohn, Eds., Wiley-Liss Inc., New York, pp. 81–107 (1990).
39. W. P. van de Merwe, D. R. Huffman, and B. V. Bronk, "Reproducibility and sensitivity of polarized light scattering for identifying bacterial suspension," *Appl. Opt.* **28**(23), 5052–5057 (1989).
40. B. V. Bronk et al., "Measuring diameters of rod-shaped bacteria in vivo with polarized light scattering," *Biophys. J.* **69**, 1170–1177 (1995).
41. W. P. Van de Merwe et al., "Polarized light scattering for rapid observation of bacterial size changes," *Biophys. J.* **73**, 500–506 (1997).
42. C. T. Gross et al., "Hemoglobin polymerization in sickle cells studied by circular polarized light scattering," *Biochim. Biophys. Acta* **1079**(2), 152–160 (1991).
43. R. W. Hart and R. A. Farrell, "Light scattering in the cornea," *J. Opt. Soc. Am.* **59**(6), 766–774 (1969).
44. R. L. McCally and R. A. Farrell, "Light scattering from cornea and corneal transparency," in *Noninvasive Diagnostic Techniques in Ophthalmology*, B. R. Master, Ed., pp. 189–210, Springer-Verlag, New York (1990).
45. I. L. Maksimova, V. V. Tuchin, and L. P. Shubochkin, "Polarization features of eye's cornea," *Opt. Spectrosc. (USSR)* **60**(4), 801–807 (1986).
46. D. S. Greenfield, R. W. Knighton, and X.-R. Huang, "Effect of corneal polarization axis on assessment of retinal nerve fiber layer thickness by scanning laser polarimetry," *Am. J. Ophthalmol.* **129**, 715–722 (2000).
47. I. L. Maksimova, V. V. Tuchin, and L. P. Shubochkin, "Light scattering matrix of crystalline lens," *Opt. Spectrosc. (USSR)* **65**(3), 615–619 (1988).

48. X.-R. Huang and R. W. Knighton, "Linear birefringence of the retinal nerve fiber layer measured in vitro with a multispectral imaging micropolarimeter," *J. Biomed. Opt.* **7**(2), 199–204 (2002).
49. A. W. Dreher, K. Reiter, and R. N. Weinreb, "Spatially resolved birefringence of the retinal never fiber layer assessed with a retinal laser ellipsometer," *Appl. Opt.* **31**, 3730–3735 (1992).
50. L. O. Svaasand and C. H. J. Gomer, "Optics of tissue," in *Dosimetry of Laser Radiation in Medicine and Biology*, Vol. **IS5**, pp. 114–132, SPIE Press, Bellingham, Washington (1989).
51. R. R. Anderson, "Polarized light examination and photography of the skin," *Arch. Dermatol.* **127**, 1000–1005 (1991).
52. J. M. Schmitt, A. H. Gandjbakhche, and R. F. Bonnar, "Use of polarized light to discriminate short-photons in a multiply scattering medium," *Appl. Opt.* **31**, 6535–6546 (1992).
53. P. Bruscaglioni, G. Zaccanti, and Q. Wei, "Transmission of a pulsed polarized light beam through thick turbid media: numerical results," *Appl. Opt.* **32**, 6142–6150 (1993).
54. D. Bicout et al., "Depolarization of multiply scattering waves by spherical diffusers: influence of the size parameter," *Phys. Rev. E* **49**, 1767–1770 (1994).
55. H. Horinaka et al., "Extraction of quasi-straightforward-propagating photons from diffused light transmitting through a scattering medium by polarization modulation," *Opt. Lett.* **20**, 1501–1503 (1995).
56. M. Dogariu and T. Asakura, "Photon pathlength distribution from polarized backscattering in random media," *Opt. Eng.* **35**, 2234–2239 (1996).
57. S. P. Morgan, M. P. Khong, and M. G. Somekh, "Effects of polarization state and scatterer concentration optical imaging through scattering media," *Appl. Opt.* **36**, 1560–1565 (1997).
58. A. H. Hielscher, J. R. Mourant, and I. J. Bigio, "Influence of particle size and concentration on the diffuse backscattering of polarized light from tissue phantoms and biological cell suspensions," *Appl. Opt.* **36**, 125–135 (1997).
59. A. Ambirajan and D. C. Look, "A backward Monte Carlo study of the multiple scattering of a polarized laser beam," *J. Quant. Spectrosc. Radiat. Transfer* **58**, 171–192 (1997).
60. N. Kollias, "Polarized light photography of human skin," in *Bioengineering of the Skin: Skin Surface Imaging and Analysis*, K.-P. Wilhelm et al., Eds., pp. 95–106, CRC Press, Boca Raton (1997).
61. G. Yao and L.-H. V. Wang, "Two-dimensional depth-resolved Mueller matrix characterization of biological tissue by optical coherence tomography," *Opt. Lett.* **24**, 537–539 (1999).
62. S. Jiao, G. Yao, and L.-H. V. Wang, "Depth-resolved two-dimensional Stokes vectors of backscattered light and Mueller matrices of biological tissue measured by optical coherence tomography," *Appl. Opt.* **39**, 6318–6324 (2000).
63. X. Wang and L. V. Wang, "Propagation of polarized light in birefringent turbid media: time-resolved simulations," *Opt. Express* **9**(5), 254–259 (2001).
64. D. A. Zimnyakov et al., "Residual polarization of non-coherently backscattered linearly polarized light: the influence of the anisotropy parameter of the scattering medium," *Waves Random Media* **11**, 395–412 (2001).
65. I. A. Vitkin and R. C. N. Studinski, "Polarization preservation in diffusive scattering from in vivo turbid biological media: effects of tissue optical absorption in the exact backscattering direction," *Opt. Commun.* **190**, 37–43 (2001).
66. C. K. Hitzenberger et al., "Measurement and imaging of birefringence and optic axis orientation by phase resolved polarization sensitive optical coherence tomography," *Opt. Express* **9**, 780–790 (2001).
67. J. F. de Boer and T. E. Milner, "Review of polarization sensitive optical coherence tomography and Stokes vector determination," *J. Biomed. Opt.* **7**(3), 359–371 (2002).
68. F. Jaillon and H. Saint-Jalmes, "Description and time reduction of a Monte Carlo code to simulate propagation of polarized light through scattering media," *Appl. Opt.* **42**(16), 3290–3296 (2003).
69. L. Dagdug, G. H. Weiss, and A. H. Gandjbakhche, "Effects of anisotropic optical properties on photon migration in structured tissues," *Phys. Med. Biol.* **48**, 1361–1370 (2003).
70. S. V. Gangnus, S. J. Matcher, and I. V. Meglinski, "Monte Carlo modeling of polarized light propagation in biological tissues," *Laser Phys.* **14**, 886–891 (2004).
71. A. P. Sviridov et al., "Enhancement of hidden structures of early skin fibrosis using polarization degree pattern and Pearson correlation analysis," *J. Biomed. Opt.* **10**(5), 051706 (2005).
72. F. Boulvert et al., "Analysis of the depolarizing of irradiated pig skin," *J. Opt. A: Pure Appl. Opt.* **7**, 21–28 (2005).
73. J. Ramella-Roman, S. Prahl, and S. Jacques, "Three Monte Carlo programs of polarized light transport into scattering media: part I," *Opt. Express* **13**(12), 4420–4438 (2005); Part II, Opt. Express 13(25), 10392–10405 (2005).
74. M. Xu and R. R. Alfano, "Circular polarization memory of light," *Phys. Rev.* **E 72**, 065601(R) (2005).
75. Y. L. Kim et al., "Circular polarization memory effect in low-coherence enhanced backscattering of light," *Opt. Lett.* **31**, 2744–2746 (2006).
76. P. J. Wu and J. T. Walsh Jr., "Stokes polarimetry imaging of rat tail tissue in a turbid medium: degree of linear polarization image maps using incident linearly polarized light," *J. Biomed. Opt.* **11**, 014031 (2006).
77. Y. U. P. Sinichkin et al., "Effect of optical anisotropy of scattering media on the state of polarization of the scattered light," *Opt. Spectrosc.* **101**(5), 802–810 (2006).
78. J. Ramachandran et al., "Light scattering and micro architectural differences between tumorigenic and non-tumorigenic cell models of tissue," *Opt. Express* **15**(7), 4039–4053 (2007).
79. J. Chung et al., "Use of polar decomposition for the diagnosis of oral precancer," *Appl. Opt.* **46**, 3038–3044 (2007).
80. M. Anastasiadou et al., "Polarimetric imaging for the diagnosis of cervical cancer," *Phys. Status Solidi* **5**, 1423–1426 (2008).
81. P. Shukla and A. Pradhan, "Mueller decomposition images for cervical tissue: potential for discriminating normal and dysplastic states," *Opt. Express* **17**, 1600–1609 (2009).
82. X. Li and G. Yao, "Mueller matrix decomposition of diffuse reflectance imaging in skeletal muscle," *Appl. Opt.* **48**, 2625–2631 (2009).
83. V. V. Tuchin, Ed., *Handbook of Optical Sensing of Glucose in Biological Fluids and Tissues*, CRC Press, Taylor & Francis Group, London (2009).
84. M. F. G. Wood et al., "Towards noninvasive glucose sensing using polarization analysis of multiply scattered light," in *Handbook of Optical Sensing of Glucose in Biological Fluids and Tissues*, V. V. Tuchin, Ed., pp. 527–562, CRC Press, Taylor & Francis Group, London (2009).
85. H. He et al., "Application of sphere-cylinder scattering model to skeletal muscle," *Opt. Express* **18**, 15104–15112 (2010).
86. Y. A. Ushenko, "Diagnostics of structure and physiological state of birefringent biological tissues: statistical, correlation and topological approaches," in *Coherent-Domain Optical Methods: Biomedical Diagnostics, Environmental Monitoring and Material Science*, 2nd ed., V. V. Tuchin, Ed., pp. 107–148, Springer Reference, Science + Business Media, New York (2013).
87. A. Pierangelo et al., "Ex vivo characterization of human colon cancer by Mueller polarimetric imaging," *Opt. Express* **19**, 1582–1593 (2011).
88. G. Purvinis, B. D. Cameron, and D. M. Altrogge, "Noninvasive polarimetric-based glucose monitoring: an in vivo study," *J. Diabetes Sci. Technol.* **5**(2), 380–387 (2011).
89. A. Doronin and I. Meglinski, "Online object oriented Monte Carlo computational tool for the needs of biomedical optics," *Biomed. Opt. Express* **2**(9), 2461–2469 (2011).
90. S. Alali et al., "Quantitative correlation between light depolarization and transport albedo of various porcine tissues," *J. Biomed. Opt.* **17**(4), 045004 (2012).
91. A. Pierangelo et al., "Multispectral Mueller polarimetric imaging detecting residual cancer and cancer regression after neoadjuvant treatment for colorectal carcinomas," *J. Biomed. Opt.* **18**(4), 046014 (2013).
92. E. Du et al., "Mueller matrix polarimetry for differentiating characteristic features of cancerous tissues," *J. Biomed. Opt.* **19**(7), 076013 (2014).
93. A. Doronin, C. Macdonald, and I. Meglinski, "Propagation of coherent polarized light in highly scattering turbid media," *J. Biomed. Opt.* **19**(2), 025005 (2014).
94. B. Kunnen et al., "Application of circularly polarized light for non-invasive diagnosis of cancerous tissues and turbid tissue-like scattering media," *J. Biophotonics* **8**(4), 317–323 (2015).

95. X. Feng, R. Patel, and A. N. Yaroslavsky, "Wavelength optimized cross-polarized wide-field imaging for noninvasive and rapid evaluation of dermal structures," *J. Biophotonics* **8**(4), 324–331 (2015).
96. C. F. Bohren and D. R. Huffman, *Absorption and Scattering of Light by Small Particles*, Wiley, New York (1983); Wiley-VCH Verlag GmbH & Co. KGaA, Weinheim (2004).
97. A. Z. Dolginov, Y. N. Gnedin, and N. A. Silant'ev, *Propagation and Polarization of Radiation in Cosmic Media*, Gordon and Breach, Basel (1995).
98. M. I. Mishchenko, J. W. Hovenier, and L. D. Travis, Eds., *Light Scattering by Nonspherical Particles*, Academic Press, San Diego (2000).
99. M. I. Mishchenko, L. D. Travis, and A. A. Lacis, *Scattering, Absorption, and Emission of Light by Small Particles*, Cambridge University Press, Cambridge (2002).
100. M. I. Mishchenko, L. D. Travis, and A. A. Lacis, *Multiple Scattering of Light by Particles: Radiative Transfer and Coherent Backscattering*, Cambridge University Press, New York (2006).
101. A. Kokhanovsky, *Polarization Optics of Random Media*, Springer-Verlag, Berlin, Heidelberg, New York (2003).
102. T. Khos-Ochir et al., "Polarimetric measurement of Jones matrix of a twisted nematic liquid crystal spatial light modulator," *J. Opt. Soc. Korea* **16**(4), 443–448 (2012).
103. S. Jiao and L. V. Wang, "Jones-matrix imaging of biological tissues with quadruple-channel optical coherence tomography," *J. Biomed. Opt.* **7**, 350–358 (2002).
104. I. L. Maksimova and L. P. Shubochkin, "Light-scattering matrices for a close-packed binary system of hard spheres," *Opt. Spectrosc.* **70**(6), 745–748 (1991).
105. M. K. Swami et al., "Size dependent patterns in depolarization maps from turbid medium and tissue," *Appl. Opt.* **53**(27), 6133–6139 (2014).
106. B. Deboo, J. Sasian, and R. A. Chipman, "Degree of polarization surfaces and maps for analysis of depolarization," *Opt. Express* **12**(20), 4941–4958 (2004).
107. H. C. van de Hulst, *Light Scattering by Small Particles*, Wiley, New York (1957); reprint, Dover, New York (1981); Multiple Light Scattering: Tables, Formulas and Applications, Academic Press, New York (1980).
108. A. H. Hielscher et al., "Diffuse backscattering Mueller matrices of highly scattering media," *Opt. Express* **1**(13), 441–453 (1997).
109. R. A. Chipman, "Polarimetry" in *Handbook of Optics: Vol. I—Geometrical and Physical Optics, Polarized Light, Components and Instruments*, M. Bass, Ed., pp. 22.1–22.37, McGraw-Hill Professional, New York (2010).
110. M. K. Swami, H. S. Patel, and P. K. Gupta, "Conversion of 3×3 Mueller matrix to 4×4 Mueller matrix for non-depolarizing samples," *Opt. Commun.* **286**(1), 18–22 (2013).
111. Y. Kamai and T. Ushiki, "The three-dimensional organization of collagen fibrils in the human cornea and sclera," *Invest. Ophthalmol. Vis. Sci.* **32**, 2244–2258 (1991).
112. R. A. Farrell, D. E. Freund, and R. L. McCally, "Research on corneal structure," *Johns Hopkins APL Tech. Dig.* **11**, 191–199 (1990).
113. R. A. Farrell and R. L. McCally, "Corneal transparency" in *Principles and Practice of Ophthalmology*, D. A. Albert and F. A. Jakobiec, Eds., pp. 629–643, W.B. Saunders, Philadelphia, Pennsylvania (2000).
114. V. V. Tuchin, "Optical polarization in biomedical applications, a polarization-based optical techniques applied to biology and medicine," in *Proc. European Workshop*, pp. 18–26, Ecole Polytechnique, Massy, France (2009).
115. Y. Huang and K. M. Meek, "Swelling studies on the cornea and sclera: the effect of pH and ionic strength," *Biophys. J.* **77**, 1655–1665 (1999).
116. I. Fine et al., "Optical properties of the sclera," *Phys. Med. Biol.* **30**, 565–571 (1985).
117. M. J. Costello, T. N. Oliver, and L. M. Cobo, "Cellular architecture in aged-related human nuclear cataracts," *Invest. Ophthal. Vis. Sci.* **33**(11), 3209–3227 (1992).
118. Y. Ozaki, "Medical application of Raman spectroscopy," *Appl. Spectrosc. Rev.* **24**(3), 259–312 (1988).
119. V. V. Tuchin, *Dictionary of Biomedical Optics and Biophotonics*, SPIE Press, Bellingham, Washington (2012).
120. P. M. Conn, Ed., *Neuroscience in Medicine*, Human Press, Totowa, New Jersey (2008).
121. H. A. Linares et al., "The histiotypic organization of the hypertrophic scar in humans," *J. Invest. Dermatol.* **59**(4), 323–331 (1972).
122. S. Nickell et al., "Anisotropy of light propagation in human skin," *Phys. Med. Biol.* **45**, 2873–2886 (2000).
123. G. B. Altshuler and V. N. Grisimov, "Effect of waveguide transport of light in human tooth," *USSR Acad. Sci. Reports* **310**(5), 1245–1248 (1990).
124. A. Kienle et al., "Light propagation in dentin: influence of microstructure on anisotropy," *Phys. Med. Biol.* **48**, N7–N14 (2003).
125. V. V. Tuchin and G. B. Altshuler, "Dental and oral tissue optics," in *Photonics in Dentistry. Series of Biomaterials and Bioengineering*, A. Kishen and A. Asundi, Eds., Imperial College Press, London, pp. 245–300 (2006).
126. C. Giannini et al., "Correlative light and scanning x-ray scattering microscopy of healthy and pathologic human bone sections," *Sci. Rep.* **2**, 435 (2012).
127. A. Beraudi et al., "Osteon classification in human fibular shaft by circularly polarized light," *Cells Tissues Organs* **191**(3), 260–268 (2010).
128. N. Ugryumova, S. J. Matcher, and D. P. Attenburrow, "Measurement of bone mineral density via light scattering," *Phys. Med. Biol.* **49**, 469–483 (2004).
129. D. P. Popescu et al., "Assessment of early demineralization in teeth using the signal attenuation in optical coherence tomography images," *J. Biomed. Opt.* **13**, 054053 (2008).
130. V. C. Mow, A. Ratcliffe, and A. R. Poole, "Cartilage and diarthrodial joints as paradigms for hierarchical materials and structures," *Biomaterials* **13**, 67–97 (1992).
131. J. A. Buckwalter and H. J. Mankin, "Articular cartilage. Part I: tissue design and chondrocyte-matrix interactions," *J. Bone Joint Surg. (Am.)* **79A**, 600–611 (1997).
132. S. J. Matcher, "A review of some recent developments in polarization-sensitive optical imaging techniques for the study of articular cartilage," *J. Appl. Phys.* **105**, 102041 (2009).
133. J. C. Mansfield et al., "Collagen fiber arrangement in normal and diseased cartilage studied by polarization sensitive nonlinear microscopy," *J. Biomed. Opt.* **13**(4), 044020 (2008).
134. T. A. Waigh, *Applied Biophysics: Molecular Approach for Physical Scientists*, John Wiley & Sons Ltd, Chichester (2007).
135. X. Wang et al., "Group refractive index measurement of dry and hydrated type I collagen films using optical low-coherence reflectometry," *J. Biomed. Opt.* **1**(2), 212–216 (1996).
136. R. P. Hemenger, "Refractive index changes in the ocular lens result from increased light scatter," *J. Biomed. Opt.* **1**, 268–272 (1996).
137. V. F. Izotova et al., "Investigation of Mueller matrices of anisotropic nonhomogeneous layers in application to optical model of cornea," *Appl. Opt.* **36**(1), 164–169 (1997).
138. R. Splinter and B. A. Hooper, *An Introduction to Biomedical Optics*, Taylor & Francis Publishers, New York, London (2007).
139. S. L. Jacques, "Optical properties of biological tissues: a review," *Phys. Med. Biol.* **58**, R37–R61 (2013).
140. K. Frank and M. Kessler, Eds., *Quantitative Spectroscopy in Tissue*, Pmi Verlag, Frankfurt am Main (1992).
141. I. L. Maksimova, "Scattering of radiation by regular and random systems comprised of parallel long cylindrical rods," *Opt. Spectrosc.* **93**(4), 610–619 (2002).
142. M. Born and E. Wolf, *Principles of Optics*, 7th ed., Cambridge University Press, Cambridge (1999).
143. J. M. Ziman, *Models of Disorder: The Theoretical Physics of Homogeneously Disordered Systems*, Cambridge University Press, London, New York, Melbourne (1979).
144. N. G. Khlebtsov et al., "Introduction to light scattering by biological objects," in *Handbook of Optical Biomedical Diagnostics*, 2nd ed., Vol. **PM 262**, pp. 1–155, V. V. Tuchin, Ed., SPIE Press, Bellingham, Washington (2016).
145. B. D. Cameron et al., "Measurement and calculation of the two-dimensional backscattering Mueller matrix of a turbid medium," *Opt. Lett.* **23**, 485–487 (1998); Errata: *Opt. Lett.* 23, 1630 (1998).
146. H. H. Tynes et al., "Monte Carlo and multicomponent approximation methods for vector radiative transfer by use of effective Mueller matrix calculations," *Appl. Opt.* **40**(3), 400–412 (2001).

147. I. L. Maksimova, S. V. Romanov, and V. F. Izotova, "The effect of multiple scattering in disperse media on polarization characteristics of scattered light," *Opt. Spectrosc.* **92**(6), 915–923 (2002).
148. M. J. Rakovic and G. W. Kattawar, "Theoretical analysis of polarization patterns from incoherent backscattering of light," *Appl. Opt.* **37**(15), 3333–3338 (1998).
149. M. J. Rakovic et al., "Light backscattering polarization patterns from turbid media: theory and experiment," *Appl. Opt.* **38**, 3399–3408 (1999).
150. S. Bartel and A. H. Hielscher, "Monte Carlo simulations of the diffuse backscattering Mueller matrix for highly scattering media," *Appl. Opt.* **39**, 1580–1588 (2000).
151. G. Bal and M. Moscoso, "Theoretical and numerical analysis of polarization for time-dependent radiative transfer equations," *J. Quant. Spectrosc. Radiat. Transf.* **70**, 75–98 (2001).
152. K. Y. Yong et al., "Characterization of layered scattering media using polarized light measurements and neural networks," *J. Biomed. Opt.* **8**(3), 504–511 (2003).
153. Y. Deng et al., "Characterization of backscattering Mueller matrix patterns of highly scattering media with triple scattering assumption," *Opt. Express* **15**(15), 9672–9680 (2007).
154. M. R. Antonelli et al., "Mueller matrix imaging of human colon tissue for cancer diagnostics: how Monte Carlo modeling can help in the interpretation of experimental data," *Opt. Express* **18**(10), 10200–10208 (2010).
155. M.-R. Antonelli et al., "Impact of model parameters on Monte Carlo simulations of backscattering Mueller matrix images of colon tissue," *Biomed. Opt. Express* **2**(7), 1836–1851 (2011).
156. N. Ghosh, M. F. G. Wood, and I. A. Vitkin, "Polarimetry in turbid, birefringent, optically active media: a Monte Carlo study of Mueller matrix decomposition in the backscattering geometry," *J. Appl. Phys.* **105**(10), 102023 (2009).
157. A. Doronin and I. Meglinski, "Peer-to-peer Monte Carlo simulation of photon migration in topical applications of biomedical optics," *J. Biomed. Opt.* **17**, 090504 (2012).
158. P. Ghassemi et al., "A new approach for optical assessment of directional anisotropy in turbid media," *J. Biophotonics* **9**(1–9), 100–108 (2015).
159. Y. Guo et al., "Study on retardance due to well-ordered birefringent cylinders in anisotropic scattering media," *J. Biomed. Opt.* **19**(6), 065001 (2014).
160. Y. Guo et al., "A study on forward scattering Mueller matrix decomposition in anisotropic medium," *Opt. Express* **21**(15), 18361–18370 (2013).
161. N. Riviere et al., "Hyperspectral polarized light scattering to study tumor cells in in-vitro samples," *Proc. SPIE* **8464**, 846410 (2012).
162. A. L. Oldenburg et al., "Motility-, autocorrelation-, and polarization-sensitive optical coherence tomography discriminates cells and gold nanorods within 3D tissue cultures," *Opt. Lett.* **38**(15), 2923–2926 (2013).
163. G. Wang et al., "A 3-D multicellular tumor spheroid on ultrathin matrix coated single cancer cells provides a tumor microenvironment model to study epithelial-to-mesenchymal transitions," *Polym. Chem.* **6**, 283–293 (2015).
164. I. L. Maksimova, S. N. Tatarintsev, and L. P. Shubochkin, "Multiple scattering effects in laser diagnostics of bioobjects," *Opt. Spectrosc.* **72**, 1171–1177 (1992).
165. V. V. Tuchin, "Tissue optics and photonics: biological tissue structures [review]," *J. Biomed. Photonics Eng.* **1**(1), 3–21 (2015).
166. V. V. Tuchin, "Tissue optics and photonics: light-tissue interaction [review]," *J. Biomed. Photonics Eng.* **1**(2), 98–134 (2015).
167. A. N. Yaroslavsky et al., "Influence of the scattering phase function approximation on the optical properties of blood determined from the integrating sphere measurements," *J. Biomed. Opt.* **4**(1), 47–53 (1999).
168. D. A. Zimnyakov, Y. P. Sinichkin, and V. V. Tuchin, "Polarization reflectance spectroscopy of biological tissues: diagnostic applications," *Izv. Vyash. Uchebn. Zaved. Radiofiz.* **47**, 957–975 (2005).
169. L. T. Perelman et al., "Observation of periodic fine structure in reflectance from biological tissue: a new technique for measuring nuclear size distribution," *Phys. Rev. Lett.* **80**, 627–630 (1998).
170. Y. P. Sinichkin et al., "Reflectance and fluorescence spectroscopy of human skin in vivo," in *Handbook of Optical Biomedical Diagnostics*, 2nd ed., V. V. Tuchin, Ed., pp. 95–185, SPIE Press, Bellingham, Washington (2016).
171. L. T. Perelman and V. Backman, "Light scattering spectroscopy of epithelial tissues: principles and applications," in *Handbook of Optical Biomedical Diagnostics*, 2nd ed., V. V. Tuchin, Ed., pp. 33–93, SPIE Press, Bellingham, Washington (2016).
172. K. Sokolov et al., "Reflectance spectroscopy with polarized light: is it sensitive to cellular and nuclear morphology?," *Opt. Express* **5**, 302–317 (1999).
173. J. R. Mourant et al., "Polarized angular dependent spectroscopy of epithelial cells and epithelial cell nuclei to determine the size scale of scattering structures," *J. Biomed. Opt.* **7**(3), 378–387 (2002).
174. L. Qiu et al., "Spectral imaging with scattered light: from early cancer detection to cell biology," *IEEE J. Sel. Top. Quantum Electron.* **18**(3), 1073–1083 (2012).
175. A. Myakov et al., "Fiber optic probe for polarized reflectance spectroscopy in vivo: design and performance," *J. Biomed. Opt.* **7**(3), 388–397 (2002).
176. J. R. Lakowicz, *Principles of Fluorescence Spectroscopy*, 2nd ed., Kluwer Academic/Plenum Publ., New York (1999); Third ed., Springer, New York (2006).
177. S. K. Mohanty et al., "Depolarization of autofluorescence from malignant and normal human breast tissues," *Appl. Opt.* **40**(7), 1147–1154 (2001).
178. N. Ghosh, S. K. Majumder, and P. K. Gupta, "Polarized fluorescence spectroscopy of human tissue," *Opt. Lett.* **27**, 2007–2009 (2002).
179. A. N. Yaroslavsky, V. Neel, and R. R. Anderson, "Demarcation of nonmelanoma skin cancer margins in thick excisions using multispectral polarized light imaging," *J. Invest. Dermatol.* **121**, 259–266 (2003).
180. A. N. Yaroslavsky, V. Neel, and R. R. Anderson, "Fluorescence polarization imaging for delineating nonmelanoma skin cancers," *Opt. Lett.* **29**, 2010–2012 (2004).
181. A. N. Yaroslavsky et al., "Combining multi-spectral polarized-light imaging and confocal microscopy for localization of nonmelanoma skin cancer," *J. Biomed. Opt.* **10**(1), 014011 (2005).
182. A. N. Yaroslavsky et al., "Fluorescence polarization of tetracycline derivatives as a technique for mapping nonmelanoma skin cancers," *J. Biomed. Opt.* **12**(1), 014005 (2007).
183. A. N. Yaroslavsky et al., "High-contrast mapping of basal cell carcinomas," *Opt. Lett.* **37**(4), 644–646 (2012).
184. V. F. Izotova, I. L. Maksimova, and S. V. Romanov, "Utilization of relation between elements of the Mueller matrices for estimating properties of objects and the reliability of experiments," *Opt. Spectrosc.* **80**(5), 753–759 (1996).
185. V. F. Izotova, I. L. Maksimova, and S. V. Romanov, "Analysis of errors of a laser polarization nephelometer," *Opt. Spectrosc.* **80**(6), 905–1001 (1996).
186. V. F. Izotova, I. L. Maksimova, and S. V. Romanov, "Simulation of polarization characteristics of the crystalline lens during protein aggregation with regard to multiple scattering," *Opt. Spectrosc.* **86**(6) 902–908 (1999).
187. A. J. Hunt and D. R. Huffman, "A new polarization-modulated light scattering instrument," *Rev. Sci. Instrum.* **44**(12), 1753–1762 (1973).
188. R. C. Thompson, J. R. Bottiger, and E. S. Fry, "Measurement of polarized light interactions via the Mueller matrix," *Appl. Opt.* **19**(8), 1323–1332 (1980).
189. Y. Tanaka et al., "Motion-artifact-robust, polarization-resolved second-harmonic-generation microscopy based on rapid polarization switching with electro-optic Pockells cell and its application to in vivo visualization of collagen fiber orientation in human facial skin," *Biomed. Opt. Express* **5**(4), 1099–1113 (2014).
190. E. L. DeWalt et al., "Polarization-modulated second harmonic generation ellipsometric microscopy at video rate," *Anal. Chem.* **86**, 8448–8456 (2014).
191. A. N. Korolevich, A. Y. Khairullina, and L. P. Shubochkin, "Effects of aggregation of large biological particles on the scattering matrix elements," *Opt. Spectrosc.* **77**(2), 278–282 (1994).
192. A. N. Korolevich, A. Y. Khairullina, and L. P. Shubochkin, "Scattering matrix for 'soft' particles," *Opt. Spectrosc.* **68**(2) 403–409 (1990).
193. A. G. Hoekstra and P. M. A. Sloot, "Biophysical and biomedical applications of nonspherical scattering," in *Light Scattering by Nonspherical Particles: Theory, Measurements, and Applications*, M.

I. Mishchenko, J. W. Hovenier, and L. D. Travis, Eds., pp. 585–602, Academic Press, San Diego (2000).

194. M. F. G. Wood et al., "Polarization birefringence measurements for characterizing the myocardium, including healthy, infracted, and stem cell regenerated tissues," *J. Biomed. Opt.* **15**(4), 047009 (2010).
195. S. Y. Lu and R. A. Chipman, "Interpretation of Mueller matrices based on polar decomposition," *J. Opt. Soc. Am. A* **13**(5), 1106–1113 (1996).
196. S. Manhas et al., "Mueller matrix approach for determination of optical rotation in chiral turbid media in backscattering geometry," *Opt. Express* **14**(1), 190–202 (2006).
197. M. K. Swami et al., "Polar decomposition of 3×3 Mueller matrix: a tool for quantitative tissue polarimetry," *Opt. Express* **14**(20), 9324–9337 (2006).
198. S. Manhas et al., "Polarized diffuse reflectance measurements on cancerous and noncancerous tissues," *J. Biophotonics* **2**(10), 581–587 (2009).
199. W. Wang et al., "Roles of linear and circular polarization properties and effect of wavelength choice on differentiation between ex vivo normal and cancerous gastric samples," *J. Biomed. Opt.* **19**(4), 046020 (2014).
200. J. Qi et al., "Narrow band 3×3 Mueller polarimetric endoscopy," *Biomed. Opt. Express* **4**, 2433–2449 (2013).
201. C. Macdonald and I. Meglinski, "Backscattering of circular polarized light from a disperse random medium influenced by optical clearing," *Laser Phys. Lett.* **8**(4), 324–328 (2011).
202. J. F. de Boer, "Polarization sensitive optical coherence tomography: phase sensitive interferometry for multi-functional imaging," in *Coherent-Domain Optical Methods: Biomedical Diagnostics, Environmental Monitoring and Material Science*, 2nd ed., V. V. Tuchin, Ed., pp. 857–888, Springer Reference, Science + Business Media, New York (2013).
203. L. F. Rojas-Ochoa et al., "Depolarization of backscattered linearly polarized light," *J. Opt. Soc. Am. A* **21**, 1799–1804 (2004).
204. P. Sun et al., "Mueller matrix decomposition for determination of optical rotation of glucose molecules in turbid media," *J. Biomed. Opt.* **19**(4), 046015 (2014).
205. E. E. Gorodnichev et al., "Transillumination of highly scattering media by polarized light," in *Light Scattering Reviews 8. Radiative Transfer and Light Scattering*, A. A. Kokhanovsky, Ed., pp. 317–361, Springer Praxis Books, Berlin, Heidelberg (2013).
206. E. E. Gorodnichev, A. I. Kuzovlev, and D. B. Rogozkin, "Impact of wave polarization on long-range intensity correlations in a disordered medium," *J. Opt. Soc. Am. A* **33**, 95–106 (2016).
207. J. A. Muccini et al., "Polarized light photography in the evaluation of photoaging," *J. Am. Acad. Dermatol.* **33**, 765–769 (1995).
208. R. Ortmann, "Use of polarized light for quantitative determination of the adjustment of the tangential fibres in articular cartilage," *Anat. Embryol.* **148**, 109–120 (1975).
209. D. P. Speer and L. Dahners, "The collagenous architecture of articular cartilage. Correlation of scanning electron microscopy and polarized light microscopy observations," *Clin. Orthopaed. Related Res.* **139**, 267–275 (1979).
210. J. P. Arokoski et al., "Decreased birefringence of the superficial zone collagen network in the canine knee (stifle) articular cartilage after long distance running training, detected by quantitative polarized light microscopy," *Ann. Rheum. Dis.* **55**, 253–264 (1996).
211. J. Rieppo et al., "Practical considerations in the use of polarized light microscopy in the analysis of the collagen network in articular cartilage," *Microsc. Res. Tech.* **71**, 279–287 (2008).
212. I. C. Buscemi and S. Guyot, "Near real-time polarimetric imaging system," *J. Biomed. Opt.* **18**(11), 116002 (2013).
213. N.-J. Jan et al., "Polarization microscopy for characterizing fiber orientation of ocular tissues," *Biomed. Opt. Express* **6**(12), 4705–4718 (2015).
214. B. Yang et al., "Polarized light spatial frequency domain imaging for non-destructive quantification of soft tissue fibrous structures," *Biomed. Opt. Express* **6**(4), 1520–1533 (2015).
215. N. T. Clancy et al., "Polarised stereo endoscope and narrowband detection for minimal access surgery," *Biomed. Opt. Express* **5**(12), 4108–4117 (2014).
216. S. Manhas et al., "Demonstration of full 4×4 Mueller polarimetry through an optical fiber for endoscopic applications," *Opt. Express* **23**(3), 3047–3054 (2015).
217. D. Chan et al., "In vivo spectroscopic ellipsometry measurements on human skin," *J. Biomed. Opt.* **12**, 014023 (2007).
218. X. Feng et al., "Polarization enhanced wide-field imaging for evaluating dermal changes caused by non-ablative fractional laser treatment," *Laser Surg. Med.* **48**(2), 150–156 (2016).
219. P. Banerjee et al., "Probing the fractal pattern and organization of Bacillus thuringiensis bacteria colonies growing under different conditions using quantitative spectral light scattering polarimetry," *J. Biomed. Opt.* **18**(3), 035003 (2013).
220. J. Soni et al., "Quantitative fluorescence and elastic scattering tissue polarimetry using an eigenvalue calibrated spectroscopic Mueller matrix system," *Opt. Express* **21**(13), 15475–15489 (2013).
221. J. Jagtap et al., "Quantitative Mueller matrix fluorescence spectroscopy for precancer detection," *Opt. Lett.* **39**(2), 243–246 (2014).
222. S. Satapathi, J. Soni, and N. Ghosh, "Fluorescent Mueller matrix analysis of a highly scattering turbid media," *Appl. Phys. Lett.* **104**, 131902 (2014).
223. N. S. J. Lim et al, "Early detection of biomolecular changes in disrupted porcine cartilage using polarized Raman spectroscopy," *J. Biomed. Opt.* **16**(1), 017003 (2011).
224. S. Ahlawat et al., "Polarized Raman spectroscopic investigations on hemoglobin ordering in red blood cells," *J. Biomed. Opt.* **19**(8), 087002 (2014).
225. J. M. Schmitt and S. H. Xiang, "Cross-polarized backscatter in optical coherence tomography of biological tissue," *Opt. Lett.* **23**(13), 1060–1062 (1998).
226. W. Drexler et al., "Correlation of collagen organization with polarization sensitive imaging of in vitro cartilage: implications for osteoarthritis," *J. Rheumatol.* **28**, 1311–1318 (2001).
227. R. V. Kuranov et al., "Complementary use of cross-polarization and standard OCT for differential diagnosis of pathological tissues," *Opt. Express* **10**, 707–713 (2002).
228. L. S. Dolin et al., "OCT fundamentals and clinical applications of endoscopic OCT" in *Coherent-Domain Optical Methods: Biomedical Diagnostics, Environmental Monitoring and Material Science*, 2nd ed., V. V. Tuchin, Ed., pp. 999–1064, Springer Reference, Science + Business Media, New York (2013).
229. S. J. Matcher, C. P. Winlove, and S. V. Gangnus, "Collagen structure of bovine intervertebral disc studied using polarization sensitive optical coherence tomography," *Phys. Med. Biol.* **49**, 1295–1306 (2004).
230. N. Ugrumova et al., "The collagen structure of equine articular cartilage, characterized using polarization-sensitive optical coherence tomography," *J. Phys. D: Appl. Phys.* **38**, 2612–2619 (2005).
231. T. Xie et al., "Use of polarization-sensitive optical coherence tomography to determine the directional polarization sensitivity of articular cartilage and meniscus," *J. Biomed. Opt.* **11**, 064001 (2006).
232. J. J. Shyu et al., "Polarization sensitive optical coherence tomography and the extracted optical properties," *Prog. Electromagn. Res.* **91**, 365–376 (2009).
233. D. K. Kasaragod et al., "Experimental validation of an extended Jones matrix calculus model to study the 3D structural orientation of the collagen fibers in articular cartilage using polarization-sensitive optical coherence tomography," *Biomed. Opt. Express* **3**(3), 378–387 (2012).
234. C. Fan and G. Yao, "Imaging myocardial fiber orientation using polarization sensitive optical coherence tomography," *Biomed. Opt. Express* **4**(3), 460–465 (2013).
235. Y. Wang and G. Yao, "Optical tractography of the mouse heart using polarization-sensitive optical coherence tomography," *Biomed. Opt. Express* **4**(11), 2540–2545 (2013).
236. M. Sugita et al., "Motion artifact and speckle noise reduction in polarization sensitive optical coherence tomography by retinal tracking," *Biomed. Opt. Express* **5**(1), 106–122 (2014).
237. M. Sugita et al. "Retinal nerve fiber bundle tracing and analysis in human eye by polarization sensitive OCT," *Biomed. Opt. Express* **6**(3), 1030–1054 (2015).
238. C. K. Hitzenberger and M. Pircher, "MUW approach of PS OCT," in *Optical Coherence Tomography: Technology and Applications*, 2nd ed., W. Drexler and J. G. Fujimoto, Eds., pp. 1103–1136, Springer Reference, Science + Business Media, New York (2015).
239. B. H. Park and J. F. de Boer, "Polarization sensitive optical coherence tomography," in *Optical Coherence Tomography: Technology and Applications*, 2nd ed., W. Drexler and J. G. Fujimoto, Eds.,

pp. 1055–1101, Springer Reference, Science + Business Media, New York (2015).
240. M. Yamanari et al., "Scleral birefringence as measured by polarization-sensitive optical coherence tomography and ocular biometric parameters of human eyes in vivo," *Biomed. Opt. Express* **5**(5), 1391–1402 (2014).
241. Y.-J. Hong et al., "Optically buffered Jones-matrix-based multifunctional optical coherence tomography with polarization mode dispersion correction," *Biomed. Opt. Express* **6**(1), 225–243 (2015).
242. Y. Yasuno et al., "Jones Matrix based polarization sensitive optical coherence tomography," in *Optical Coherence Tomography: Technology and Applications*, 2nd ed., W. Drexler and J. G. Fujimoto, Eds., pp. 1137–1162, Springer Reference, Science + Business Media, New York (2015).
243. P. H. Puhakka, "Estimation of articular cartilage properties using multivariate analysis of optical coherence tomography signal," *Osteoarthritis Cartilage* **23**(12), 2206–2213 (2015).
244. S. Wang and K. V. Larin, "Optical coherence elastography for tissue characterization: a review," *J. Biophotonics* **8**(4), 279–302 (2015).
245. A. Curatolo et al., "Ultrahigh-resolution optical coherence elastography," *Opt. Lett.* **41**(1), 21–24 (2016).
246. N. Gladkova et al., "Evaluation of oral mucosa collagen condition with cross-polarization optical coherence tomography," *J. Biophotonics* **6**(4), 321–329 (2013).
247. E. B. Kiseleva et al., "Differential diagnosis of human bladder mucosa pathologies in vivo with cross-polarization optical coherence tomography," *Biomed. Opt. Express* **6**(4), 1464–1476 (2015).
248. E. V. Gubarkova et al., "Multi-modal optical imaging characterization of atherosclerotic plaques," *J. Biophotonics* (2015).
249. R. C. Lee et al., "Automated assessment of the remineralization of artificial enamel lesions with polarization-sensitive optical coherence tomography," *Biomed. Opt. Express* **5**(9), 2950–2962 (2014).
250. K. H. Chan et al., "Use of 2D images of depth and integrated reflectivity to represent the severity of demineralization in cross-polarization optical coherence tomography," *J. Biophotonics* **8**(1–2), 36–45 (2015).
251. F. S. Pavone and P. J. Campagnola, Eds., *Second Harmonic Generation Imaging*, CRC Press, Boca Raton, Florida (2013).
252. S. Brasselet, "Polarization-resolved nonlinear microscopy: application to structural molecular and biological imaging," *Adv. Opt. Photonics* **3**, 205–271 (2011).
253. H. B. de Aguiar, P. Gasecka, and S. Brasselet, "Quantitative analysis of light scattering in polarization-resolved nonlinear microscopy," *Opt. Express* **23**(7), 8960–8973 (2015).
254. G. Milione et al., "Measuring the self-healing of the spatially inhomogeneous states of polarization of vector Bessel beams," *J. Opt.* **17**, 035617 (2015).
255. J. Park et al., "Focusing through turbid media by polarization modulation," *Opt. Lett.* **40**(8), 1667–1670 (2015).
256. Z. Ding, C.-P. Liang, and Y. Chen, "Technology developments and biomedical applications of polarization-sensitive optical coherence tomography," *Front. Optoelectron.* **8**(2), 128–140 (2015).
257. K. H. Kim et al., "In vivo imaging of human burn injuries with polarization-sensitive optical coherence tomography," *J. Biomed. Opt.* **17**(6), 066012 (2012).
258. K. Sahu et al., "Noninvasive assessment of healing of bacteria infected and uninfected wounds using optical coherence tomography," *Skin Res. Tech.* **16**, 428–437 (2010).
259. K. Sahu et al., "Effect of poly-L-lysine-chlorin P6-mediated antimicrobial photodynamic treatment on collagen restoration in bacteria-infected wounds," *Photomed. Laser Surg.* **32**(1), 23–29 (2014) [Epub ahead of print].
260. K. H. Chan et al., "Clinical monitoring of smooth surface enamel lesions using CP-OCT during nonsurgical intervention," *Laser Surg. Med.* (2016).
261. T. C. Wood and D. S. Elson, "Polarization response measurement and simulation of rigid endoscopes," *Biomed. Opt. Express* **1**(2), 463–470 (2010).
262. D. Kapsokalyvas et al., "In-vivo imaging of psoriatic lesions with polarization multispectral dermoscope and multiphoton microscopy," *Biomed. Opt. Express* **5**(7), 2405–2419 (2014).
263. A. K. Dharmadhikari et al., "On the birefringence of healthy and malaria-infected red blood cells," *J. Biomed. Opt.* **18**(12), 125001 (2013).
264. M. Kinnunen et al., "Optical clearing at cellular level," *J. Biomed. Opt.* **19**(7), 071409 (2014).
265. J. Aaron et al., "Polarization microscopy with stellated gold nanoparticles for robust, in-situ monitoring of biomolecules," *Opt. Express* **16**(3), 2153–2167 (2008).
266. M. K. Swami et al., "Spectral Mueller matrix measurements for characterization of depolarization from non-spherical gold nanoparticles," *Opt. Commun.* **308**, 136–141 (2013).
267. M. K. Swami et al., "Effect of gold nanoparticles on depolarization characteristics of Intralipid tissue phantom," *Opt. Lett.* **38**(15), 2855–2657 (2013).
268. P. Zhang et al., "Imaging single chiral nanoparticles in turbid media using circular-polarization optical coherence microscopy," *Sci. Rep.* **4**, 4979 (2014).
269. M. Ney and I. Abdulhalim, "Ultrahigh polarimetric image contrast enhancement for skin cancer diagnosis using InN plasmonic nanoparticles in the terahertz range," *J. Biomed. Opt.* **20**(12), 125007 (2015).
270. Y. Cui et al., "Optical clearing delivers ultrasensitive hyperspectral dark-field imaging for single-cell evaluation," *ACS Nano* **10**(3), 3132–3143 (2016).
271. O. V. Angelsky, A. G. Ushenko, and Y. G. Ushenko, "Investigation of the correlation structure of biological tissue polarization images during the diagnostics of their oncological changes," *Phys. Med. Biol.* **50**(20), 4811–4822 (2005).
272. Y. A. Ushenko et al., "New parameter for describing and analyzing the optical-anisotropic properties of biological tissues," *J. Innov. Opt. Health Sci.* **4**(4), 463–475 (2011).
273. P. R. Bargo and N. Kollias, "Measurement of skin texture through polarization imaging," *Br. J. Dermatol.* **162**, 724–731 (2010).
274. D. Huang et al., "Optical coherence tomography," *Science* **254**, 1178–1181 (1991).
275. V. V. Bakutkin et al., "Diffusion of light by the human sclera," *J. Appl. Spectrosc.* **46**(1), 86–89 (1987).
276. V. V. Tuchin, "Laser light scattering in biomedical diagnostics and therapy," *J. Laser Appl.* **5**(2), 43–60 (1993).
277. V. V. Tuchin et al., "Light propagation in tissues with controlled optical properties," *J. Biomed. Opt.* **2**(4), 401–417 (1997).
278. G. Vargas et al., "Use of an agent to reduce scattering in skin," *Laser Surg. Med.* **24**(2), 133–141 (1999).
279. V. V. Tuchin, "Coherent optical techniques for the analysis of tissue structure and dynamics," *J. Biomed. Opt.* **4**(1), 106–124 (1999).
280. V. V. Tuchin, "Optical immersion as a new tool to control optical properties of tissues and blood," *Laser Phys.* **15**(8), 1109–1136 (2005).
281. V. V. Tuchin, "Optical clearing of tissue and blood using immersion method," *J. Phys. D: Appl. Phys.* **38**, 2497–2518 (2005).
282. V. V. Tuchin, *Optical Clearing of Tissues and Blood*, SPIE Press, Bellingham, Washington (2006).
283. A. P. Ivanov, S. A. Makarevich, and A. Y. Khairulina, "Propagation of radiation in tissues and liquids with densely packed scatterers," *J. Appl. Spectrosc.* **47**(4), 662–668 (1988).
284. C. G. Rylander et al., "Dehydration mechanism of optical clearing in tissue," *J. Biomed. Opt.* **11**(4), 041117 (2006).
285. A. T. Yeh et al., "Reversible dissociation of collagen in tissues," *J. Invest. Dermatol.* **121**, 1332–1335 (2003).
286. A. T. Yeh and J. Hirshburg, "Molecular interactions of exogenous chemical agents with collagen implications for tissue optical clearing," *J. Biomed. Opt.* **11**(1), 014003 (2006).
287. J. Hirshburg et al., "Correlation between collagen solubility and skin optical clearing using sugars," *Laser Surg. Med.* **39**(2), 140–144 (2007).
288. J. Hirshburg et al., "Molecular basis for optical clearing of collagenous tissues," *J. Biomed. Opt.* **15**(5), 055002 (2010).
289. V. V. Tuchin, "A clear vision for laser diagnostics," *IEEE J. Sel. Top. Quantum Electron.* **13**(6), 1621–1628 (2007).
290. E. A. Genina, A. N. Bashkatov, and V. V. Tuchin, "Tissue optical immersion clearing," *Expert Rev. Med. Devices* **7**(6), 825–842 (2010).

291. K. V. Larin et al., "Optical clearing for OCT image enhancement and in-depth monitoring of molecular diffusion," *IEEE J. Sel. Top. Quantum Electron.* **18**(3), 1244–1259 (2012).
292. D. Zhu et al., "Recent progress in tissue optical clearing," *Laser Photon. Rev.* **7**(5), 732–757 (2013).
293. O. Nadiarnykh and P. J. Campagnola, "SHG and optical clearing," in *Second Harmonic Generation Imaging*, F. S. Pavone and P. J. Campagnola, Eds., pp. 169–189, CRC Press, Taylor & Francis Group, Boca Raton, London, New York (2014).
294. E. A. Genina et al., "Optical clearing of biological tissues: prospects of application in medical diagnostics and phototherapy [review]," *J. Biomed. Photonics Eng.* **1**(1), 22–58 (2015).
295. R. K. Wang and V. V. Tuchin, "Optical tissue clearing to enhance imaging performance for OCT," in *Optical Coherence Tomography: Technology and Applications*, 2nd ed., W. Drexler and J. G. Fujimoto, Eds., pp. 1455–1488, Springer Reference, Science + Business Media, New York (2015).
296. D. A. Zimnyakov, G. V. Simonenko, and V. V. Tuchin, "Dispersion dependence of the optical anisotropy and the degree of depolarization of fibrous tissue," *J. Opt. Technol.* **77**(9), 577–581 (2010).
297. G. V. Simonenko et al., "Measurement of an optical anisotropy of biotissues," *Proc. SPIE* **3915**, 152–157 (2000).
298. G. V. Simonenko, V. V. Tuchin, and N. A. Lakodina, "Measurement of the optical anisotropy of biological tissues with the use of a nematic liquid crystal cell," *J. Opt. Technol.* **67**, 559–563 (2000).
299. H. G. Akarçay et al., "Monte Carlo modeling of polarized light propagation. Part I. Stokes versus Jones," *Appl. Opt.* **53**, 7576–7585 (2014).
300. H. G. Akarçay et al., "Monte Carlo modeling of polarized light propagation. Part II. Stokes versus Jones," *Appl. Opt.* **53**, 7586–7602 (2014).

Valery V. Tuchin is a professor and head of optics and biophotonics at Saratov National Research State University and a few other universities and institutions. His research interests include tissue optics, laser medicine, tissue optical clearing, and nanobiophotonics. He is a fellow of SPIE and OSA, has been awarded Honored Science Worker of the Russia, SPIE Educator Award, FiDiPro (Finland), Chime Bell Prize of Hubei Province (China), and Joseph W. Goodman Book Writing Award (OSA/SPIE).